NORTHWESTERN UNIVERSITY

Chromatin Scaling and the Regulation of Cellular Function

A DISSERTATION

SUBMITTED TO THE GRADUATE SCHOOL
IN PARTIAL FULFILLMENT OF THE REQUIREMENTS

for the degree

DOCTOR OF PHILOSOPHY

Field of Biological Sciences

By

Greta Mary Wodarcyk (Bauer)

EVANSTON, ILLINOIS

September 2018

Abstract

Chromatin Scaling and the Regulation of Cellular Function

Greta Mary Wodarcyk (Bauer)

Chromatin organization involves a hierarchy of length scales ranging from a few tens of nanometers in nucleosomes to hundreds of nanometers for chromosomal territories. This physical nanostructure is regulated by the genetic code, differential methylation and histone modifications that comprise the histone code, as well as non-molecular factors, such as crowding, ionic conditions, and pH. We have developed a novel optical spectroscopic microscopy technique, live cell Partial Wave Spectroscopic (PWS) microscopy, which allows us to interrogate the structure-function relationship of chromatin between 20 and 350 nm in critical processes including DNA repair, replication, transcription, cell cycle, and proliferation. We have demonstrated, both computationally and experimentally, that the physico-chemical regulation of chromatin packing scaling, as measured by PWS, can be used to manipulate transcriptional diversity, intercellular heterogeneity, and gene network heterogeneity. Here we use PWS microscopy and complementary biological assays to show the driving force of chromatin scaling and its regulation in the context of several biological applications including cardiovascular inflammation, stem cell plasticity, and carcinogenesis and chemoevasion. We show that controlling the physicochemical environment within the cell's nucleus to alter chromatin scaling can predictably modulate global patterns in gene expression. This whole-transcriptome manipulation based on the control of the physiochemical nanoenvironment of chromatin has implications in these as well as essentially any disease state and may allow for the ability to control the overall behavior of biological systems.

Thesis Advisor: Dr. Vadim Backman

Acknowledgements

It is difficult to believe that my time in graduate school at Northwestern has come to a close. The academic and personal support I have received over the past five years has been overwhelming, and I would like to thank some of the most important people without whose support this thesis would not have been possible.

First and foremost, I would like to thank my thesis advisor, Dr. Vadim Backman. Vadim has been inspirational in his enthusiasm for the lab's research projects and has always made himself available to discuss results and direction of projects. He is also incredibly supportive of all of his students, both in their scientific as well as their personal endeavors. I would also like to thank many members, both past and present, of the Backman Lab. Dr. Yolanda Stypula and Dr. Luay Almassalha were my first mentors in lab and thoroughly trained me both on all the techniques used in lab and also in how to think critically about interdisciplinary research projects. In particular, Dr. Luay Almassalha has been the best senior mentor I could have asked for throughout the entire time I have been in the lab. Not only has he continued to provide scientific guidance over the years, but he has also taught me the best qualities of leadership as I now begin to mentor the next generation of students in lab.

Additionally, I would like to thank Scott Gladstein and Dr. John Chandler, with whom I worked on many interdisciplinary projects and publications. They patiently explained the theory and instrumentation behind the microscopy techniques employed in our research and reminded me to think about project design and conclusions from more than just the biological mindset. A huge thank you goes to David VanDerway, the best lab tech anyone could ever ask for. He took on 25+ lines worth of cell culture and sample prep and also contributed essential experiments, including many long overnight sessions of data collection. I would also like to thank Andrew Stawarz for his work on projects as well as Jane Frederick, Ranya Virk, and Vasundhara Agrawal, an excellent group of first years who are taking over the macrogenomic engineering project. Other thanks go to Adam Eschein and Yue Li, for their collaborations on STORM and ChromEMT and to Wenli Wu for her collaboration on modeling aspects of the macrogenomic engineering project. I would also like to thank Dr. Michele Jen, Dr. Bin Jiang, and Dr. Xinlong Wang from Dr. Guillermo Ameer's lab for their work and collaboration on some of the sections of this thesis work. Finally, I would like to thank Ben Keane for keeping all of our meetings scheduled and

on track and for answering daily questions about logistics and meetings as well as Maria Proenca for her office companionship but also for her wonderful lab management and for putting up with nonstop questions regarding finances, reagent ordering, equipment malfunctions, and general lab complaints.

Thank you to my committee members Dr. Jason Brickner, Dr. Guillermo Ameer, and Dr. Evan Scott for their critical questions and guidance at our meetings over the past five years. It has been very helpful to have such a scientifically diverse committee. Thank you also to the collaborators with whom I have worked these past five years: Dr. Guillermo Ameer on my rotation projects and now more recently on stem cell applications of the macrogenomic engineering project, Dr. Igal Szleifer on the modeling aspects of the macrogenomic engineering project, Dr. Hemant Roy on the macrogenomic engineering project, and Dr. Shahabi on the macrogenomic engineering project and its translation into the clinical setting.

While much of my thesis work was done on instrumentation that was designed in-lab, I also utilized several of NU's core facilities. I would like to thank the High Throughput Analysis Lab, the Northwestern Sequencing Core, and the Keck Biophysical Facility for their help in data acquisition. Additionally, I would like to thank the training programs in which I have participated. The Biotechnology Training Program and the Robert H. Lurie Translational Bridge Program have increased my exposure to the scientific community and encouraged me to present my research to a group of scientists and clinicians with diverse backgrounds.

Finally, I would like to thank my family members for their support in my pursuit of a PhD. A special thank you goes also to my first Evanston "family," my roommate for the first three years of grad school, Dr. Stacey Barnaby. She guided me through the intricacies of grad school life and provided an excellent example of hard work and dedication to graduate studies. Without our nightly conversations and exchange of lab stories, the early years of grad school would have been a lot lonelier.

Last, but certainly not least, I owe a tremendous thank you to my husband, Michael Wodarcyk, for his encouragement and support over the past five years. From the initial days of dating as I prepared for my qualifying exams to planning a wedding with me during grant season to encouraging me through the final stretch of committee meetings, thesis writing, and thesis defense two weeks before the due date of our first child, he has never been anything but supportive and understanding of me and my work.

Table of Contents

List of Figures

List of Tables

Chapter 1: Introduction

1.1. BACKGROUND AND SIGNIFICANCE

Every cellular and extracellular structure has a complex nanoscale organization ranging from individual macromolecules that are a few nanometers in size (e.g. protein, DNA) to macromolecular assemblies that are tens to hundreds of nanometers in size (e.g. cell membranes, higher-order chromatin structure, cytoskeleton, and extracellular matrix fibers). A major scientific challenge is to understand these macromolecular structures, specifically their function and interactions in structurally and dynamically complex living cellular systems. In particular, one prominent area of biological research is the understanding of the structure-function relationship of chromatin. Chromatin organization (which is comprised of DNA, histones, and hundreds of other conjugated proteins and small molecules such as RNA) involves a hierarchy of length scales ranging from a few tens of nanometers in nucleosomes to hundreds of nanometers for chromosomal territories (1, 2). The physical nanostructure of chromatin is regulated by numerous molecular factors, including the primary DNA sequence composition, differential methylation patterns, histone modifications, polycomb and cohesin protein complexes, RNA and DNA polymerases, long noncoding RNA, etc., and non-molecular factors, such as crowding, ionic conditions, and pH. Due to this complexity and the lack of existing optical techniques that can rapidly sample information below 200 nm, little is known about the higher-order chromatin structure at length scales between 20 and 350 nm or their dynamics in live cells (e.g., the folding structure of chromatin above that of mononucleosomes).

At length scales between 100 and 200 nm, recent work using super resolution microscopy has shown a power-law (fractal) relation in the organization of chromatin, with domains of highly dense, inactive chromatin localizing within a few hundred nanometers of transcriptionally active sites (3). Furthermore, *in vitro* studies using texture analysis of microscopy images have shown that the topology of chromatin is well represented as a fractal media (4). Likewise, *ex vivo* analysis of somatic copy number alterations and neutron scattering measurements of isolated nuclei have shown that, across these length scales, chromatin is well described as a fractal media (5-7). In conjunction, molecular techniques such as chromosomal capture methods [chromosome conformation capture (3C) and high-throughput 3C (Hi-C)]

have shown that the higher-order organization of chromatin above single nucleosomes and below the structure of chromosomal territories follows this same power-law fractal organization. These methods have shown that topology of this higher-order organization is correlated with the regulation of gene transcription (8-10) and capable of evolving rapidly under stress conditions to globally regulate the expression of genes (11). Critically, these observed changes in chromatin structure have recently been linked to the regulation of genes often implicated in oncogenesis (12).

Additionally, ChromEMT, a new electron microscopy technique with unprecedented resolution (3 nm), revealed that above the level of the nucleosome, chromatin is simply a disordered polymer, a heterogeneously packed 2-20nm basic chain of DNA strands and nucleosomes (13). This basic chain is consistent across the genome and has no "ordered" organization, such as the 30nm fiber that has been debated for the past several years. While techniques like Hi-C and superresolution microscopy have given us new insights into just how this disordered chain is organized within the nucleus through TADs, A/B compartments, and other features of genome organization, there is still much to be learned about chromatin dynamics in live cells at the kbp-Mbp range or from about 20-350 nm, where packing of this 2-20nM chain of DNA strands and nucleosomes is driven by loop formation and the laws of polymer physics.

However, in order to study the packing of this chromatin polymer, there is a need for a new technique, namely a live cell imaging technology platform with nanoscale sensitivity (<200nm) and the ability to provide label-free, quantitative, molecularly informative, and non-perturbing, and information on the chromatin scaling at these length scales (20-350 nm, or the kilo base pair – mega base pair range). In the following work, we will present such a technique, live cell Partial Wave Spectroscopic (PWS) microscopy that allows for such a capacity.

In addition to a better understanding of how chromatin is packaged within the nucleus and how that packaging is influenced by the nuclear nanoenvironment, there is a need to better understand exactly how the physical scaling of chromatin influences critical cellular process such as transcription. Gene expression is influenced by both molecular and physico-chemical factors, and regulation of gene expression occurs across a hierarchy of length scales: at the genetic level through the role of transcription factors; at the nucleosomal level through alterations in local DNA accessibility (~10nm); and through

genome compartmentalization conferred by organization of DNA into a range of domains (~100nm, ~100kbp-Mbp) (14). Emerging evidence indicates the existence of yet another level of transcriptional regulation, potentiated by chromatin packing, which works across these length scales (~20-350nm length scales; ~kbp – Mbp) and affects *global patterns* of gene expression (13, 15-17). Gene expression is a series of interrelated chemical reactions that depend on the complex chromatin nanoenvironment (e.g. nanoscale-local ionic environment, pH, molecular crowding). In turn, the nanoenvironment both can be expected to affect and be affected by chromatin packing. Chromatin packing shapes the genomic information space by altering chromatin conformation while governing local chemical reaction rates. As a result, more realistic models and experimental validation of chromatin not as an isolated chain of DNA but as a dynamic player in a dense and highly interconnected nanoenvironment are necessary in order to understand the structure-function relationship between chromatin and transcription, or the direct and global effects of chromatin packing on the regulation of global gene expression and thus fundamental cellular processes.

The ability to target chromatin scaling as a means of controlling cell function could have tremendous power in the ability to regulate disease states, Classically, epigenetics has been studied through analysis of localized histone or DNA chemical modifications. While the role of these molecular transformations is indisputable, the overall folding of the genome likely depends on the confluence of numerous regulators. For example, deacetylation of histones creates a positive charge on the histones, increasing affinity for the negatively charged DNA. However, this modification in affinity can potentially be achieved by altering the counter-ion concentrations surrounding chromatin (K^+ or Ca^{2+}) (18). As a result, there is a need for a more systematic study of how to regulate the scaling of chromatin. Such approaches can be found in adapting the model of chromatin as a polymer and targeting its packing properties through two different methods: 1) Processes that use ATP and molecular motors to create chromatin loops such as through the regulation of CTCF or cohesins, and 2) By targeting the natural conformation assumed by chromatin as dependent on strength of chromatin self-interactions and chromatin-solute interactions, either through molecular specific regulation or through physical regulation of the nanoenvironment. If such methods can be developed, they would pave the way for the study and

treatment of diseases — such as Parkinson's disease, atherosclerosis, and autoimmune disorders — that are governed by the complex interplay of dozens of genes.

One context where chromatin scaling can be expected to play a critical role in disease progression and where its targeting may have profound functional consequences is that of cardiovascular inflammation. A significant long-term challenge to vascular intervention procedures, such as stenting and bypass surgery using vascular grafts, is restenosis due to neointimal hyperplasia (19). The cause of this neointimal hyperplasia is the induction of an inflammatory and oxidative stress milieu due to vascular damage that triggers proliferation and migration of vascular cells throughout the vessel lumen. Although the mechanisms that lead to neointimal hyperplasia are complex, it is now recognized that the adventitia plays a major role in neointima formation (20-22). In particular, adventitial fibroblasts (AFs) can secrete proinflammatory cytokines, growth factors, and reactive oxygen species that affect vascular remodeling (23, 24). Therefore, strategies that aim to reduce the pro-inflammatory and pro-oxidative responses of adventitial fibroblasts during injury or disease in the vascular wall may be novel approaches to reduce neointimal hyperplasia (25-29).

Sirt1, an NAD+-dependent lysine deacetylase, has been shown to be protective against oxidative stress and its inhibition has been shown to reduce DNA repair in vascular smooth muscle cells. As a result, we can potentially explore Sirt1 overexpression as a means to elicit vasculoprotective cellular responses in adventitial fibroblasts that are mediated in part by modulation of chromatin scaling, due to its function as a lysine deacetylase, prevent restenosis due to neointimal hyperplasia following vascular injury.

Another context where chromatin scaling can be expected to play a critical role is in the case of stem cell technology and regenerative medicine. Here, there are a several potential ways we might hope to improve cell fate outcome: some stem cells, like iPSCs spontaneously differentiate, so methods to maintain culture purity are necessary. Alternately, some types of stem cells take several days to differentiate and if the end goal is stem cell differentiation, methods to increase their differentiation capacity would prove beneficial. A third goal would be to increase re-programming capabilities of differentiated cells, if the end goal is tissue regeneration or some other application in which a more

pluripotent state is desirable. In short, targeting chromatin scaling in stem cells has the potential to enhance cellular plasticity and modulate cells in either direction along the stem continuum.

Finally, the role of nuclear morphology and chromatin alterations in disease has perhaps historically been most studied in carcinogenesis. Abnormalities in nuclear organization are one of the most definitive markers of dysplasia and malignancy and have been universally used by pathologists for decades. Of note, microscopic nuclear alterations such as nuclear atypia and abnormal nuclear texture (microscale chromatin heterogeneity) are consistently observed by pathologists in the absolute majority of solid tumors and are convergent physical phenomena in multiple molecular carcinogenesis pathways. These alterations can have profound effects on many critical cellular functions, such as gene expression and DNA replication, but the role of chromatin structure on these processes in the earliest stages of cancer development is still not well understood.

Electron microscopy has long been the gold standard for detecting nanoscale changes in cellular structure. While these ultrastructures can be identified by TEM, there are significant downsides to using electron microscopy as a diagnostic or pre-diagnostic screening tool in the clinical setting. Primarily, TEM imaging has high costs per sample and has significant restrictions in availability due to the difficult and lengthy sample preparation required. Furthermore, the inherent complexity of TEM preparation necessitates expert use and analysis, which consequently prevents the technique from being used as a high-throughput diagnostic tool. Optical microscopy techniques are a much more practical choice for clinical diagnostics due to their relatively low cost, high throughput, and ease of use. Historically, we have used novel optical microscopy tools to study the convergence of the physical structure of chromatin with the molecular transformations frequently observed in carcinogenesis (e.g. aberrant transcriptional alterations, epigenetic changes in histones, etc) and suggest that the topology of chromatin may be more than a marker of the molecular transformation of cells during malignancy. Indeed, this evidence suggests that deformation of chromatin folding could play a role in driving the observed molecular transformations.

In this context, it may be important to consider the physical folding of chromatin in and of itself as a regulator of gene expression and a potential contributor to oncogenesis (17). This may allow us to better understand the overall integration between the heterogeneous epigenetic transformations that occur during oncogenesis. In this view, changes in DNA methylation (CpG Islands), histone modifications,

and mutations in both higher-order chromatin modulators (cohesins, condensins) and histone modifying enzymes (HDACs, SWItch/Sucrose Non-Fermentable enzymes) could be convergent on global changes that act at the level of a genomic 'folding code' (30-33).

Furthermore, the modulation of this higher order folding code can be viewed in the context of increasing interest in targeting epigenetic mechanisms for cancer therapeutics. Unlike genetic modifications that largely cannot be reversed, epigenetic therapies present the opportunity for reversible regulation of gene expression by altering the epigenetic state of cells. To date, clinical trials have found some success at this epigenetic level through the use of DNA demethylating agents, HDAC inhibitors, and the histone methyltranserase EZH2 (34, 35) (36, 37). Indeed, the success of these interventions is due to the role that epigenetic mutations and modifications have in conferring resistance to traditional chemotherapeutics. At a broader level, this epigenetically driven resistance may be in part due to global alterations in chromatin topology producing increased access to the genomic information space. Thus, epigenetic therapies that regulate both local modifications to critical genes and the overall folding of the genome could have a considerable effect on delaying the emergence of chemoresistance.

In the future, pairing gene editing and macrogenomic engineering may allow for the hitherto unachieved capacity to control the overall behavior of biological systems. The joint application of genomic editing and macrogenomic engineering could significantly enhance existing capabilities to regulate biological behavior in complex systems where global transcriptional reprogramming takes place, including pathologies related to atherosclerosis, neurodegeneration, wound-repair, oncology, and inflammation. Whereas genome-editing tools would supply the capacity to create new proteomic states, macrogenomic engineering is inherently reversible and can thus support the intrinsic capabilities of an organism by increasing or decreasing the access to such states.

1.2. SCOPE OF THESIS PROJECT

The overarching goal of this thesis is to demonstrate the relationship between higher order chromatin scaling (between 20-350 nm) and critical cellular process such as DNA repair, replication, transcription, cell cycle, and proliferation. The thesis is organized as follows: In Chapter 1, we presented a

new technique, Partial Wave Spectroscopic (PWS) microscopy, that gives us the capability to study such critical cellular processes at these lengthscales in label free, live cells in real time. In Chapter 2, we present the findings of molecular dynamics simulations and supporting experimental data indicating that physico-chemical regulation of chromatin packing scaling can be used to influence and alter transcriptional diversity, intercellular heterogeneity, and gene network heterogeneity. This relationship suggests the ability to target chromatin scaling as a means to regulate critical cellular processes and the overall plasticity of cells as they respond to extracellular conditions. In Chapters 3-7, we present three "case studies" of disease states or cellular conditions in which the regulation of chromatin scaling has profound effects on cell function: In Chapter 3, we discuss the role of Sirt1, a histone deacetylase, and its role in regulating chromatin scaling to protect against cardiovascular inflammation. In Chapter 4, we demonstrate that genome structure and compartmentalization can be affected through pharmacological and morphological means to alter stem cell plasticity. In Chapters 5-7, we demonstrate the near-universal link between increased chromatin scaling in early tumorigenesis as well as in cancer cells evading chemotherapy, that appears to be a common denominator of multiple molecular carcinogenesis pathways and mechanisms of action for different chemotherapeutic agents. Furthermore, we show that pharmacological agents can rapidly reduce the spatial variations in chromatin scaling in cancer cells to in turn modulate transcriptional heterogeneity. Finally, in Chapter 8 we summarize our results and discuss the future mechanistic and therapeutic directions of the project as well the overall impact of the ability to control the physicochemical environment within the cell's nucleus to alter chromatin scaling and predictably modulate global patterns in gene expression.
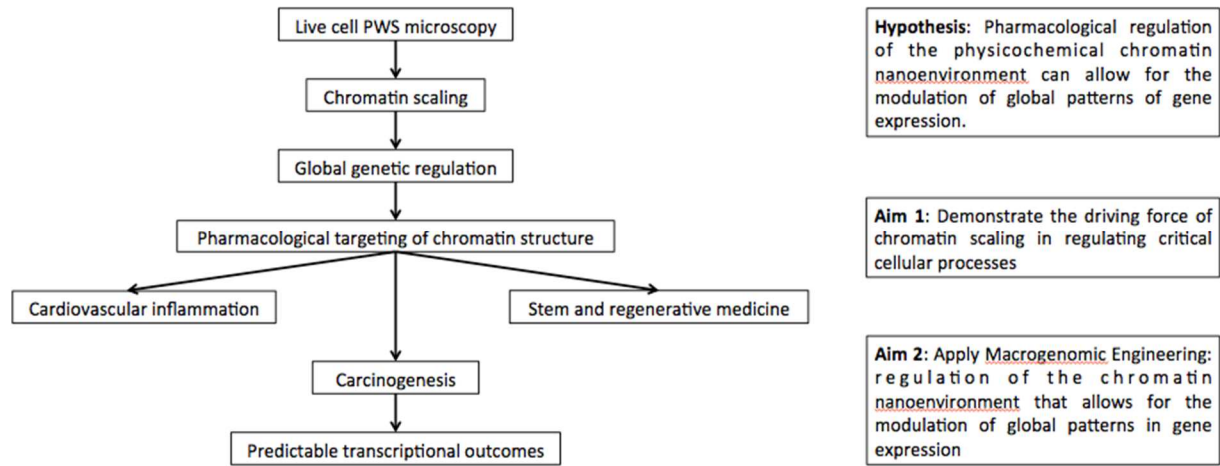
Figure 1.1. *Flow chart of dissertation hypothesis and specific aims.*

Chapter 2: Label-free imaging of the native, living cellular nanoarchitecture using partial wave spectroscopic (PWS) microscopy

This chapter is adapted from Almassalha, Bauer, Chandler, Gladstein et al, PNAS, 2016, reference (38).

2.1. INTRODUCTION

To study the function and interactions of macromolecular structures within the context of the structurally and dynamically complex living cellular systems the ideal live cell imaging technology platform would satisfy five key requirements: (1) nanoscale sensitivity (<200nm), (2) label-free (3) non-perturbing (4) quantitative, (5) high-throughput, and (6) molecularly informative.

Current approaches are unable to meet all these criteria alone. The breakthroughs in super-resolution fluorescence microscopy (SRM) have enabled new imaging technologies capable of providing unprecedented molecular identification at the highest resolutions currently available in live cells. SRM techniques, which include stimulated emission depletion (STED) (39), stochastic optical reconstruction microscopy (STORM) (40), photo-activated localization microscopy (PALM) (41), and structured illumination (SIM), require the use of exogenous fluorophores to visualize macromolecular structures. For some applications, these labels are indispensable to achieve molecular specificity. However, there are significant drawbacks to the exclusive use of molecular labels for studies of cellular structure and function. Exclusively label-based SRM approaches are limited by the number of possible imaging channels, by the high label densities required, by the high light intensities used during imaging, and by the introduction of possible artifacts due to the labels themselves, especially at the high densities required for nanoscale resolution (42, 43). In the study of macromolecular organization, current imaging approaches have significant drawbacks as macromolecular structures are often composed of dozens to hundreds of distinct molecules and often include different subtypes such as lipids, proteins, nucleic acids, and carbohydrates, some of which are difficult to directly label. Due to these limitations, phase contrast microscopy is still the most widely used label-free imaging modality for live-cell experiments. Although this technique is fast and improves contrast to visualize live cells, its diffraction-limited resolution cannot provide any insights into the macromolecular nanoarchitecture. As such, currently no label-free optical technique exists to measure the nanoarchitectural properties of live cells below the diffraction limit.

In diseases like cancer, it is increasingly clear that changes in chromatin scaling at all length scales are a critical determinant of tumor formation, aggressiveness, and chemoresistance. One of the primary features of tumorigenesis is a shift in the fractal physical organization of chromatin, correlating both with the formation of tumors and their invasiveness. In early carcinogenesis, we have previously applied a fixed-cell–imaging technique, partial-wave spectroscopic (PWS) microscopy and transmission electron microscopy (TEM), to detect physical changes in the chromatin nanoarchitecture, indicating that the topology of chromatin is a critical component in cellular function at the earliest stages of tumor formation (44).

Here, we set out to create a label-free live-cell microscopy method based on interference principles used in PWS cytology, thereby creating a tool to directly study the dynamic nanoscale topology of live cells, with a specific focus on studying real-time changes in chromatin organization. We sought to develop an ideal extension of PWS in live cells that would (i) provide nanoscale sensitivity to structures between 20 and 350 nm, (ii) use label-free contrast to capture nanoscopic information, (iii) be nonperturbing to biological samples by using low-power illumination and label-free contrast, (iv) quantify the cellular nanoarchitecture, and (v) rapidly capture the temporal evolution of nanoscale structures, providing contrast in multiple cells in seconds. For studies aimed at understanding the overall structure–function relationship in eukaryotic cells, using SRM approaches alone would not be suitable. The power of live-cell PWS is its unique ability to work in conjunction with existing label-based technologies to provide the structural context for molecular interactions, thereby greatly expanding our understanding of the molecular behavior in live cells (18). With this approach, we demonstrate the ability to measure the nanoarchitecture in live cells in seconds. Specifically, we explore changes to the cellular nanoarchitecture due to UV light exposure, show that live-cell DNA-binding dyes transform chromatin within seconds, and demonstrate a direct link between higher-order chromatin structure and mitochondrial membrane potential.

2.2. MATERIALS AND METHODS

2.2.1. Live-cell PWS imaging

Before imaging, media within the Petri dishes was exchanged with fresh RPMI-1640 media (lacking phenol red pH indicator; purchased from Life Technologies) supplemented with 10% (vol/vol) FBS (Sigma-Aldrich). For DNA fragmentation experiments, live-cell PWS images were acquired at room temperature (22 °C) and in trace CO_2 (open air) conditions or cells subsequently stained with Hoechst 33342. During acquisition of any time series data (UV and controls, metabolic perturbation), cells were maintained at physiological conditions for the duration of the experiment. For imaging, a reference scattering spectra was obtained from an open surface of the substrate coverslip immersed in media before any cellular imaging to normalize the intensity of light scattered for each wavelength at each pixel. We define Σ as the spectral SD of our measured reflectance intensity normalized to this reference scattering spectra from the substrate–media interface. To account for noise due to high-frequency oscillations produced by the lamp, we used a low-pass Butterworth filter before calculation of Σ. For phase contrast imaging, cells were grown and maintained in the same conditions as cells used for live-cell PWS, but images were acquired with a 40Å~ air objective and a transmission illumination beam. Likewise, for wide-field fluorescent imaging, cells were grown in the same conditions but preincubated with Hoechst 33342 for 15 min before imaging. To study the effects of UV illumination on cellular structure and function, cells were continuously exposed to UV light produced from an Xcite 120 LED light source (Excelitas) by removing the 500-nm long-pass filter from the illumination path (measurements were performed in triplicate; n = 19). For Hoechst-induced DNA damage experiments, significance was determined using Student's t test with unpaired, unequal variance on nuclear $\Delta(\Sigma)$ between the conditions indicated in the experiment in both Mathematica, version 10, and Microsoft Excel (Microsoft) with n = 146 for Hoechst-stained HeLa cells from 11 replicates and n = 87 for Hoechst-stained CHO cells from 5 replicates. For mitochondrial membrane depletion experiments, significance was determined using a two-tailed, paired Student's t test on nuclear Σ before and after CCCP treatment using Microsoft Excel (Microsoft) with n = 31 for HeLa cells from six independent experiments and n = 159 for CHO cells from five independent experiments. Each experiment consists of 1–10 independent fields of view for analysis. Sequences of pseudocolored live-cell PWS images were merged into movies using ImageJ. All

pseudocolored live-cell PWS images were produced using Matlab, version 2015b, using the Jet color scheme with the ranges indicated in the figure legend. All cells were purchased from American Type Culture Collection (ATCC) unless otherwise noted and imaged in their cell appropriate media supplemented with 10% (vol/vol) FBS. Human umbilical vein endothelial cells (HUVECs) were purchased from Lonza and grown under cell-appropriate media formulation on poly-L-lysine–coated glass imaging dishes.

2.2.2. Co-localization

Fluorescence colocalization of organelle-specific stains with live-cell PWS imaging was performed through manual image alignment of mean reflectance images produced by live-cell PWS acquisition of unstained cells to the cells at the time of acquisition. Background intensity was removed using ImageJ with using a rolling average of 50 pixels for nuclei and 75 pixels for mitochondria. Threshold intensities for the aligned fluorescence images were then calculated by FindThreshold function in Mathematica, version 10, using Otsu's algorithm. Colocalized images were produced by the binary mapping of fluorescent images for each stain, pseudocolored, and scaled by the live-cell PWS P intensity.

2.2.3. H2A.X phosphorylation

Coregistration of live-cell PWS imaging and DNA strand damage using phospho-histone H2A.X was performed by immunofluorescent staining on three independent experiments. Cells were fixed for 20 min with 4% (wt/vol) paraformaldehyde at room temperature and washed twice with PBS, and a permeabilization/blocking step was performed with 0.1% Triton X-100 in1%BSA (Sigma-Aldrich) for 20 min. Cells were again washed twice with PBS and then incubated with Alexa Fluor 488 conjugated to anti-γH2A.X (serine 139 residue) rabbit monoclonal antibody (Cell Signaling) for 30 min. Following incubation with the antibody, cells were imaged using the FITC-EGFP filter on the live-cell PWS microscope.

2.2.4. Mitochondrial membrane potential perturbation

HeLa and CHO cells were grown and prepared for live cell imaging as previously described. Cell

measurements for a single field of view were sequentially obtained for 3 minutes prior to treatment with protonophore carbonyl cyanide m-chlorophenyl hydrazine (CCCP), a widely used compound for studies of mitochondrial function due to its disruption of mitochondrial membrane potential ($\Delta\Psi$m). CCCP. HeLa (n = 31 from six independent experiments) and CHO (n = 159 from five independent experiments) cells were treated with 10 µM for 15 min and imaged before and after treatment. Mock-treated cells were incubated with 0.01% DMSO to account for the effect of DMSO solvent on the cells. No significant changes were observed in the mock-treated cells for either cell line. Mitochondrial membrane potential, $\Delta\Psi$m, was measured by flow cytometry (BD LSRII at the Northwestern Flow Cytometry Core) for TMRE (purchased from Life Technologies)-stained cells. In brief, cells were trypsinized and immediately stained with 50 nM TMRE for 30 min. Cells were washed twice with PBS after staining and suspended in 1 mL of PBS. CCCP-treated cells were treated for 15 min to replicate conditions during live-cell PWS imaging. At least 20,000 cells were selected by forward- and side-scattering channels for each group, with a double elimination of doublets from the final analysis. Mean TMRE intensity from each replicate population was used for representative comparison between treated and untreated groups.

2.3. RESULTS

2.3.1. Live-cell PWS rapidly provides quantitative nanoscale structural information in living cells

The live-cell PWS instrument is built into a commercial inverted microscope equipped with a broadband illumination and a tunable spectral collection filter. With this configuration, the live cell instrument uses the glass–cell interface to produce the requisite interference signal that allows for the study of underlying nanoscale structure. In brief, the spatial fluctuations of refractive index (RI) produced by the macromolecular density distribution cause backscattering of incident light waves from the sample. Optical interference of the backpropagating light results in wavelength- dependent fluctuations in the acquired spectrally resolved microscope image. The standard deviation of these spectra (Σ) quantifies the internal structure of the sample with nanometer sensitivity (45, 46). In cells, there are numerous variations in macromolecular density due to the spatial organization of macromolecules. Quantification of this nanomolecular density distribution is given by the statistical parameter, Σ, at each diffraction-limited pixel

(45, 46). Σ, and the disorder strength (Ld, which is Σ normalized by sample thickness), are proportional to two crucial characteristics of molecular organization at deeply subdiffractional length scales: the characteristic length scale of macromolecular organization (Lc), and the standard deviation (δn) of the density(45, 46). In a fractal media, such as chromatin, the characteristic length scale of macromolecules can be alternatively evaluated through the fractal dimension, *D*, which is proportional to Σ. Thus, Σ measured from chromatin senses nanoscale changes in its fractal organization. Critically, increase in heterogeneity (i.e., differential compaction) within chromatin by definition produces an increase in D, δn, or Lc. This relation is derived from the properties of fractal media with conserved mass and volume—as compaction increases locally, the variations in mass density (heterogeneity) must also increase. Previous molecular dynamics simulations have further confirmed that increases in δn*Lc correspond to an increase in macromolecular compaction, and experimental results have shown that this increase within the nucleus quantitatively describes an increase in chromatin heterogeneity (44, 47, 48).

As a representation of the nanoscopic topology detected by live-cell PWS, we used as a model 10-nm "beads on a string" chromatin fibers (Figure 2.1A, B) as has been previously described by Kim et al. (47). In this model, we consider changes in the nanoscopic structure of higher-order chromatin that have the same nanoscopic average mass density but have starkly different nanoscale organization: differentially compacted (Figure 2.1A) and diffusely compacted (Figure 2.1B) DNA fibers. In both cases, images produced from conventional light microscopy techniques cannot capture information about the nanoscale topology of these differential states (Figure 2.1C, D). Likewise, although PWS cannot resolve the structures directly, it provides information about their subdiffractional organization. To demonstrate sensitivity to these structures, Σ is computed directly as described by the work of Cherkezyan et al. (45, 46) accounting for the physical properties of the live-cell system. As is shown in Figure 2.1E, differentially compacted chromatin (Figure 2.1A) produces a much higher Σ than diffusely compacted chromatin (Figure 2.1F). Consequently, regions that result in high Σ in live cells would be the heterogeneous, differentially compacted regions likely resulting from the formation of local heterochromatin domains neighboring decompacted euchromatin (Figure 2.1A). Conversely, homogeneous regions of chromatin would result in low Σ. Although this instrument configuration was optimized to allow live-cell imaging with multimodal acquisition, including wide-field fluorescence and phase contrast microscopy, it has an

appreciably weaker reference interference signal than that produced in traditional PWS cytology and a much higher objective collection numerical aperture. Therefore, we validated the nanoscale sensitivity of live-cell PWS by using rigorous finite-difference time domain computations to numerically solve Maxwell's equations without approximations simulating the nanoscale-complex spatial distribution of molecular density in live cells. These computations were used to study the effect of the RI mismatch using sapphire as a high-RI substrate on the interference signal, and to compare the effect of numerical aperture on. The finite-difference time domain (FDTD) simulations enabled us to optimize the configuration of signal acquisition to provide nanoscale sensitivity to intracellular structure at length scale between 20 and 350 nm (38). Without the use of exogenous labels, we can achieve high-contrast images using Σ that delineate nuclei from cytoplasm due to the intrinsic differences in their nanoarchitecture (Figure 2.1G). Due to its multimodal design, exogenous and endogenous labels can be subsequently used to colocalize specific molecular markers or organelles (Figure 2.1H). Live-cell PWS acquisition yields a 3D data cube, I(λ, x, y), where λ is the wavelength and (x, y) correspond to pixel positions across a 10,000-µm2 field of view, allowing multiple cells to be imaged simultaneously. Acquisition of the full cell reference interference spectrum (500–700 nm) for spectral analysis takes under 30 s, with each wavelength collection produced from <100-ms exposures. Using a reduced wavelength approach to subsample the interference spectrum, this can be further reduced to under 2 s per acquisition(49). Even with full spectral collection, as demonstrated in Figure 2.1 I and J, live-cell PWS provides rapid, quantitative visualization of cellular structures within a single field of view for dozens of cells simultaneously for multiple cell lines (Figure 2.1I, 20 HeLa cells captured in ~30 s, and Figure 2.1J, 36 MES-SA cells captured in ~15 s).
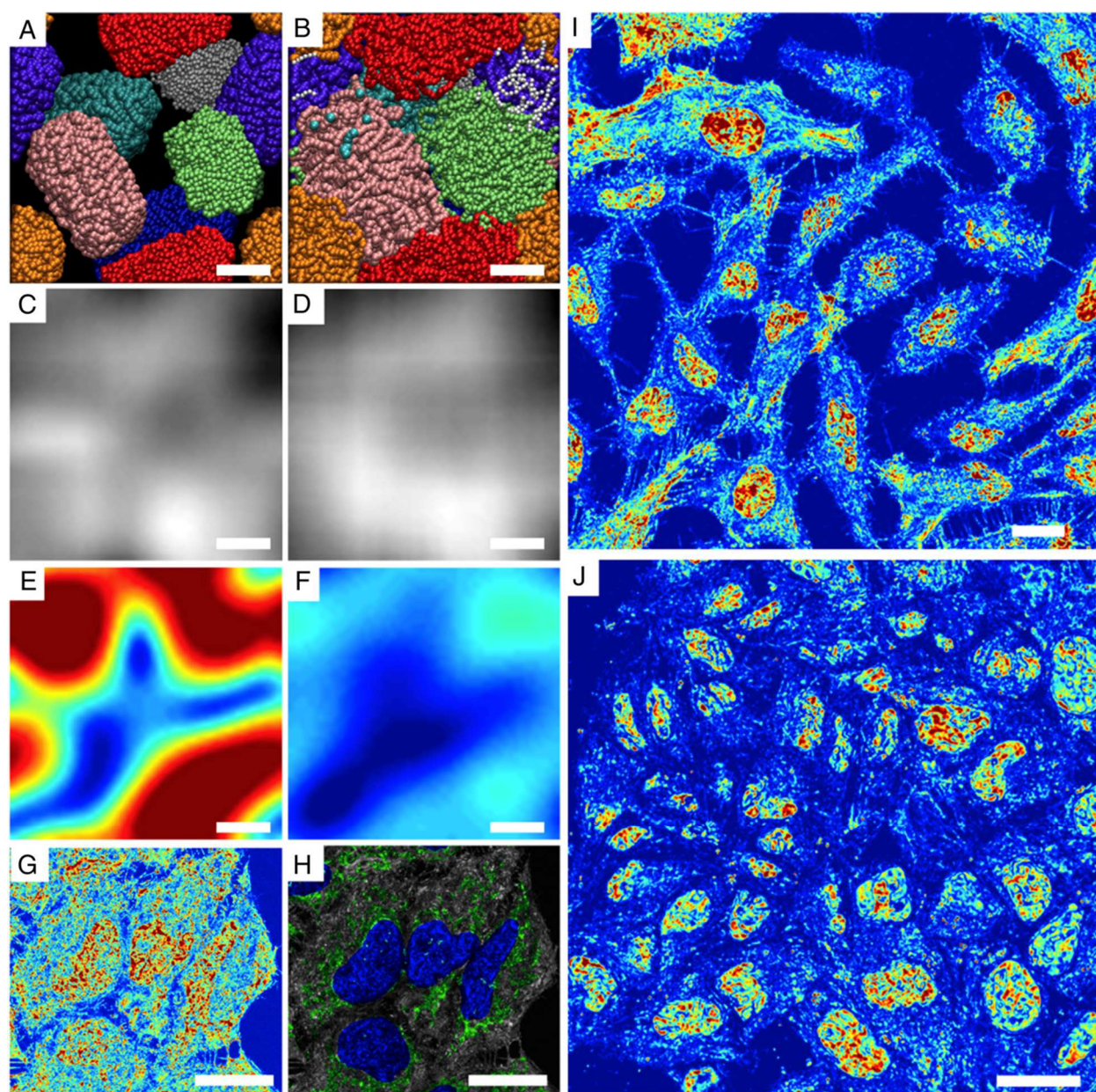
Figure 2.1. *Live-cell PWS rapidly provides quantitative nanoscale structural information of living cells.* A and B) Orthographic z-axis projection of molecular dynamics simulations of chromatin as a 10-nm "beads on a string" polymer capturing (A) differentially compacted (lc = 70 nm) and (B) diffusely compacted chromatin (lc = 20 nm). Scale bar: 100 nm. C and D) Calculated transmission microscope image captured by (C) conventional bright-field microscope from differentially compacted chromatin in (A) and (D) of diffusely compacted chromatin in (B). Images were produced by calculating the average mass density at each pixel, and a Gaussian PSF of 250 nm was applied to simulate a conventional microscope. Grid size of the simulations was 10 nm. E and F) Calculation of Σ captured by live-cell PWS from differentially compacted chromatin in A and diffusely compacted chromatin in B. Σ was calculated directly from the distribution of mass within configurations shown in A and B with Σ = 0.01–0.065. G) Representative pseudocolored live-cell PWS image of HeLa cells with 63Å~ oil-immersion lens, N.A. = 1.4 with Σ scaled to range between 0.0125 and 0.065. H) Colocalization of fluorescence with live-cell PWS image showing mitochondria (green), nuclei (dark blue), and mitochondria–nucleus overlap (light blue). Scale bar: 20 μm.

I and J) Representative pseudocolored live-cell PWS image of (I) HeLa cells and (J) Mes-SA cells demonstrating the capacity to capture nanoscopic information from dozens of nuclei in seconds with Σ scaled to range between 0.01 and 0.05 in I and 0.01 and 0.065 in (J).

Indeed, one of the most critical features of this rapid acquisition is the capacity to directly study the underlying heterogeneity of both chromatin structure and its temporal evolution within the cell population over time. Likewise, as a label-free technique using low illumination intensity, live-cell PWS allows for the study of various time-evolving processes on the structure of cells in general, and chromatin in particular for different cell types over extended periods of time.

2.3.2. Hoechst 33342 excitation induces rapid transformation of chromatin nanoarchitecture uniquely detected by live-cell PWS

Live-cell PWS has a broad utility as a tool for studying the complex relationships between cell function and chromatin nanoorganization. As the initial demonstration, we explored live-cell PWS to rapidly quantify the changes in the nanoscale chromatin structure due to DNA damage. As a demonstration of its ability to detect rapid changes specific to chromatin (within seconds), we explored the transformation of the higher-order chromatin structure secondary to DNA fragmentation using the DNA-binding dye, Hoechst 33342. Damage to DNA results in the formation of DNA fragments and double-stranded breaks (50-52). This damage, in turn, leads to apoptosis or mutagenic transformation. In cancer therapy, many drugs eliminate tumor cells by causing an unbearable accumulation of DNA damage and/or by activating the intrinsic apoptotic pathways (53, 54). Therefore, the identification of DNA fragmentation and understanding of the time evolution of chromatin structure in response to damage are crucial to both understanding DNA repair mechanisms and to identifying chemotherapeutic efficacy. Current techniques to study these processes require cell fixation, such as immunofluorescent identification of the rapidly phosphorylated histone H2A.X (γ-H2A.X) subunit (51) or transfection using photoactivatable proteins (55, 56). Furthermore, fluorescent visualization of cell viability for drug screening often requires the use of cell-permeant minor-groove binding dyes. However, it has been reported that these minor-groove DNA-binding dyes, including Hoechst 33342, induce DNA fragmentation by disrupting the activity of topoisomerase I (57, 58). These effects are observed independently from the

fluorescence excitation of the dye but are accelerated upon UV excitation (58). Consequently, no methods currently exist with the capability for the real-time study of changes to chromatin higher-order structure due to DNA damage or the overall dynamics of the damage response in unlabeled live cells. Using live-cell PWS, we show that the addition of Hoechst 33342 to living mammalian cells transforms the nanoorganization of chromatin at the timescale required for imaging and that subsequent excitation induces fragmentation of the chromatin nanoarchitecture within seconds. This is apparent, as we observe an overall decrease in the Σ after irradiation, suggesting homogenization and decompaction of chromatin across the entire nucleus (Figure 2.2A). Additionally, these effects persist for longer durations, lasting at least 15 min, indicating that the once-fragmented chromatin in the presence of the dye does not immediately reassemble, suggesting these changes could be irreversible. To control for the effects of ionizing UV radiation required for Hoechst excitation, we performed a mock-staining (M-S) experiment where we compared the nuclear changes in cells incubated with Hoechst 33342 to those exposed to UV light alone. In the M-S cells, there was not an observable change in cellular or chromatin structure during the short illumination time required for Hoechst excitation, indicating preservation of the original chromatin structure (Figure 2.2B, C).
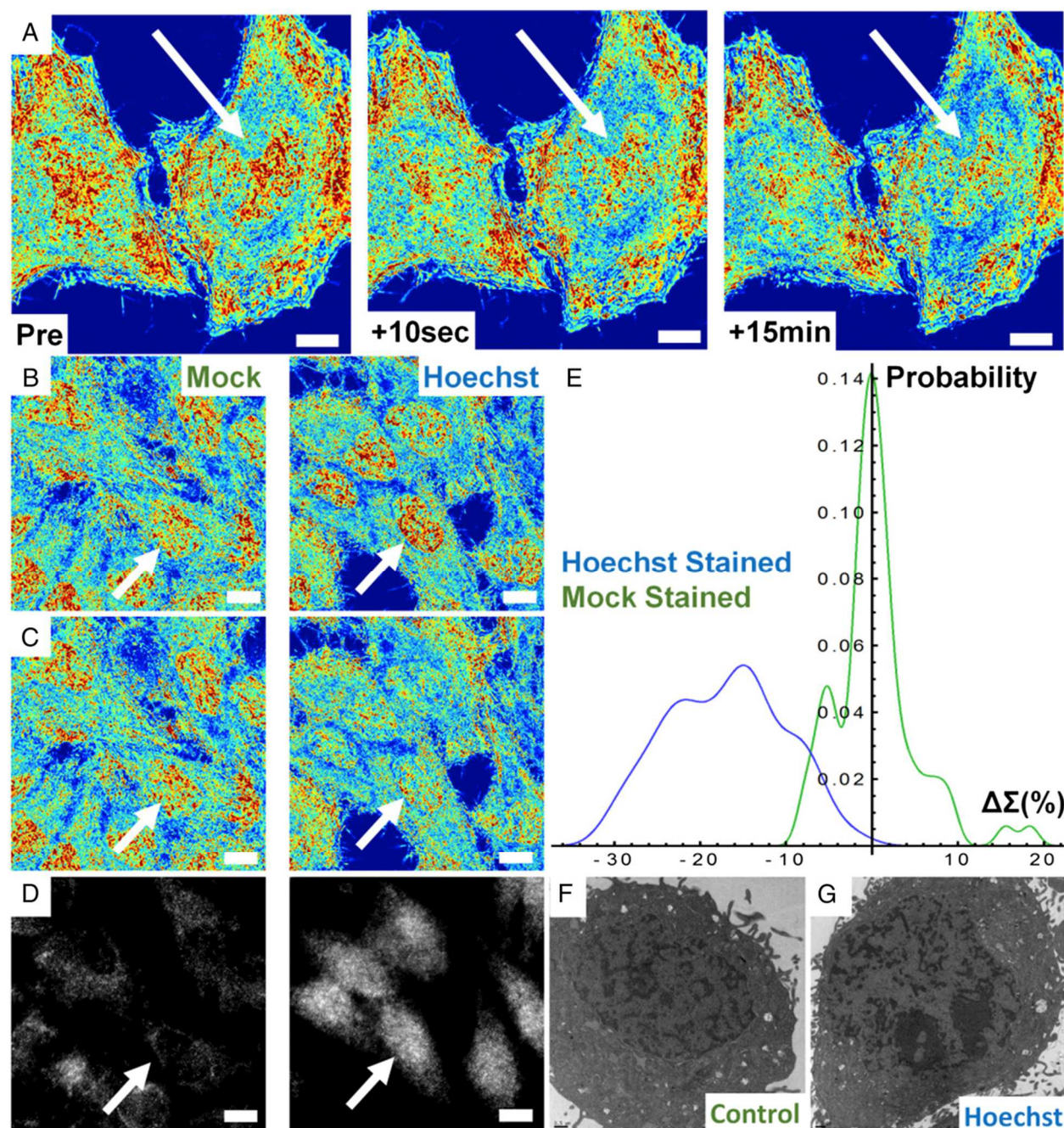
Figure 2.2. *Hoechst excitation induces rapid transformation of chromatin nanoarchitecture.* A) Pseudocolored live-cell PWS image of Hoechst 33342-stained HeLa cells before and after excitation of the dye with UV light. Transformation of chromatin occurs across the whole nucleus within seconds and no repair is observed even after 15 min. B) Hoechst-stained and M-S cells before excitation and (C) the same M-S and Hoechst-stained cells after UV irradiation. D) Minimal (mock) and significant (Hoechst) γH2A.X antibody accumulation. E) Distribution of chromatin transformation after UV excitation for Hoechst-stained and M-S cells. F and G) Transmission electron-microscopic images of control and Hoechst-stained cells confirming nanoscale fragmentation of the chromatin nanoarchitecture in fixed cells. All pseudocolored images scaled between Σ = 0.01 and 0.065. All scale bars: 15 µm. Arrows indicate representative nuclei.

Quantitatively, M-S cells showed no significant change in mean nuclear Σ after a few seconds of UV exposure, whereas the Hoechst-stained cells displayed a 17.01% decrease in HeLa [99% confidence interval, Hoechst (−18.5%, −15.6%); value of P < 0.001] between M-S and Hoechst-stained cells with n = 146 cells from 11 independent experiments for Hoechst-stained cells and n = 68 cells from 6 independent experiments for M-S cells (Figure 2.2B, C). In Hoechst-stained cells, all nuclei demonstrated a negative change in the mean nuclear Σ after UV exposure, whereas the M-S cells displayed a narrow, zero-centered distribution after UV exposure (Figure 2.2E). In both M-S and Hoechst-stained cells, cytoplasmic Σ did not change following UV exposure (value of P > 0.05). Similar results were observed for Chinese hamster ovarian (CHO) cells with M-S cells displaying no change, whereas Hoechst-stained cells experience a −7.1% decrease [99% confidence interval, Hoechst (−9%, −5%); value of P < 0.001 between M-S and Hoechst-stained cells; n = 127 cells for M-S, n = 87 for Hoechst-stained from five independent experiments each], demonstrating this effect occurs independent of the cell type (Figure A1).

Due to this rapid (<10-s) chromatin transformation, we hypothesized that the decrease in the mean nuclear Σ was due to the homogenization of the higher-order chromatin organization caused by DNA fragmentation and the resulting nuclear remodeling. To test this hypothesis, we used a γ-H2A.X-Alexa 488–conjugated antibody to independently monitor the fragmentation of DNA. In Hoechst-stained cells, we observed a drastic accumulation of the γ-H2A.X antibody, whereas we observed little or no localization in the M-S control nuclei (Figure 2.2D). Additionally, TEM on Hoechst-stained and M-S cells exposed to UV light showed an increase in micrometer-scale dense chromatin clumps compared with untreated cells (Figure 2.2F, G). As previous work has shown that DNA damage causes local chromatin expansion(59), this confirmed our hypothesis that immediate DNA fragmentation was induced by Hoechst 33342 excitation, a phenomenon that is detectable by live-cell PWS in real time without the need for exogenous labels.

2.3.3. Live-cell PWS detects dynamics of nanoarchitectural transformation under normal and UV-irradiated conditions

Subsequently, we compared live-cell PWS with phase contrast microscopy to determine whether

live-cell PWS provides information not detectable by other standard, label-free optical modalities (Figure 2.32, B). With phase contrast microscopy, no changes in the cell or nuclear structure were detected after excitation of Hoechst 33342 due to its diffraction-limited resolution (Figure 2.3B). Although electron microscopy cannot be performed on live cells, these experiments demonstrate that photoexcitable molecules disrupt the chromatin nanoarchitecture, which is uniquely detectable in real time in live cells by live-cell PWS.
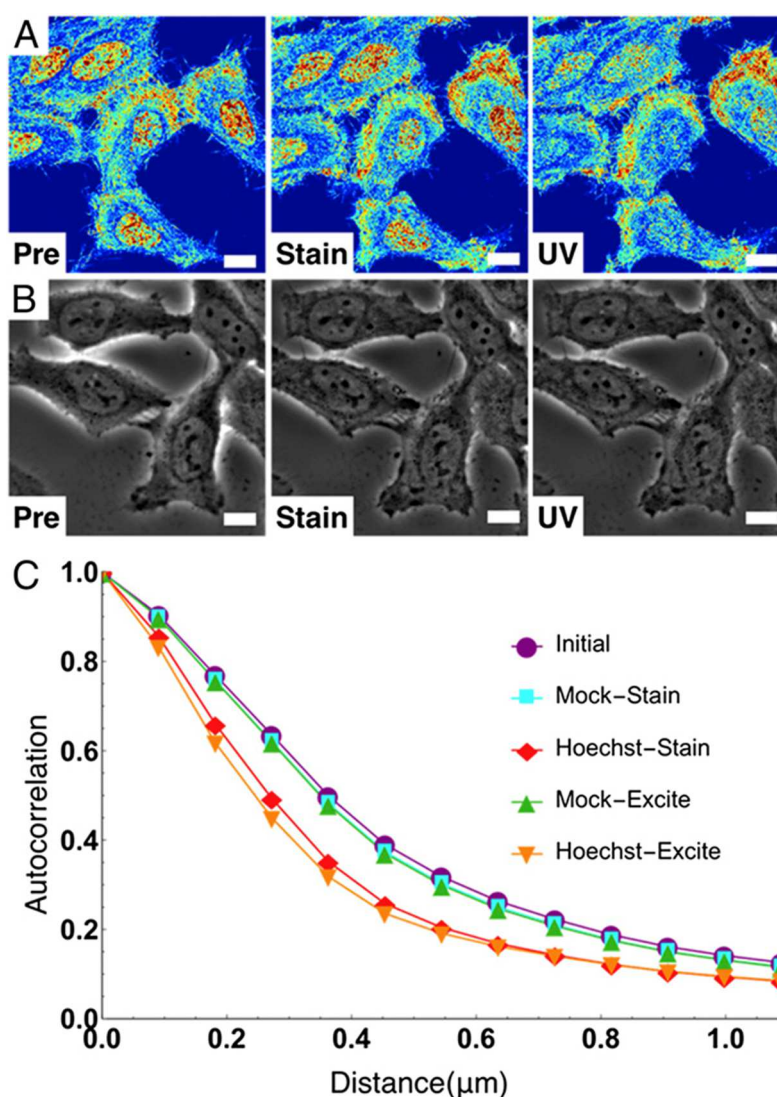
Figure 2.3. *Live-cell PWS uniquely detects nanoarchitectural transformation resulting from Hoechst incubation and excitation.* A and B) Live-cell PWS (A) and phase contrast (B) cells preincubation, 15-min postincubation, Hoechst fluorescent image, and after excitation. C) Change in the autocorrelation function of live-cell PWS intensity. Hoechst transforms chromatin into a more globally heterogeneous structure. Live-cell PWS images are scaled between Σ = 0.01 and 0.065. All scale bars: 15 µm. Autocorrelation analysis was performed by Scott Gladstein, Backman Lab, Northwestern University.

Next, we investigated the effects of Hoechst staining on the spatial transformation of chromatin nanoorganization as measured by live-cell PWS. In particular, we analyzed the spatial distribution of Σ across the nucleus by calculating the 2D spatial autocorrelation, which measures the change in the pixel-to-pixel variability as a function of distance. An increase in the spatial autocorrelation indicates that the nanoscale structure at one pixel has become similar to its neighboring pixels, whereas a decrease indicates a more locally heterogeneous structure. The size of these clusters of similar nanoscale structures was significantly decreased between 100 nm and 1 μm after both the addition of Hoechst and its excitation (n = 40 from three independent experiments) (Figure 2.3C). This indicates an increase in the spatial microscopic heterogeneity of nanoscopic heterogeneity of the nuclear nanoscale structure (Σ) after Hoechst addition and excitation. Consequently, we found that Hoechst causes a global alteration in the chromatin nanoarchitecture independent of its excitation. Not only does this study demonstrate the ability of live-cell PWS to sense the alterations in chromatin structure that were heretofore undetectable in live cells, such as double-strand DNA breaks, but it also illustrates some of the limitations of the extrinsic labeling approaches, such as Hoechst: even though they have traditionally been used for live-cell imaging, these labels alter chromatin structure and lead to DNA damage, which in turn may lead to a perturbation of cell function (Figure A2).

Owing to this sensitivity of live-cell PWS to detect dynamic changes to the chromatin nanoarchitecture due to DNA damage, we next applied it to study the temporal dynamics of the cellular nanoarchitecture under normal growth conditions (Figure 2.4A) in comparison with cells exposed to continuous UV light (Figure 2.4B). UV light is known to cause DNA damage, generate reactive oxygen species, alter receptor-kinase function, and disrupt the cellular membrane. Under normal conditions, chromatin structure can evolve rapidly, with whole-scale changes occurring in minutes (Figure 2.4C). Although the nanoscale topology of chromatin rapidly evolves within any given cell, the organization across the population overall remains stable under normal conditions. In comparison, during continuous UV exposure over 30 min, higher-order chromatin structure is degraded after few minutes of exposure (Figure 2.4D), with pronounced variations in structure over time from cell to cell (with time-lapse measurements performed for three independent experiments).
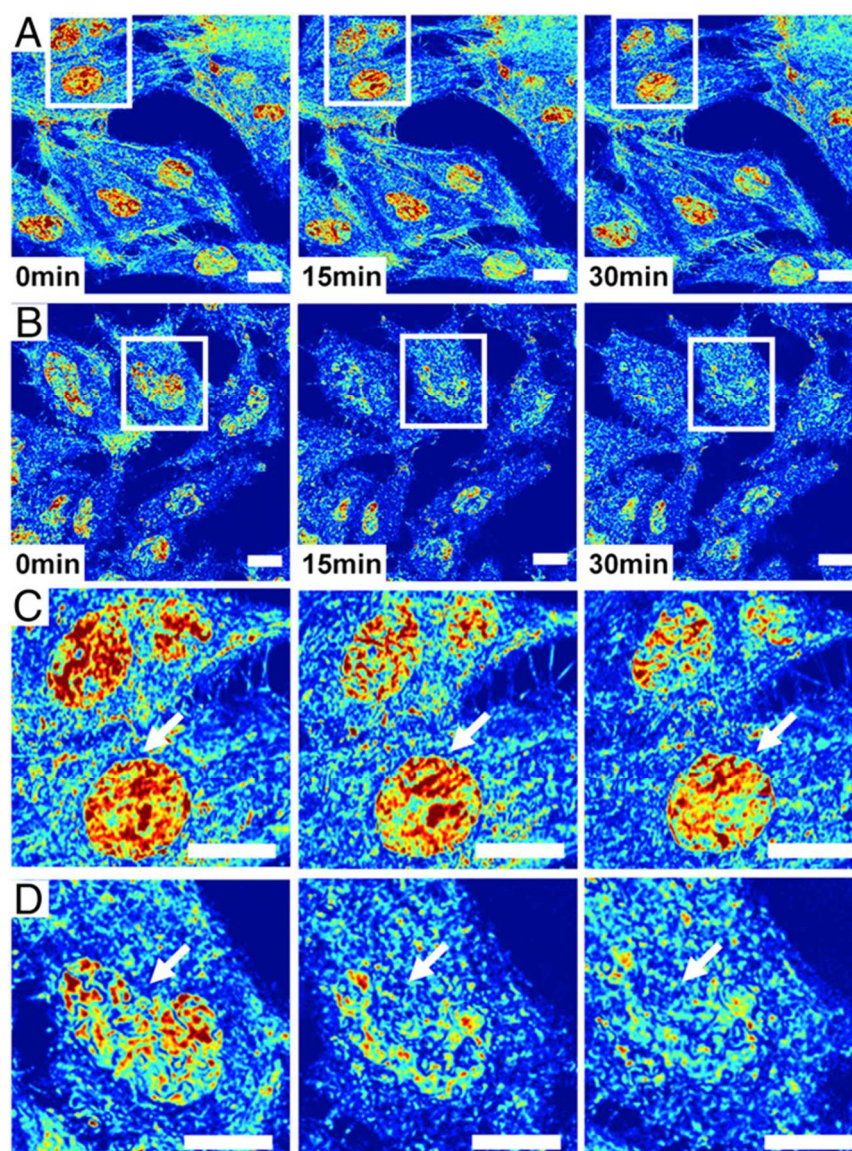
Figure 2.4. *Live-cell PWS detects dynamics of nanoarchitectural transformation under normal and UV-irradiated conditions.* A) Representative field of view displaying seven HeLa cells imaged in ∼15 s using a 63Å~ oil-immersion lens, N.A. = 1.4, with Σ scaled to range between 0.01 and 0.065 over 30 min of imaging. B) Representative field of view displaying seven HeLa cells exposed continuously to UV light imaged in ∼22 s using a 63Å~ oil-immersion lens, N.A. = 1.4, with Σ scaled to range between 0.01 and 0.065 over 30 min of imaging. C) Inset from field of view in A showing the time evolution of two nuclei. Interestingly, chromatin organization is rapidly evolving in time, showing that, even at steady state, the underlying structure changes. D) Inset from field of view in B showing the time evolution of one nucleus under UV illumination. Under UV exposure, homogeneous micrometer-scale domains form within chromatin, lacking their original higher-order structure. Arrows indicate representative nuclei.

Over the course of 2–3 min, there are minimal changes in chromatin and cellular topology due to UV light exposure. However, after ~3 min, the chromatin of some cells exposed to UV light undergoes rapid, directional increase in heterogeneity that corresponds with the formation of micrometer-scale homogeneous domains (Figure 2.4D). Concurrently, the cytoplasm of the cell is transformed, with cell–cell adhesions retracting and a retreating waveform spreading from the cell periphery toward the nucleus. Finally, a near-instantaneous transition occurs within the cytoplasm, with the changes in the cytoplasmic and chromatin nanostructure spontaneously arresting 20 min after exposure. To capture these temporal dynamics in nanostructure, we performed a kymograph analysis using ImageJ of a representative cell exposed to UV light in comparison with a control cell. As is shown in Figure 2.5A, over the 30 min of exposure to UV, micrometer-scale homogeneous domains form within the nucleus and the temporal evolution of nanostructure ceases. In comparison, control cells display continuous transformation, with homogeneous and heterogeneous domains transiently forming and dissipating over the time frame of a few minutes (Figure 2.5B). As is shown in Figure 2.5C, the formation of these large, homogeneous domains that lack higher order structure dominate, resulting in an overall decrease in P (average decrease at 30 min of 26.9% calculated from 19 nuclei from three independent experiments). Interestingly, even under control conditions, some cells rapidly demonstrate global changes in their chromatin topology, possibly due to intrinsic molecular variations or due to differential sensitivity to light exposure. Despite these rapid alterations, the overall chromatin structure of the population displays minimal changes over the course of 30 min (average 0.2% decrease in P from 32 nuclei from two independent experiments; additional control experiments with slower acquisition were not included) (Figure 2.5C). Given the multimodal nature of the current system, these topological variations can be examined and any possible light toxicity further minimized by a variety of well-established methods, including spectral filtration at the illumination source or by using structured illumination.
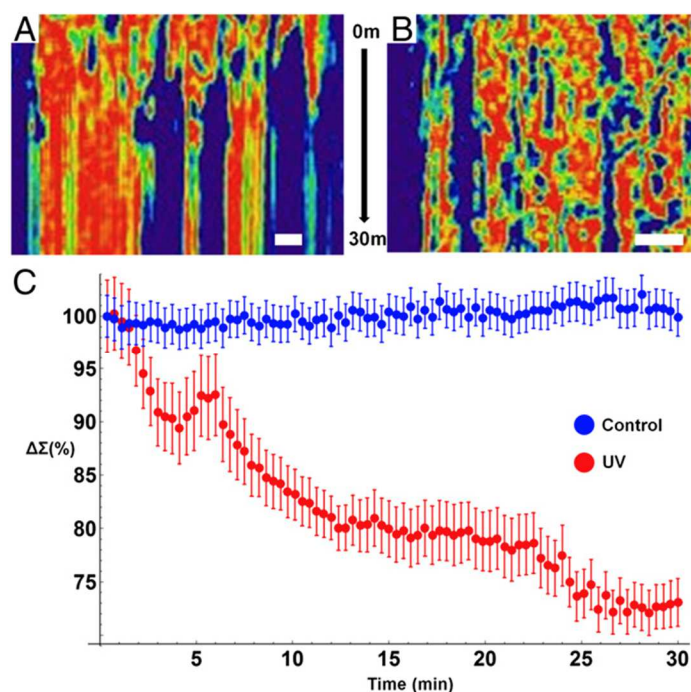
Figure 2.5. *Live-cell PWS detects dynamics of nanoarchitectural transformation under normal and UV-irradiated conditions.* A) Kymograph (with the x axis representing a linear cross-section in x–y plane and the y axis showing changes over time) representing the temporal evolution of chromatin of a cell exposed to continuous UV light. Interestingly, nanoscopically homogenous, micrometer- scale domains form within the nucleus after ~5 min of exposure with an overall arrest in structural dynamics. B) Kymograph representing the temporal evolution of chromatin of a cell under normal conditions. Under normal conditions, the nanoscale topology of chromatin is highly dynamic, with continuous transitions in structure occurring throughout the nucleus. C) Quantitative analysis of nanoscale structure of chromatin of cells under normal conditions (blue, n = 32 cells from two replicates) and exposed to UV light (red, n = 19 cells from three replicates) for 30 min. Exposure to UV light induces overall homogenization of chromatin nanoarchitecture within minutes. Error bars represent SE. Scale bar: 5 µm.

2.3.4. Mitochondrial membrane potential is a direct, rapid regulator of changes in chromatin packing

density heterogeneity

As a final demonstration of the broad utility of live-cell PWS as a tool for studying the complex

relationships between cell function and chromatin nanoorganization, we studied the effect of alteration of

cellular metabolism on higher-order chromatin architecture. The relationship of chromatin structure with

mitochondrial function and metabolism has been a major point of focus in recent years. Studies have

shown that the cellular metabolic activity is intimately linked to cell replication, tumor formation, DNA

damage response, and transcriptional activity (60-63). Therefore, understanding the interplay between

the structural organization of chromatin and mitochondrial function is pivotal to understanding numerous

diseases. Recent fluorescence microscopy studies have suggested that impairment of cellular metabolism induces rapid (<15-min) transformation of chromatin(64, 65). However, these studies often require the production of specialized transfection models (H2B-GFP) or the use of DNA-binding dyes such as Hoechst 33342 and, as such, are limited in their ability to study multiple cell lines and/or over significant periods of time without perturbing the natural cell behavior (64, 65).

To study the link between chromatin structure and mitochondrial function, we used the protonophore, carbonyl cyanide m-chlorophenyl hydrazine (CCCP), which is widely used for studies of mitochondrial function due to its disruption of mitochondrial membrane potential ($\Delta\Psi$m). To explore the role of $\Delta\Psi$m reduction on the immediate transformation of the chromatin nanoarchitecture in live cells, we used two cell lines, HeLa and CHO. Following addition of 10 µM CCCP, HeLa cells rapidly lost $\Delta\Psi$m, whereas CHO cells displayed no significant change as gauged by tetramethylrhodamine (TMRE) fluorescence (Figure 2.6A). Interestingly, after 15 min of treatment with CCCP, we found that addition of 10 µM CCCP produced rapid transformation of chromatin structure in HeLa cells but not in CHO cells (Figure 2.6B). Critically, in HeLa cells, we observed a decrease in nuclear Σ suggesting homogenization and decompaction in the chromatin structure. Conversely, in CHO cells, we observed no statistical change in chromatin compaction and heterogeneity (Figure 2.6C). Quantitatively, HeLa nuclei showed a 10% decrease in mean-nuclear Σ after CCCP (value of $P < 0.001$; n = 31 from six independent experiments), whereas the CHO cells displayed no significant increase in mean-nuclear Σ (n = 159 cells from five independent experiments) (Figure 2.6D). This transformation suggests that the depletion of mitochondrial membrane potential induces rapid decompaction and homogenization of chromatin nanostructure. Disruption of the $\Delta\Psi$m has numerous effects, including the inhibition of mitochondrial ATP synthesis, changes in the production of reactive oxygen species, altered signal transduction, as well as modification of other mitochondrially produced metabolites (i.e., acetyl and methyl transfer groups). Although previous groups have shown that Ψm is an important determinant of cellular proliferation, to date it has not been shown that loss of Ψm has a rapid effect on the global chromatin structure. These results show that the change in Ψm rapidly regulates the nanoscale organization of chromatin, possibly resulting in the observed decreased proliferative potential of cells over time.
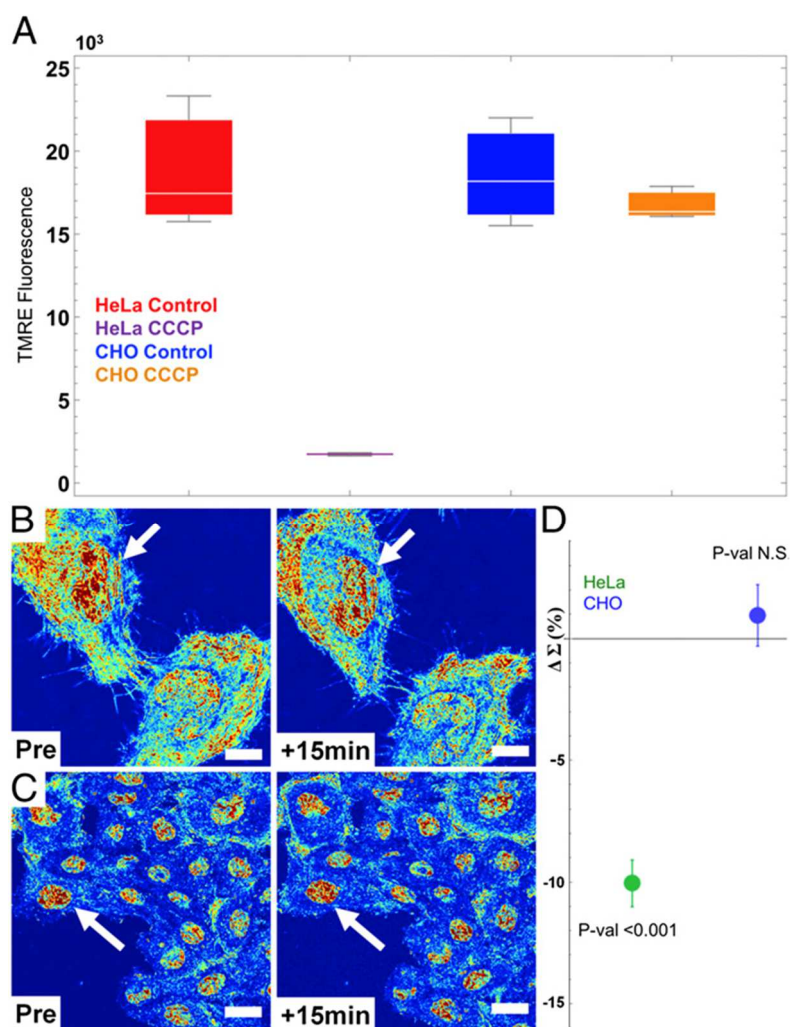
Figure 2.6. *Mitochondrial membrane potential (ΔΨm) is a direct, rapid regulator of chromatin compaction.* A) Flow cytometry showing a 10-fold decrease in HeLa cell TMRE fluorescence after 10 µM CCCP treatment (P < 0.015) and no significant change in CHO cell fluorescence. B) HeLa and (C) CHO cells before and 15 min after CCCP treatment. D) Quantification of the nuclear nanoarchitecture change in HeLa and CHO cells before and after treatment (HeLa = 31 cells, six replicates; CHO = 159 cells, five replicates) with SE bars. Depletion of ΔΨm induces decompaction and homogenization of HeLa but not CHO chromatin. Live-cell PWS images are scaled between Σ = 0.01 and 0.065. All scale bars: 15 µm. Arrows indicate representative nuclei. TMRE fluorescence measurements were performed by Samuel Weinberg, Chandel Lab, Northwestern University.

2.4. CONCLUSION

In summary, we have extended the application of PWS microscopy to the study of temporal dynamics of the cellular nanoarchitecture. Using this technique, we can rapidly quantify the nanomolecular organization in live eukaryotic cells without the use of exogenous labels. Applying this technique to studying the topological changes within the nucleus, live-cell PWS microscopy

predominantly measures spatiotemporal changes in the macromolecular assemblies formed by chromatin because there are no other scaffolding structures present within the nucleoplasm of interphase nuclei within its sensitivity range. As a result, live-cell PWS demonstrates that the nanoscale structure of chromatin evolves rapidly with time, which would significantly transform our understanding of the structure–function relationship between critical processes and chromatin structure, including DNA repair, replication, and transcription. With this technique, we determined that live-cell DNA-binding dyes, such as Hoechst 33342, cause rapid destruction of the higher-order chromatin structure at timescales (seconds) not previously recognized. Paradoxically, this dye is ubiquitously used for the study of cell viability and the presence of DNA damage(66). As a result, live-cell PWS is a powerful tool for studying DNA damage/repair and potentially, chemotherapeutic efficacy in live cells.

Additionally, we showed that live-cell PWS allows for previously limited exploration of the factors affecting the chromatin nano-architecture by demonstrating differential responses in chromatin structure that depend on the mitochondrial membrane potential. In particular, this illustrates that mitochondrial function is intimately related to chromatin structure in real-time and that live-cell PWS can for the first time act as a tool to further investigate the mechanisms of chromatin-metabolic interaction. Live-cell PWS is a natural supplement to super-resolution fluorescence techniques, providing quantifiable information about unstained cellular organization to examine the role of the nano-architecture on molecular interactions in live cells. In the future, we envision that live-cell PWS can be applied to a broad range of critical studies of structure-function in live cells - leveraging the multimodal potential in conjunction with existing SRM to study: (1) the interaction between chromatin structure and mRNA transport; (2) the accessibility of euchromatin and heterochromatin to transcription factors (67, 68); (3) the relationship between chromatin looping, as measured by techniques such as Hi-C, to the physical chromatin structure (7, 9, 69); (4) why and how high-order chromatin structure changes in cancer(7); (5) the role of nuclear architecture as an epigenetic regulator of gene expression (7, 9, 69); (6) the effect of metabolism on chromatin structure(63, 70); and (7) the role of chromatin dynamics in stem cell development (71, 72).

Chapter 3: Chromatin polymer and its ability to affect critical cellular processes

This chapter is adapted from Almassalha, Bauer, Wu, et al, Nature Biomed Eng, 2017, reference (15).

3.1. INTRODUCTION

The 3D organization of the genome is the subject of active research (2, 9, 13, 47, 73, 74). The emerging picture is that the genome is a disordered polymer packed into a variety of domains. As the chromatin polymer folds inside the nucleus, the resulting chromatin packing density is highly non-uniform throughout the genome. Locally, chromatin packing density has a non-monotonic effect on the probability of gene expression, enhancing the rates of expression at chromatin packing densities below ~35% of chromatin volume concentration and suppressing expression at higher chromatin densities due to the competing effects of two consequences of molecular crowding, increased binding of transcriptional complexes and suppressed diffusion. A more nuanced but even more significant effect is driven by the scaling of chromatin packing density (D) across 20-350nm length scales (corresponding to approximately the kbp – Mbp range). As in many other polymeric systems, chromatin packing scaling defines the relationship between the genomic length and the physical packing of a chromatin domain. In turn, chromatin scaling affects the local distribution and the heterogeneity of chromatin density and the probability of genes being accessible to transcriptional factors. Recent evidence indicates that chromatin packing scaling modulates transcriptional diversity (the dynamic range of gene expression), intercellular variation in gene transcription, and gene network heterogeneity (Figure 3.1) (15, 17). In other words, chromatin packing regulation affects cells' transcriptional access to their genomic space. An abnormal 3D organization of chromatin facilitates diseased cells' ability to dynamically change their gene expression patterns, explore a greater genomic landscape, and increases the probability of developing new transcriptional states. This may help cells to develop new traits beneficial to their survival.
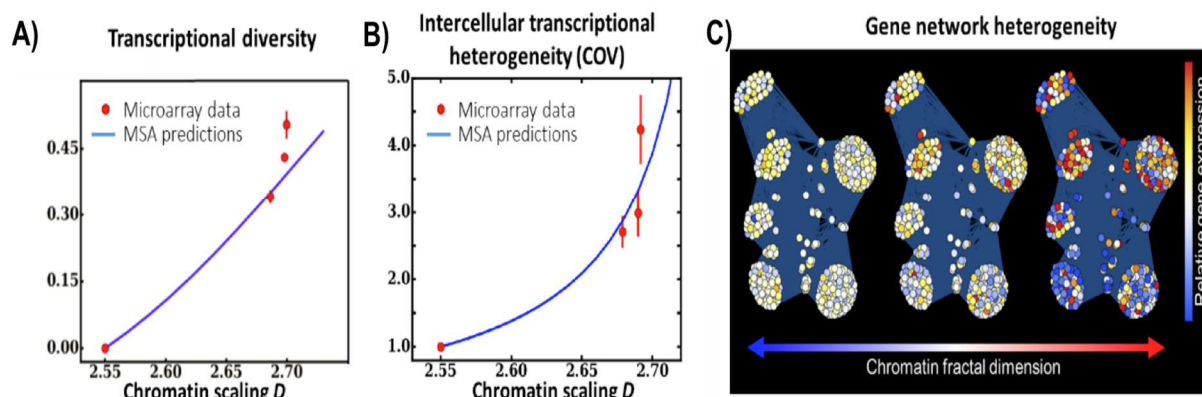
Figure 3.1. *Increasing chromatin packing scaling, D, increases relative transcriptional diversity, relative intercellular gene expression heterogeneity, and gene network heterogeneity.* Relative differences in chromatin scaling were measured 30 minutes after a stimulation (SE, EGF or PMA) was applied using PWS microscopy on the same cells before and after the stimulation. Microarray data was obtained from cell populations treated with the same stimulation conditions. A) Large groups of genes (>100 per group) follow a well-defined pattern that is dependent on their initial expression and the overall chromatin scaling while appearing to be independent of the perturbation mechanism. An increase in D corresponds to an increase in the dynamic range of gene expression. B) Coefficient of variation of intercellular gene expression. Model predicted coefficient of variation for intercellular gene expression as a function of D (blue curve) and the coefficient of variation for intercellular gene expression calculated based on the experimental microarray data (red dots). The result is normalized by the coefficient of variation of cells with the lowest D. Error bars are the standard error of the coefficient of variation of 1,000 genes for each condition. C) Gene network heterogeneity. The standard deviation of expression for genes within a given network increases with increasing D. Microarray analysis was performed by Luay Almassalha, Backman Lab, Northwestern University. Modeling predictions were performed by Wenli Wu, Backman Lab, Northwestern University.

Chromatin heterogenization does not compel diseased cells to change their genome in any specific way; it simply modulates the barrier for functional changes to occur. For example, throughout tumor progression cancer cells must keep developing new traits, be it the induction of angiogenesis or finding strategies to evade the immune system, and chromatin heterogenization facilitates this process.

By leveraging methods of nanoimaging, computational modeling, and molecular biology to understand the principles of physico-chemical regulation of chromatin packing, we have begun to study the spatio-temporal changes in chromatin packing (15, 75), and how they relate to gene transcription and other critical cellular processes in the context of realistic chromatin nanoenvironment (16, 76). Leveraging multi-scale analysis models and nanoimaging, we can mechanistically interrogate the role of chromatin packing in the regulation of gene expression (15). In particular, chromatin packing scaling depends on the ATP-dependent chromatin loop extrusion, which folds a small portion of the genome into

loci-specific topologically-specific domains (TADs)(77) as well as on physico-chemical interactions, namely the balance between chromatin self-interaction and chromatin-nucleoplasm interactions, which in turn depend on chromatin nanoenvironment (local crowding, pH, ionic nanoenvironment) and histone modifications.

We have demonstrated, both computationally and experimentally, that physico-chemical regulation of chromatin packing scaling can be used to manipulate transcriptional diversity, intercellular heterogeneity, gene network heterogeneity, and modulation of the pathway-activated changes in the rates of gene expression. This chromatin packing regulation has broad implications in the ability to regulate critical cellular processes and the overall plasticity of cells as they respond to extracellular conditions.

3.2. METHODS

3.2.1. Microarray transcriptional analysis

Cells were serum starved for 5 hours prior to being treated with 10%FBS (SE), 100ng/ml epidermal growth factor (EGF), or 100ng/ml phorbol 12-myristate 13-acetate (PMA). Live cell PWS microscopy measurements were performed on HT-29 cells grown on 5mm glass bottom petri dishes (Cell Vis) and serum starved for 5 hours before and after stimulation (16). Changes in gene expression for each treatment group were measured using Illumina human HG12-T microarray chips of mRNA collected by TRIzol® isolation (Life Technologies, Carlsbad California) from 10mL petri dishes. Quality check and the probe level processing of the Illumina microarray data were further made with R Bioconductor package, lumi by the Northwestern Genomics Core(78). Analysis of network heterogeneity was performed on 2445 differentially expressed genes using Mathematica® v10.

For gene network analysis, a total of 471 genes were selected based on their ontology groups (Cell Cycle, Proliferation, Apoptosis, Transcription, Signal Transduction, Cell Differentiation) using inbuilt GenomeData®, matching the annotated genes with these processes. Transcriptional heterogeneity for each process was measured by analyzing the relative gene expression for each gene in reference to the expression of the serum starved cells. Relative differences in chromatin packing-density heterogeneity were measured 30 minutes after stimulation (SE, EGF, or PMA) was applied using PWS microscopy on the same cells before and after the stimulation. The difference between the two measured values of Σ

($\Delta\Sigma$) was obtained from over 50 cells per condition and was observed to be on average: 0.1% for SE cells, 0.77% for EGF cells, and 8.49% for PMA cells.

3.2.2. BrdU staining

1 hour pulse-chase BrdU (Sigma Aldrich, St. Louis Missouri) staining was performed according to the immunofluorescence protocol for labeling with BrdU antibody from Cell Signaling Technology. BrdU was prepared in fresh growth media at 37°C at a final concentration of 0.03 mg/mL. Cells were incubated with the BrdU solution for 1 hour at 37°C. Media was then removed, cells were washed with cold 70% ethanol, and the cells were fixed for 5 minutes at room temperature in 70% ethanol. After fixation, cells were rinsed with PBS and incubated at room temperature for 30 minutes in 1.5M HCl. Cells were washed 2x for 5min with 1x PBS prior to blocking and immunostaining.

Cells were incubated for 60 minutes in a blocking buffer (1X PBS / 5% normal goat serum/ 0.3% Triton X-100). The blocking solution was removed and the cells were incubated overnight at 4C in primary mouse monoclonal antibody diluted 1:1400 in 1X PBS / 1% BSA. The following day cells were washed with PBS and incubated for two hours at room temperature in Alexafluor-488 goat anti-mouse secondary antibody diluted 1:1000 in 1X PBS / 1% BSA. Following a final PBS rinse, slides were mounted with Prolong® Gold Antifade Reagent and coverslips.

3.3. RESULTS

3.3.1. Chromatin scaling and genome connectivity

While live-cell PWS microscopy offers a novel means to study chromatin scaling genome organization and the function and interactions of macromolecular structures within the context of the structurally and dynamically complex living cellular systems, it is also important to contextualize data obtained with live-cell PWS to other techniques used to study nuclear organization. Hi-C is a chromosome capture technique that in recent years has provided insight into genome organization through the characterization of chromosome territories and genome wide compartments (9). One way to express this genome compartmentalization is through the contact probability $P_c(x) \sim x^{-S}$ (where S is the

contact probability exponent) between distinct loci on the genome separated by a distance x that would otherwise be less likely to come into contact. In fact, we can compare one number, the average contact probability across the entire genome, to the average chromatin scaling across the nucleus. Recalling that in a fractal media such as chromatin, Σ as measured by PWS is proportional the fractal dimension, D, we have derived and seen an inverse relationship between S (as measured by Hi-C) and D as measured by PWS (Figure 3.2).

Using a Hi-C data set for BJ fibroblast cells treated with dexamethasone, we observed loss of long-range contact probability with dexamethasone treatment as measured by Hi-C as well as a decrease in chromatin scaling as measured by PWS (Figure 3.2A). We saw the same inverse relationship between S and D with a second dataset on TNFα -treated IMR90 human lung cells (79). Both PWS and Hi-C data showed a comparable decrease in the contact probability exponent S (Hi-C) and an increase in scaling D (PWS) after 1 hour of TNFα treatment (Figure 3.2C-E). These results indicate that contact probability profiles are driven, to a large extent, by chromatin packing properties, which in turn affect and are affected by gene-specific compartmentalization mechanisms that delineate TAD boundaries.
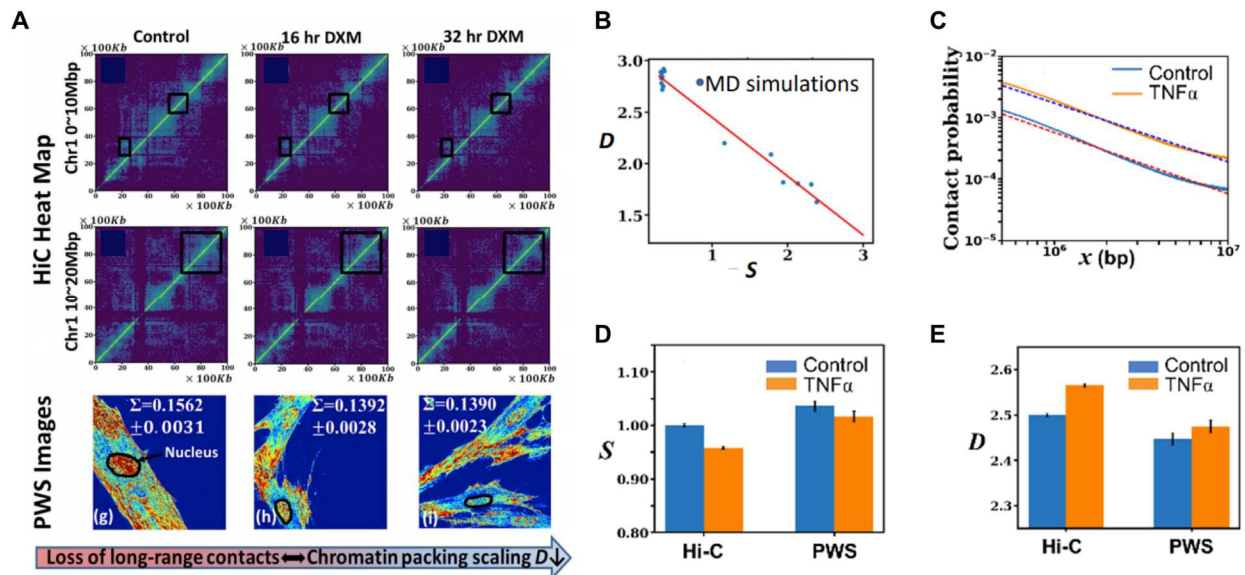
Figure 3.2. *Relationship between chromatin scaling and genome connectivity*. Molecular dynamic simulation of chromatin packing established a relationship between the contact probability exponent S (e.g. experimentally measured using Hi-C genome mapping) and chromatin packing scaling D (e.g. experimentally measured by PWS or ChromEMT). Chromatin was modeled as the self-avoiding polymer

with 1,000 nucleosomes (~0.2Mbp ~ average TAD size) with a non-specific Lennard-Jones attractive potential $V=4\varepsilon[(\sigma/(r-\Delta))^{12}-(\sigma/(r-\Delta))^{6}]$ with the depth of the potential wall ε, the monomer diameter Δ, the intermonomer center to center distance r, and $\sigma=1.12\Delta$. D was varied by changing ε (from 0 to $2kT$). 10^7 conformations were generated for each potential. S and D were found from the following relationships: $P_c(x)$ is proportional to x^{-s} and $Rg(N)$ is proportional to $N^{1/D}$, where Rg is the radius of gyration for a polymer with N monomers. $S\approx3/2(D-1)$. A) HiC and PWS measurements on BJ fibroblast cells show loss of long-range contact probability and decrease of chromatin heterogeneity when treated with dexamethasone (DXM). HiC heat maps of BJ cells before, after 16 hours and after 32 hours of DXM treatment (top and middle rows) indicate a change in long-range interactions in chromosome 1 between 0 and 10 Mbp after DXM administration (top tow). HiC maps of chromosome 1 between 10 Mbp and 20 Mbp with a black square in each image indicate TADs with the largest change of long-range contact probabilities across treatments (middle row), but both genomic ranges show the loss of long-range contact probability with dexamethasone treatment. PWS measurements of Σ for cell nuclei at 0, 16, and 32 hours after DXM treatment (bottom row) show decreased average intranuclear Σ (100 cells per condition) after DXM treatment indicating a DXM-induced decrease in chromatin heterogeneity of BJ cells. B) Molecular dynamic (MD) simulation of chromatin packing established a relationship between the contact probability exponent S (experimentally measured using Hi-C genome mapping) and chromatin packing scaling D (experimentally measured by PWS or ChromEMT). C-E) Experimental validation of the relationship between S and D. IMR90 cells were treated with TNFα, which modulates TAD organization. S was calculated from Hi-C data(79) before and 1 hour after TNFα treatment and compared with D measured in live cells by PWS for the same treatment condition. Error bars are standard error for $N=95$ control and 86 TNFα-treated IMR90 cells as measured by PWS (***$P<0.001$). Hi-C analysis and molecular dynamics simulations were performed by Wenli Wu, Backman Lab, Northwestern University.

3.3.2. Chromatin packing domains and transcription

Another important relationship is that between chromatin scaling and transcriptional activity. We have already discussed the relationship between increases in scaling and their global transcriptional consequences, but we must also consider the relationship between the degree of chromatin scaling, regions of heterochromatin and euchromatin, and their associated transcriptional profiles. Recently, we have made use of the multimodal functionality of PWS to pair structural information on chromatin (through PWS measurements) with the exact location of specific molecules of interest (through STORM measurements) to begin to better understand this relationship. Specifically, we colocalized label-free PWS with 15nM resolution STORM labeled for active RNA polymerase II (Pol II) (Figure 3.3). Initially, we sought to identify the relationship between PWS packing domains and overall active transcription throughout the nucleus. Our results indicated that spatially distinct chromatin packing domains correlate with markers of active gene transcription. PWS measurements showed a number of 200-300nm chromatin regions with elevated chromatin scaling, and STORM colocalization showed that Pol-II tended to localize within and around these packing domains with elevated scaling and not in between them (Figure 3.3D).
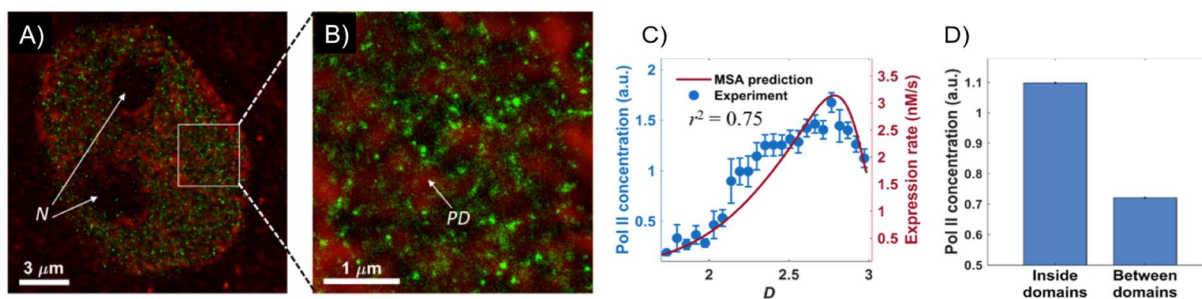
Figure 3.3. *Spatially distinct packing domains correlate with markers of gene transcription.* A, B) Co-registered label-free PWS and labeled STORM of nuclear chromatin in M248 cells. Red: chromatin packing domains (PD; PWS). Green: labeled active RNA-polymerase II (Pol II; STORM); 15nm resolution. N–nucleolus. C) Concentration of Pol II associated with packing domains increases with the scaling of the PDs indicating a higher transcriptional activity within domains with a higher D, in agreement with the Multi-Scale Analysis (MSA) of transcription modeling predictions. D) Pol II tended to localize within packing domains. STORM was performed by Adam Eshein, Backman Lab, Northwestern University.

These results are in agreement with Multi-Scale Analysis (MSA) modeling predictions (summarized in section 3.1) that indicate that the concentration of Pol-II associated with packing domains increases with the scaling of the packing domains (Figure 3.3C). Plotting the scaling of each of these domains against the concentration of Pol II at that domain, we saw an increase in Pol II concentration up to a scaling, *D*, of about 2.7 and then a decrease in the Pol II concentration with an increasing *D* above 2.7. This nonmonotonicity and the fact that Pol II concentration above 2.7 decreased with increasing D led us to hypothesize that heterochromatin, associated with gene repression, would have a higher *D* than euchromatin. Other labs have reported similar observations obtained from alternate techniques such as volume exclusion and diffusive hindrance measurements using inert fluorescent tracers (67) as well as packing measurements through the quantification of radius of gyration (3).

To interrogate the role of compounds that alter chromatin scaling in changing chromatin domain organization (with respect to heterochromatin, facultative heterochromatin, and euchromatin), we next performed immunofluorescent staining on A2780 ovarian cancer cells with markers of heterochromatin (HP1α) and facultative heterochromatin (H3K27me3). When compared to control A2780 cells, we observed that compounds that decrease chromatin scaling (digoxin, celecoxib, valproic acid, see section 3.3.5 for more details) also lead to decreased levels of both heterochromatin (Figure 3.4A, B) and heterochromatin (Figure 3.4C, D) after 48 hours of treatment. Future experiments will also look at the effect of these compounds on euchromatin levels and will colocalize PWS and STORM for all three labels

to determine spatially exactly how chromatin packing domains (as measured by PWS) correlate to these markers of heterochromatin, facultative heterochromatin, and euchromatin.
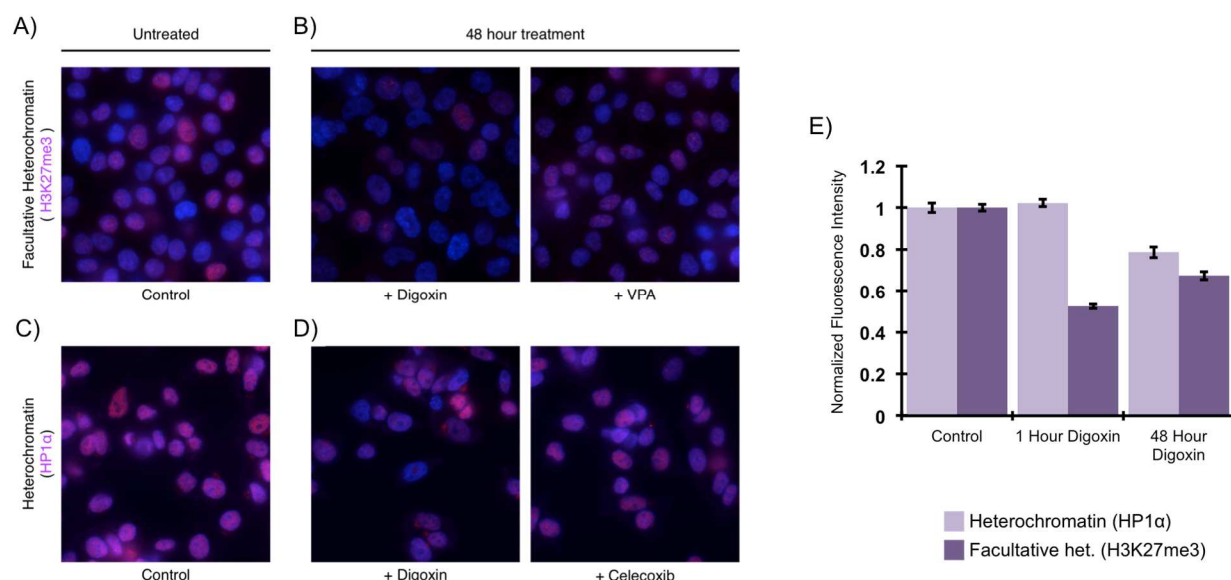
Figure 3.4. *Decrease in chromatin scaling is coupled to a decrease in heterochromatin and facultative heterochromatin.* A, B) Representative fluorescent microscopy images of A2780 cells stained for facultative heterochromatin either untreated (A) or treated for 48 hours with 100nM digoxin or 100uM valproic acid (VPA) (B). Cells are stained with DAPI (blue) and H3K27me3 (purple), a marker for facultative heterochromatin. Digoxin and VPA, both compounds that lead to a reduction in chromatin scaling, also lead to a decrease in the average amount of facultative heterochromatin in the nucleus. C, D) Representative fluorescent microscopy images of A2780 cells stained for heterochromatin either untreated (C) or treated for 48 hours with 100nM digoxin or 75uM celecoxib (D). Cells are stained with DAPI (blue) and HP1α (purple), a component of heterochromatin that binds H3K9me, leading to epigenetic repression. Digoxin and celecoxib, both compounds that lead to a reduction in chromatin scaling, also lead to a decrease in the average amount of heterochromatin in the nucleus. E) Quantification of changes in heterochromatin (HP1α) and facultative heterochromatin for 100nM digoxin-treated A2780 cells indicates a 48% decrease in facultative heterochromatin and no change in heterochromatin after 1 hour of treatment and a 22% decrease in heterochromatin and 33% decrease in facultative heterochromatin after 48 hours of treatment. Average fluorescent intensity of heterochromatic stains is normalized to DAPI for each cell and each treatment population is normalized to the untreated control group to determine relative change in HP1α and H3K27me3 for each time point.

3.3.3. Chromatin scaling and cell cycle

One of the key features of all live cell cultures is their progression through the cell cycle. Each stage of the cell cycle brings changes to the organization of chromatin within the nucleus, with perhaps the most distinct changes occurring during S-phase, the phase when the entire genome is replicated in preparation for mitosis. To determine the sensitivity of PWS to changes in chromatin scaling associated with S-phase, we first employed bromodeoxyuridine (BrdU), a synthetic nucleotide incorporated into DNA

instead of thymidine during S-phase. Briefly, 1 hour pulse-chase BrdU staining was performed. BrdU was prepared in fresh growth media at 37°C at a final concentration of 0.03 mg/mL. Cells were incubated with the BrdU solution for 1 hour at 37°C. Media was then removed, cells were washed with cold 70% ethanol, and the cells were fixed for 5 minutes at room temperature in 70% ethanol. After fixation, cells were rinsed with PBS and incubated at room temperature for 30 minutes in 1.5M HCl. Cells were washed 2x for 5min with 1x PBS prior to blocking and immunostaining.

Cells were incubated for 60 minutes in a blocking buffer (1X PBS / 5% normal goat serum/ 0.3% Triton X-100). The blocking solution was removed and the cells were incubated overnight at 4C in primary mouse monoclonal antibody diluted 1:1400 in 1X PBS / 1% BSA. The following day cells were washed with PBS and incubated for two hours at room temperature in Alexafluor-488 goat anti-mouse secondary antibody diluted 1:1000 in 1X PBS / 1% BSA. Following a final PBS rinse, slides were mounted with Prolong® Gold Antifade Reagent and coverslips.

By sorting cells based on BrdU staining, we were able to quantify population averages of chromatin scaling for cells in S-phase compared with those in other phases of the cell cycle. It should be noted that PWS is not sensitive to cells in M-phase as this phase involves slight detachment from the glass interface while a cell divides. After division, the two cells reattach firmly to the glass substrate, and PWS is once again sensitive to the cells in G0/G1 phase. When using BrdU staining to group cells into unsorted, S phase, and G-phase (a combination of G1- and G2-phase) populations, we observed no significant difference in chromatin scaling between these populations (Figure 3.5). Despite the seemingly substantial changes in chromatin composition that occur during S-phase, replication occurs at several distinct loci across the nucleus over the course of the entire S-phase and not simultaneously across the whole nucleus (80). Additionally, the distribution of replication foci changes over the course of S-phase (80). Further studies could make use of higher resolution fluorescent imaging in combination with PWS to look at the spatial arrangement of chromatin within the nucleus to see how chromatin scaling changes locally throughout S-phase. However, on average S-phase does not have globally and significantly altered chromatin scaling compared to that of the entire population or to that of the G-phases.
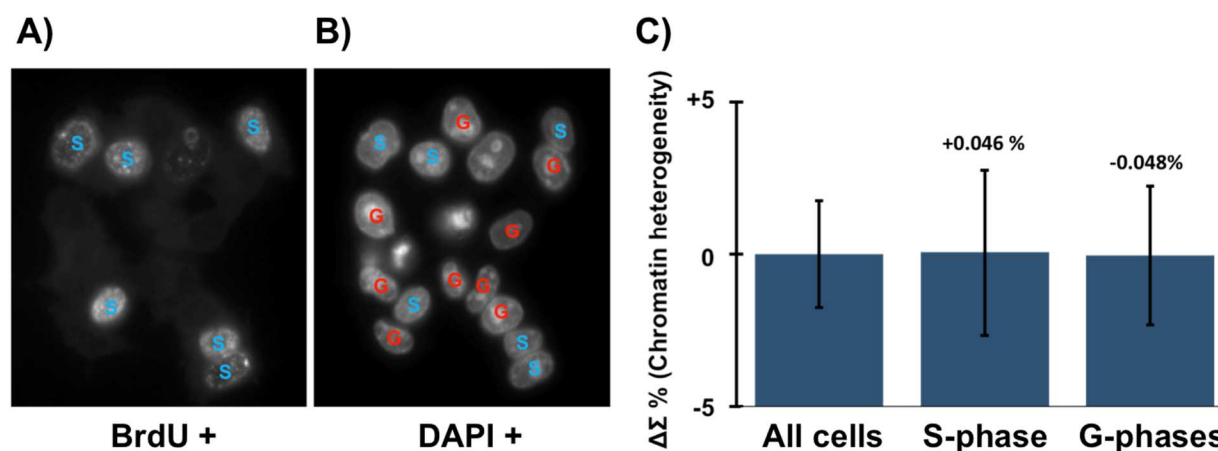
Figure 3.5. *Average population chromatin heterogeneity unaffected by cell cycle*. PWS quantification of average chromatin heterogeneity was compared for total, S-phase, and G1- and G2-phase populations. A) BrdU+/DAPI+ cells were determined to be in S-phase. B) BrdU-/DAPI+ cells were determined to be in either G1- or G2-phase. PWS is not sensitive to cells in M-phase. C) No difference was observed in the average chromatin chromatin heterogeneity between any of these sub-populations.

We further wanted to confirm that all PWS measurements of chromatin scaling were, at the population average level, cell-cycle independent. Several compounds have been identified that significantly change chromatin scaling (see section 3.3.6) but also have been implicated in altering the cell cycle.

Celecoxib, for example, has been shown to lead to concentration dependent cell cycle arrest. At higher CPX concentrations, such as the 75uM we have employed in our studies, it has been shown to lead to G2/M phase arrest. To show that chromatin scaling is not just a measure of cell cycle, we employed the FUCCI Cell Cycle fluorescent indicator system, which utilizes red fluorescent protein (RFP) and green fluorescent protein (GFP) fused to two different regulators of the cell cycle: CDT1 and Geminin. In the G1- and S-phases of the cell cycle, Geminin is degraded and thus only CDT1 tagged with RFP is present. In the G2-, and M-phases, CDT1 is degraded and only Geminin tagged with GFP remains. During the G1-/S-phase transition, CDT1 levels are decreasing and Geminin levels are increasing so both proteins are present, and overlaid fluorescent images appear yellow (Figure 3.6A).

Using the FUCCI system, we do indeed see a modest shift in the population of cells in the G2/M phase. However, when we analyze PWS results from the entire celecoxib treated population, we see no difference compared to the cell cycle-segmented populations (Figure 3.6B). Thus, at the population level,

we do not see any differences in chromatin scaling (at these length scales) associated with cell cycle. However, the fact that the average population chromatin scaling is unaffected by cell cycle (Figure 3.5) in conjunction with the FUCCI cell cycle distribution data indicates that changes in chromatin scaling observed with PWS are independent of cell cycle. For future studies, the combination of PWS measurements on chromatin scaling and cell cycle distribution measurements will have tremendous power when paired together to provide structural information on chromatin scaling and functional information on cell cycle stage associated with various cellular treatments and perturbations.
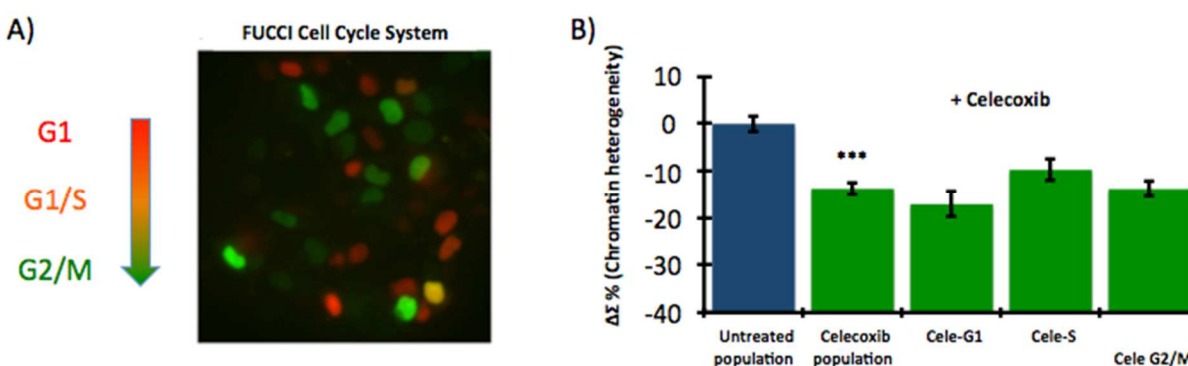
Figure 3.6. *Cell cycle distribution for untreated and 48 hr celecoxib-treated HCT116 cells.* FUCCI Cell Cycle fluorescent indicator system was used to sort cells based on their phase of the cell cycle at a given time. The FUCCI system utilizes both RFP and GFP fused to two different regulators of the cell cycle: cdt1 and geminin. In the G1 and S phases of the cell cycle, geminin is degraded; therefore, only cdt1 tagged with RFP is present. In the G2, and M phases, cdt1 is degraded and only geminin tagged with GFP remains. During the G1/S transition, when cdt1 levels are decreasing and geminin levels increasing, both proteins are present, and when the green and red images are overlaid, nuclei appear yellow fluorescent. A) Representative image of an untreated HCT116 cell population displaying cells in each phase of the cell cycle. B) 48 hr 75uM celecoxib treatment of HCT116 cells decreases population chromatin scaling in relation to control cells but does not lead to cell cycle-dependent changes in chromatin scaling.

3.3.4. Chromatin heritability

The importance of developing tools to study dynamic changes in chromatin scaling and understanding the relationship between chromatin scaling and key cellular process like transcription and cell cycle depends to some extent on whether chromatin scaling is heritable or not. If chromatin scaling "resets" every time a cell divides, the benefit of targeting or trying to understand what leads to changes in chromatin scaling has limited relevance. However, if chromatin scaling is indeed heritable, numerous

implications arise in terms of the role it plays in a vast array of normal cellular functions as well as in disease progression and can even provide insight into ways to target chromatin scaling to combat disease progression.

Having shown that chromatin scaling, as measured by PWS, is not just a marker of cell cycle progression (Figure 3.5 and Figure 3.6), we next set out to determine if chromatin scaling was heritable or not. We plated HCT116 cells at low density and performed cluster analysis of chromatin scaling on cells that divided.   Specifically, we analyzed the average chromatin scaling of small clusters of cells that divided between 12 and 24 hrs and normalized the average of each cluster to the average of all clusters. With this analysis, we observed a correlation indicating 81% of variability between average chromatin scaling of a given cluster could be explained by heritability.
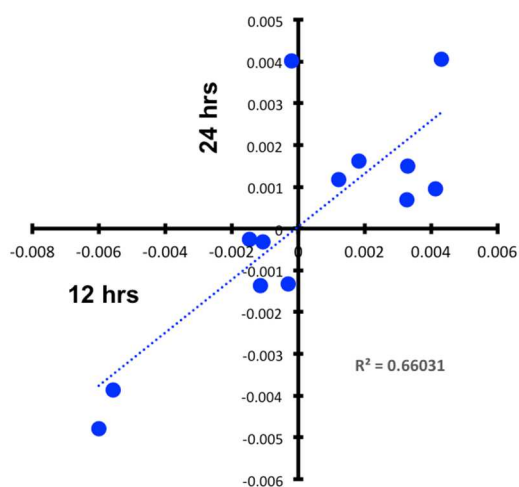
Figure 3.7. *Heritability of chromatin scaling.* Cluster analysis of chromatin scaling in HCT116 cells over cell division indicates chromatin scaling is heritable. Each data point indicates the difference in chromatin scaling of a given cluster compared to chromatin scaling of all clusters at 12 (x axis) hours and at 24 (y axis) hours. The correlation between the data points indicates that 81% of variability can be explained by heritability.

3.3.5. Targets for regulating chromatin scaling: loop formation, histone modifications, and the nuclear environment

Given the established relationship between chromatin scaling and global transcriptional patterns, there are may potential situations where it would be beneficial to regulate chromatin scaling, either to limit

or stimulate adaptive potential depending on a given disease state or extracellular condition. To identify pharmacological compounds that would have a direct impact on chromatin scaling, we considered the model of chromatin as a polymer and identified two principal targets for regulating chromatin polymer packing density scaling: 1) processes that use ATP and molecular motors to create chromatin loops, and 2) the natural conformation of a chromatin chain within the nucleus as influenced both by chromatin self-interactions and chromatin-nucleoplasm interactions.

Using these two approaches, we screened for a variety of compounds that can be expected to regulate chromatin packing density scaling (Figure 3.8). For ATP-dependent processes that create chromatin loops, we examined the effect of partial SA1 inhibition on chromatin scaling. SA1, a component of the cohesion complex is involved in chromatin looping and the formation of TADs. As such, modulation of this protein may serve as a means to regulate chromatin scaling (14). Using a CRISPR SA1 kd cell line, we observed only a very modest (4%) effect of the SA1 kd on Σ (Figure 3.8). However, even the complete suppression of TADs has been shown to only affect the expression of less than 0.5% of all genes and only involves a small fraction of total chromatin (14, 77). Thus, it follows that only modest changes in chromatin scaling can be achieved through altering looping mechanisms.
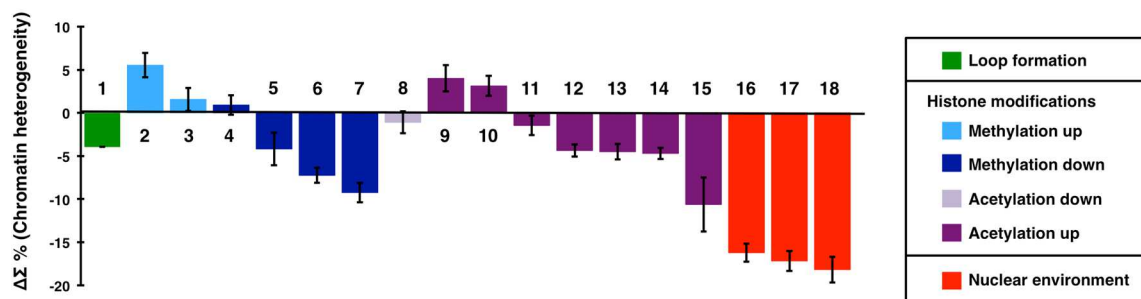
Figure 3.8. *Targets for regulating chromatin packing density heterogeneity.* Change in chromatin packing heterogeneity as influenced by loop formation (1. CRISPR SA1 knock down), histone (2. Compound A12: HMTase, 3. Compound B2: HMTase, 4. UNC0638: DNMT inhibitor, 5. UNC1990: DNMT inhibitor, 6. SGI-110: DNMT inhibitor, 7. GSK126: EZH2 inhibitor, 8. Compound A10: Sirtuin, 9. A4: HDAC inhibitor for HDAC6 and HDAC8, 10. 4-Phenylutyrate: HDAC inhibitor, 11. Ginseng: HDAC inhibitor, 12. Simvastatin: HDAC inhibitor, 13. Resveratrol: HDAC inhibitor, 14. Mevastatin: HDAC inhibitor, and 15. Valproic acid: HDAC inhibitor), and physico-chemical regulation (16. Valinomycin: potassium ionophore, 17. Celecoxib: ion channel inhibitor, and 18. Digoxin: cardiac glycoside). Compounds modulating the nuclear environment (valinomycin, celecoxib, and digoxin) were most efficient at regulating chromatin packing as measured by PWS microscopy. Significance was determined using Student's t-test with unpaired, unequal variance on the average nuclear sigma normalized by the sigma of the accompanying control group between the conditions (***P<0.001). Scale bars, 20uM. Pseudo-color: heterogeneity of chromatin packing density (Σ).

Turning to the natural conformation of a chromatin chain within the nucleus as influenced both by chromatin self-interactions and chromatin-nucleoplasm interactions, we next screened compounds that could be expected to alter either the levels of chromatin self-interactions (enhanced self-interactions are expected to increase chromatin scaling) and/or chromatin-nucleoplasm interactions (enhanced chromatin-nucleoplasm interactions are expected to decrease chromatin scaling). The strength of self-interactions is influenced by the degree of histone acetylation/methylation and DNA methylation, all of which alter interactions between DNA and histones. Testing several such epigenetic regulators at concentrations and treatment times previously shown to be effective at imparting the intended epigenetic changes, we found that enhancing chromatin self-interactions (though processes such as deacetylation and methylation), increased Σ and vice versa (Figure 3.8). However, most of these regulators are specific to particular histones or fractions of the genome and thus cannot be expected to alone impart genome-wide regulation of histone modifications. We accordingly found that even high doses of such acetylation and methylation regulators resulted in only modest changes (<10%) in chromatin scaling.

We finally screened compounds that affect factors impacting the physico-chemical nanoenvironment and chromatin-nucleoplasm interactions, such as intra-domain ionic composition, pH, and crowding. These effects, we hypothesized, would have a more global impact on chromatin scaling by altering chromatin self-interactions and chromatin-nucleoplasm interactions throughout the genome. Here we tested compounds such as valinomycin (potassium ionophore), celecoxib (previously identified to inhibit Na^+, K^+ and Ca^{2+} channels) (81), and digoxin (cardiac glycoside, which suppresses Na^+/K^+-ATPase and thus reduces intracellular [K+] as a side-effect of its activity) (Figure 3.8). These compounds are known to modulate the ion content of the nucleus through inhibition of ion pumps and channels (celecoxib and digoxin) or through facilitating ion transfer across the nuclear membrane (valinomycin). Changes in the ion content of the nucleus, such as increased [K^+], will change the electric field screening potential between chromatin constituents and thus increase the degree of chromatin scaling (82, 83).

3.4. CONCLUSION

The essential role of chromatin packing in shaping and regulating the genomic information space is becoming increasingly apparent with the development of more nuanced models of transcription and the emergence of new imaging techniques such as ChromEMT. We now have evidence that transcriptional regulation occurs at the nucleosomal level and the level of genome compartmentalization, but it also is regulated within the ~kbp – Mbp range, where chromatin packing can affect global patterns of gene expression. Specifically, we have seen that by increasing chromatin packing scaling, D, transcriptional patterns of an increase in relative transcriptional diversity, relative intercellular gene expression heterogeneity, and gene network heterogeneity emerge.

Additionally, we have analyzed the relationship between chromatin scaling and genome connectivity, particularly that contact probability profiles are driven by chromatin packing properties, which affect and are affected by gene-specific compartmentalization mechanisms that delineate TAD boundaries. This understanding, paired with the ability to systematically regulate chromatin scaling through the targeting of loop formation, histone modifications, and the nuclear nanoenvironment, creates a powerful tool with which to both study chromatin scaling properties associated with various cellular processes but also to potentially target chromatin scaling for predictable outcomes. This ability has many potential applications, including within the context of diseases such as carcinogenesis and neurodegenerative disorders. The next chapters will briefly explore the role of chromatin scaling in three different applications: 1) Reducing inflammation within the context of neointimal hyperplasia, 2) Cellular stemness and increasing the adaptive potential of cells, and 3) Understanding the earliest stages of carcinogenesis and the ability of cells to evade chemotherapy.

Chapter 4: The chromatin scaling-mediated vasculoprotective effects of Sirt1

This work done in collaboration with Dr. Michele Jen in Dr. Guillermo Ameer's lab

4.1. INTRODUCTION

One such area in which chromatin scaling and its role in disease response can be examined is that of cardiovascular inflammation. Sirtuin 1 (Sirt1) is an NAD+-dependent lysine deacetylase that regulates multiple critical cellular processes including stress response, senescence, apoptosis, energy metabolism, and DNA repair by deacetylating histones and transcription factors. Sirt1 has been shown to be involved in the protection against oxidative stress and inflammation by deacetylating FOXO transcription factors and the RelA/p65 subunit of NFκB (84-89). In addition, Sirt1 has been reported to exhibit numerous vasculoprotective effects such as enhancement of endothelial nitric oxide synthase activity, inhibition of endothelial cell senescence, and inhibition of thrombosis as well as vascular smooth muscle cell (VSMC) proliferation and migration (25-29, 90-93). Sirt1 inhibition has been shown to reduce DNA repair in VSMCs, increase inflammation in endothelial cells (EC), and promote *in vivo* arterial thrombosis (90, 91). Additionally, targeted overexpression of Sirt1 in VSMC and EC transgenic mice inhibited neointima formation and decreased atherosclerotic lesions respectively (93, 94). However, the role of Sirt1 in vascular adventitial fibroblasts and whether it can be manipulated to inhibit neointimal hyperplasia is not known. We hypothesized that Sirt1 overexpression in AFs would lead to vasculoprotective cellular responses that are mediated in part by modulation of chromatin scaling to prevent inflammatory response.

In addition to its deacetylase activity, Sirt1 can play a critical role in controlling gene expression by modulating the accessibility of genes to transcription factors and polymerases. By studying the differential remodeling of chromatin, the effects of inflammatory and oxidative responses on the local activation or repression of gene expression can be examined.

Herein we use live cell PWS to study the role of Sirt1 as a regulator of chromatin scaling and dynamics to limit gene expression in response to inflammation. Furthermore, through the parallel use of biological assays, we show that Sirt1 transgene delivery to adventitial cells is protective against inflammation, oxidative stress, and cellular senescence, and is a potential strategy to attenuate neointimal

hyperplasia. The integration of these findings suggests that Sirt1's role as a modulator of the physical nanoscale structure of chromatin could be leveraged to prevent restenosis due to neointimal hyperplasia following vascular injury.

4.2. MATERIALS AND METHODS

4.2.1. Cloning of Sirt1 into lentiviral transfer plasmid

The plasmid coding sequence for Sirt1 (plasmid #1791) was obtained from Addgene (Cambridge, MA). Sirt1 forward and reverse primers were designed with PmeI digestion sequence both upstream and downstream of the Sirt1 coding region.

Sirt1-F-PmeI	ATA GTT TAA ACA TGG CGG ACG AGG CGG CCCT
Sirt1-R-PmeI	CGC GGT TTA AAC CTA TGA TTT GTT TGA TGG ATA GTT C

Sirt1 coding region was PCR amplified using Phusion® DNA polymerase (NEB, Ipswich, MA) under the conditions of GC-rich templates. The Sirt1 PCR product was separated from the template using electrophoresis in a 1% agarose gel, isolated using a gel extraction kit (Qiagen, Valencia, CA), and subsequently digested using PmeI (NEB, Ipswich, MA) and purified using PCR purification kit (Qiagen, Valencia, CA).

The lentiviral transfer vector, pWPI (plasmid #12254, Addgene, Cambridge, MA), was digested with PmeI and dephosphorylated with calf-intestinal alkaline phosphatase (NEB, Ipswich, MA). The PmeI-digested Sirt1 PCR product was ligated with the PmeI-digested/dephosphorylated pWPI using T4 DNA ligase (NEB, Ipswich, MA) at various product to vector ratio (e.g., 2:1, 5:1, and 10:1) at room temperature for 2 h. The ligation mixtures were transformed into One Shot® Stbl3™ Chemically Competent E. Coli (Life Technologies, Carlsbad, CA) and plated on LB-agar+antibiotics plates. Colonies were picked and plasmids were isolated using QIAprep Spin Miniprep Kit (Qiagen, Valencia, CA). Clones were confirmed using restriction enzyme digestion for proper orientation and insertion of Sirt1 coding sequence. Clones were also submitted for DNA sequencing using the following sequencing primers:

EF1alpha forward	TCAAGCCTCAGACAGTGGTTC

Sirt1_1 forward	AGGCGGCGGCGGCGGCGATT
Sirt1_2 forward	AACAGCATCTTGCCTGATTT
IRES reverse	CCTCACATTGCCAAAAGACG

Production of lentivirus for Sirt1

Lentiviral packaging vectors, pMD2.g and psPAX2 (plasmid #12259 and #12260, Addgene, Cambridge, MA), were co-transfected with pWPI, pWPI-Sirt1, or pWPI-Sirt1 (H363Y) mutant (plasmid #1792, Addgene, Cambridge, MA) (mass ratio 1:3:4, respectively) into HEK-293FT cells using Fugene HD (Promega, Madison, WI) at 3:1 Fugene HD volume to total DNA mass ratio complexed in Opti-MEM (Life Technologies, Carlsbad, CA). After 48 h of transfection, the supernatant was collected and purified using Lenti-X Maxi Purification Kit (ClonTech, Mountain View, CA) and subsequently concentrated using Lenti-X concentrator (ClonTech, Mountain View, CA).

4.2.2. AoAF transduction and immunofluorescence/immunoblot studies

Human aortic adventitial fibroblasts (AoAFs) (Lonza, Walkersville, MD) were transduced with lentiviruses. Empty vector and LV-Sirt1 constructs contain IRES-EGFP sequence that allow for co-expression of EGFP. To obtain a homogeneous population of cells that were transduced, AoAFs were sorted (BD FACSAria II, Franklin Lakes, NJ) for EGFP positive expression from the empty vector and LV-Sirt1 transduced groups. Non-transduced cells were also analyzed through the sorter but were not sorted for EGFP expression. For immunobloting, cellular proteins were extracted using RIPA buffer and fractioned using Bolt® 4-12% Bis-Tris gel (Life Technologies, Carlsbad, CA), electro-transferred onto a nitrocellulose membrane, and probed using anti-Sirt1 (sc-74504, Santa Cruz Biotechnology, Dallas, TX; 9475, Cell Signaling, Danvers, MA) and anti-β actin antibodies (4970, Cell Signaling, Danvers, MA). For immunofluorescence, AoAFs were fixed with cold methanol and incubated with anti-Sirt1 antibody (sc-74504, Santa Cruz Biotechnology, Dallas, TX). Fixed cells were mounted with VectaShield plus DAPI (Burlingame, CA).

4.2.3. Cell lysis and measurement of deacetylase activity

AoAFs were lysed using CelLytic^{TM} M (Sigma, St Louis, MO). Cells were scraped and lysates were collected, passed through a 21 gauge needle, and centrifuged at 12,000 rpm for 10 mins at 4°C to pellet cell debris. Supernatants at approximately 1 mg/mL were collected and frozen at -80°C. To measure deactylase activity, supernatants were incubated at 37°C for 30 mins, 1 hr, or 2 hr with NAD$^+$, TSA, and Ac-GRK^{Ac}HYC-NH$_2$ peptides at a final concentration of 1 mM, 50 μM, and 17.4 μM, respectively with protease inhibitor cocktail (Roche, South San Francisco, CA).(95) The reaction mixtures were then quenched with 50 mM nicotinamide and transferred to a 384-gold spotted array plate with maleimide-terminated self-assembled monolayers for peptide immobilization. The plates were subsequently washed with deionized water and ethanol, dried using nitrogen, and treated with matrix (2,4,6-trihydroxyacetophenone, 20 mg/mL in acetone) and analyzed using MALDI-TOF MS. Activities were calculated from each spectrum based on the percentage conversion as previously described.(96)

4.2.4. Measurement of NFκB and p53 activity using transcription factor-lentiviral reporters

Transcription factor (TF) lentiviral reporter consisted of a TF response element (NFκB and p53) cloned upstream of a TA promoter driving the firefly luciferase gene (constructs produced by Prof Lonnie Shea's lab). TF binding to the TF response element results in luciferase production, and relative measure of TF activity can be quantified by measuring the luminescence produced in the presence of excess D-luciferin (Caliper Life Sciences, Hopkinton, MA). AoAFs were first transduced with lentiviral reporters, and after 3 days, were seeded in clear-bottom, black 96-well plates (Greiner Bio-One, Monroe, NC). Cells were either not stimulated or stimulated with 20 ng/mL TNFα (Millipore, Billerica, MA) or 1 μM doxorubicin (LC Laboratories, Woburn, MA), treated with 1 mM D-luciferin, and imaged using IVIS Spectrum imaging system (Caliper Life Sciences, Hopkinton, MA).

4.2.5. Quantification of inflammatory and antioxidant gene expression

AoAFs were stimulated either with or without 20 ng/mL TNFα (Millipore, Billerica, MA) or 10 μM of Menadione (MP Biomedicals, Santa Ana, CA) for 6 hr. Total RNA was extracted using TRIzol (Life

Technologies, Carlsbad, CA) reagent as described by the manufacturer and cDNA was synthesized using qScript cDNA supermix (Quanta Bioscience, Gaithersburg, MD). Quantitative RT-PCR was used to measure mRNA levels of GAPDH, IL-1β, MCP-1, catalase, manganese superoxide dismutase (SOD2) using Power Sybr Green PCR master mix (Life Technologies, Carlsbad, CA) and Bio-Rad CFX96 (Hercules, CA)

GAPDH	AGTCCTTCCACGATACCAAAGT
GAPDH	CATGAGAAGTATGACAACAGCCT
IL-1β forward	TACCTGTCCTGCGTGTTGAA
IL-1β reverse	TCTTTGGGTAATTTTTGGGATCT
MCP-1 forward	CATTGTGGCCAAGGAGATCTG
MCP-1 reverse	CTTCGGAGTTTGGGTTTGCTT
Catalase forward	TGAGGTCCACCCTGACTACG
Catalase reverse	GAGATCCGGACTGCACAAAG
SOD2 forward	ACAGGCCTTATTCCACTGCT
SOD2 reverse	CAGCATAACGATCGTGGTTT

IL-1β and MCP-1 protein quantification

AoAFs were stimulated either with or without 20 ng/mL TNFα (Millipore, Billerica, MA) for 24 hr and cell culture supernatants were collected, spun down at 1500 rpm for 5 mins to pellet residual cells, and cell-free supernatants were frozen. Supernatents were assayed for IL-1β and MCP-1 using V-PLEX™ Human Cytokine and Chemokine kits (Meso Scale Discovery, Gaithersburg, MD) and measured using MESO QuickPlex SQ 120 (Meso Scale Discovery, Gaithersburg, MD).

4.2.6. Cell line characterization assays

Assessment of cytotoxicity

AoAFs, plated in clear bottom, black 96-well plates, were incubated with CellTox™ Green Dye, AoAF cell culture media, and 0.5 μM of doxorubicin. Relative fluorescent units (RLU) were measured at various time points using a fluorescent plate reader (Molecular Dynamics M3, Sunnyvale, CA) according to the

manufacturer of the CellTox™ Green Cytotoxicity Assay (Promega, Madison, WI) and were normalized to the RFU at the initial time point.

Assessment of senescence associated β-galactosidase

AoAFs were allowed to age to passage 12. Cells were fixed and stained with x-gal using a cellular senescence assay kit (Millipore, Billerica, MA) following manufacturer's protocol. The number of β-galactosidase positive cells were quantified from images taken at various locations in multiple wells.

Quantification of cell proliferation

AoAFs were aged to passages greater than 10 and plated in 96-well plates at a density of 5,000 cells/cm^2. At different time points, cells were lysed with 0.1% Triton X-100/Tris-EDTA buffer and lysates were stored at -20°C in a black 96-well plate. To quantify cell number, a standard curve using known quantity of cells was generated and Quanti-iT Picogreen assay (Life Technologies, Carlsbad, CA) was performed following manufacturer's recommendation.

Analysis of cell cycle

AoAFs were cultured in minimal serum (0.2% serum) for 48 hr. Cells were then cultured in complete-serum cell culture medium for 24 hrs and fixed with ice-cold 70% ethanol overnight. The fixed cells were washed with PBS twice by pelleting cells via centrifugation. Cell pellet was resuspended and incubated in stain solution (50 μg/mL propidium iodide, 180 units/mL RNase, 0.1% Triton X-100, 4 mM citrate buffer, and 30 μg/mL polyethylene glycol 6000) at 37°C for 20 mins. Finally, an equal volume of salt solution (50 ug/mL propidium iodide, 0.1% Triton X-100, 0.4 M NaCl/H_2O, and 30 μg/mL polyethylene glycol 6000) was added and immediately measured using a flow cytometer (BD LSRII, Franklin Lakes, NJ).

Measurement of superoxide production

AoAFs were plated in clear bottom, black 96-well plates, at a density of 20,000 cells/cm^2 and stimulated with antimycin A (Enzo Life Sciences, Farmingdale, NY) for 30 mins. Dihydroethidium bromide

(PolySciences, Warrington, PA) was added to each well to a final concentration of 5 µM, and the fluorescence intensity was measured using a plate reader (Molecular Dynamics M3, Sunnyvale, CA) at various times and normalized to initial fluorescence.

Statistical analysis

Statistical analysis was conducted using GraphPad Prism software (La Jolla, CA). Statistical significance between groups was by two-way ANOVA followed by Bonferroni posttest for multiple comparisons and one-way ANOVA, when appropriate. A level of $p < 0.05$ was accepted as significant.

4.2.7. MNase accessibility assays

MNase assays were performed by culturing the cells on 6-well plates to 80% confluence. Cell membranes were permeabilized with an NP-40 lysis buffer and exposed to MNase (Sigma) buffer in the presence of $CaCl_2$ for experimentally determined amounts of time. After digestion, the DNA was extracted with a 1:1 phenol:chloroform mixture and an ethanol precipitation followed, using standard procedures. Samples were run on a 1.2% agarose gel: 2.5 µg of DNA for the undigested control samples and 10 µg of DNA for the time point digested samples. The gel was stained with ethidium bromide for detection of nucleosomal bands.

4.3. RESULTS

4.3.1. Sirt1 overexpressing AoAF cells exhibit increased lysine deacetylase activity and decreased NFkB activation and targeted gene expression

A Sirt1 Aortic Adventital Fibroblast (AoAF) model was created through lentiviral transfection. Sirt1 or a Sirt1 dominant negative mutant (H363Y) was cloned into a lentiviral transfer plasmid and lentiviral vectors encoding for Sirt1 (LV- Sirt1) or Sirt1 mutant (LV- Sirt1 mutant) were produced. Primary human AoAFs were incubated either with LV- Sirt1, LV- Sirt1 mutant, or empty vector (lentiviral vector without the Sirt1 gene) and, after three days of transduction, immunostained or lysed and immunoblotted for Sirt1. The immunofluorescence stain and immunoblot demonstrate overexpression of Sirt1 for cells

transduced with LV- Sirt1 or LV- Sirt1 dominant negative mutant (Appendix B1). According to the immunofluorescence stain, Sirt1 overexpression is predominantly localized in the nucleus, which is consistent with previous reports (96).

Self-assembled monolayer desorption ionization (SAMDI) was used to assess enzyme deacetylase activity. Whole-cell lysates were incubated with an acetylated-lysine peptide, GRK^{Ac}HYC, that was previously shown to have high SIRT specificity (95). Peptides were then immobilized onto maleimide-terminated self-assembled monolayers on a 384-gold spotted array plate and analyzed for the ratio of deacetylated to acetylated variants of the peptide using mass spectrometry. Sirt1-overexpressing AoAFs have significantly higher lysine deacetylase activity with increasing incubation time suggesting greater enzymatic activity (Figure 4.1A) (95, 96). Conversely, non-, empty vector, and Sirt1-mutant transduced AoAFs have modest increase in deacetylase activity over time (Figure 4.1A). SIRT2 and SIRT3 protein concentrations remained unchanged upon transduction, attributing the lysine deacetylase activity to Sirt1.

Additionally, NFκB-reporter lentiviral constructs were used to transduce homogeneous populations of empty vector and LV- Sirt1 transduced cells. When stimulated with TNFα, Sirt1-overexpressing AoAFs have significantly lower NFκB activation compared to non-transduced and empty vector transduced cells (Figure 4.1B). Upon TNFα stimulation, the NFκB target genes, such as interleukin-1β (IL-1β) and monocyte chemoattractant protein-1 (MCP-1), were also significantly decreased in Sirt1-overexpressing AoAF compared to non-transduced and empty vector transduced AoAF cells (Figure 4.1C).
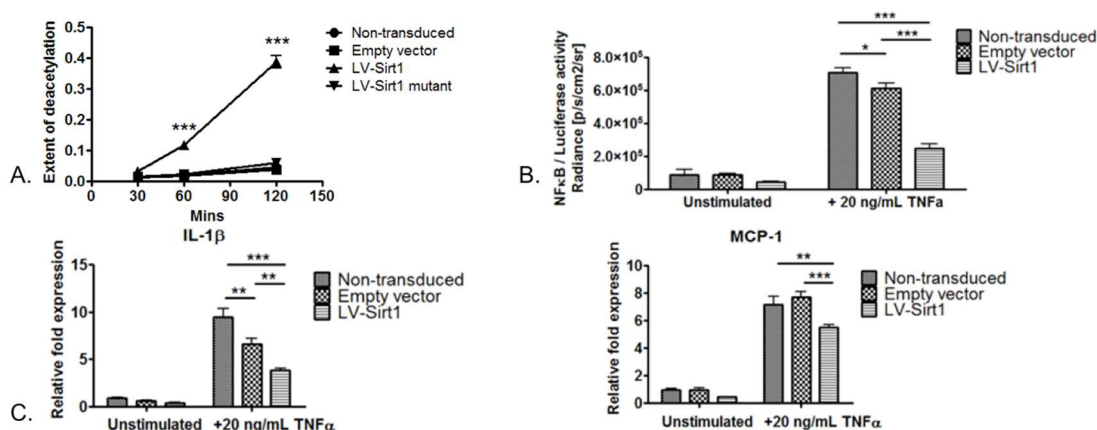
Figure 4.1. *Sirt1 leads to increased lysine deacetylase activity and decreased NFkB activation.* A Sirt1-overexpressing AoAF model was created through lentiviral transfection. The Sirt1-overexpressing line has significantly higher deacetylase activity over time (A). Additionally, TNFα stimulation revealed the Sirt1 cells have significantly lower NFkB activation (B) and decreased expression of NFkB target genes interleukin-1β (IL-1β) and monocyte chemoattractant protein-1 (MCP-1) (C). Cell line characterization and analysis was performed by Michele Jen, Ameer Lab, Northwestern University.

4.3.2. Sirt1 overexpression prevents cellular senescence and transduces the adventitia of rat carotid arteries

p53-luciferase reporter constructs were used to investigate the effect of Sirt1 overexpression on p53 activation by doxorubicin. Treatment with doxorubicin increased p53 activity and cytotoxicity, but this increase was attenuated in Sirt1-overexpressing AoAFs by approximately 66% (Figure 4.2A). In the absence of doxorubicin stimulation, Sirt1 also significantly attenuated p53 activation. Several studies suggest that Sirt1, by deacetylating p53, can prevent cellular senescence (97, 98). Cellular senescence has been linked to several cardiovascular disorders such as atherosclerosis and arterial calcification (98, 99). To study senescence, we allowed the cells to age until the replication rate of non-transduced cells slowed significantly (> passage 10) and stained them for β-galactosidase, a widely-used marker for cellular senescence (98-102). We observed that the Sirt1-overexpressing AoAFs had 60% fewer cells positive for β-galactosidase than control groups (Figure 4.2B). Further, we consistently found that the Sirt1-overexpressing AoAFs maintained a typical advential morphology and continued to proliferate in culture for passages > 10. On the other hand, non- and empty vector- transduced AoAFs failed to create a confluent culture and displayed a significant transformation of cellular morphology at higher passages.

To address whether LV- Sirt1 can transduce adventitial cells *in vivo*, we perivascularly applied LV- Sirt1 around the left carotid arteries of rats. After 8 days of transduction, Sirt1-overexpessing cells were predominantly observed in the adventitia of carotid arteries treated with lentiviruses encoding for Sirt1 (LV- Sirt1) (Appendix B2). While Sirt1 is ubiquitously expressed in all cell types, in aortic tissue samples, Sirt1 expression is the highest in the medial layer where the smooth muscle cells reside.
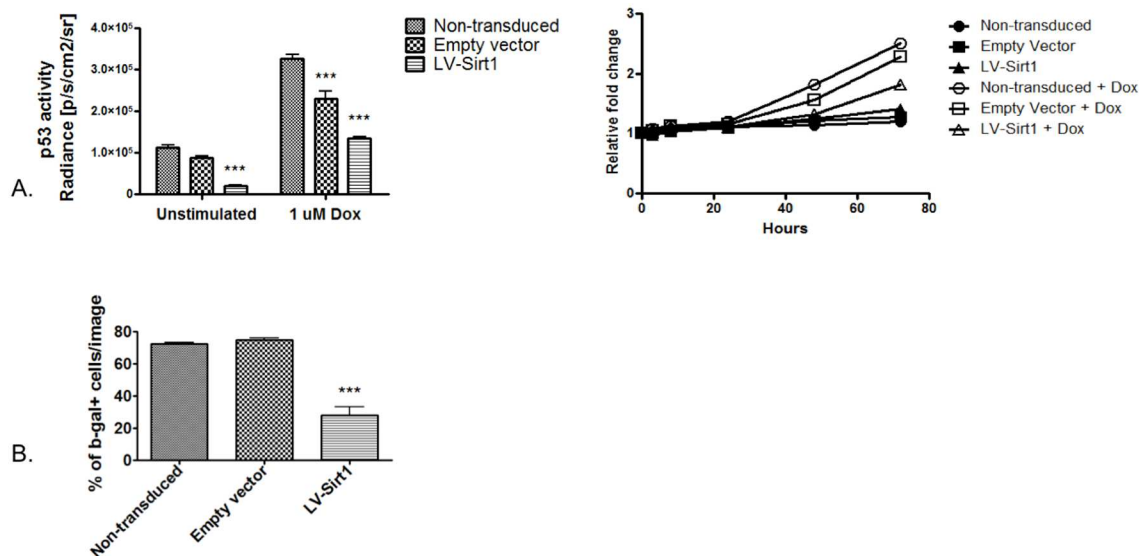
Figure 4.2. *Sirt1 prevents cellular senescence.* Doxorubicin treatment increased p53 activity in AoAF cells, but the effect was attenuated in Sirt1 overexpressing cells by 66% (A). β-galactosidase was then used as a marker for cellular senescence, and we observed 60% fewer β-galactosidase positive cells for the Sirt1 overexpressing cells compared to the control cells (B). Cell line characterization and analysis was performed by Michele Jen, Ameer Lab, Northwestern University.

4.3.3. Sirt1 overexpression results in decreased global chromatin accessibility and decreased transcriptional activity

To study the nuclear structural effects of Sirt1 overexpression, we used micrococcol nuclease (MNase) accessibility assays (48). Control and Sirt1-overexpressing AoAF cells were treated with MNase for increasing amounts of time (Figure 4.3). In the absence of MNase (time 0), the AoAF cell lines did not exhibit any endogenous nuclease activity.   The Sirt1 overexpressing AoAF cells exhibited greater resistance to MNase at later time points as opposed to the control cells, indicating a state of less globally

accessible chromatin. The difference in MNase accessibility between cell lines was most apparent at earlier time points.
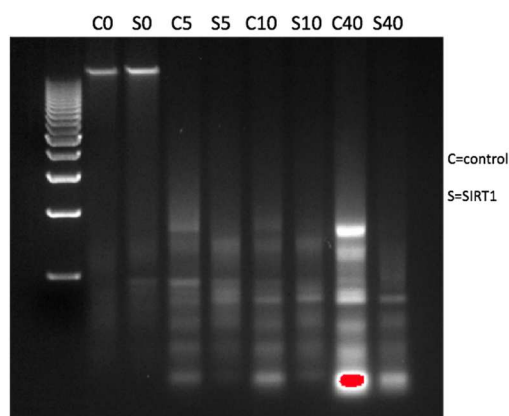
Figure 4.3. *Sirt1 overexpression decreases global chromatin accessibility in AoAF cells.* Micrococcal Nuclease (MNase) digestion assay of control and Sirt1-overexpressing AoAF cells indicates more accessible chromatin in the control cells compared to Sirt1-overexpressing AoAF cells. The control cells respond to the MNase at earlier time points, exhibiting brighter mononucleosomal bands in comparison with the Sirt1 cells. This suggests the chromatin in the control cells is more accessible to the MNase and thus, more easily digested.

As a class III HDAC, Sirt1 deacetylates histones H4K16, H3K9 and H3K14, and H1K26 (103), modifications that are directly linked to gene silencing. Sirt1 can also deacetylate other, non-histone substrates such as NFkB, thus inhibiting the activation of the inflammatory response. Sirt1 activity, then, correlates with decreased transcriptional activity. Consequently, we strove to link the structural changes between the control and Sirt1 overexpressing AoAF cell lines to functional changes in transcriptional activity.

We performed structured illumination microscopy (SIM) to image immuno-fluorescently-labeled histone methylation marks H3K9me3 (for transcriptional repression) and H3K4me2 (for transcriptional activation). We found the Sirt1-overexpressing cells had a greater amount of transcriptionally repressed chromatin (Figure 4.4), suggesting the decrease in global chromatin accessibility caused by Sirt1 lead to decreased levels of transcriptional activity.

A)

B)

Control   Sirt1 overexpressing
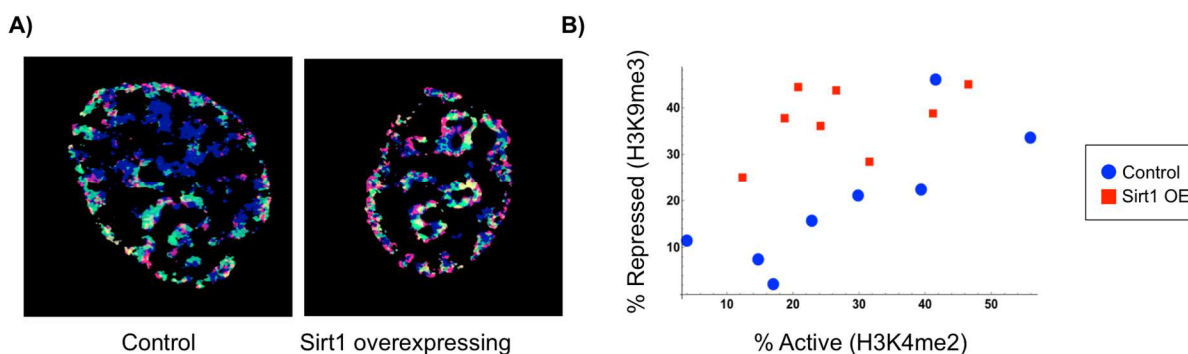
Figure 4.4. *SIRT1 overexpression in AoAF cells results in overall decrease in transcriptional activity.* A) Structured Illumination Microscopy (SIM) shows differential levels of transcriptionally active and repressed chromatin between control and Sirt1 overexpressing AoAF cells. Red corresponds to H3K9me3 (transcriptionally repressed chromatin), green corresponds to H3K4me2 (transcriptionally active), and blue corresponds to TOPRO3 nuclear stain. B) The Sirt1 overexpressing cells have more transcriptionally repressed chromatin. % Active and repressed chromatin was calculated relative to area of nucleus positive for TOPRO3 nuclear stain. Each data point in the plot represents one cell.

Combined, these data suggest Sirt1 structural effects have direct transcriptional consequences: Global reduction in chromatin accessibility as a result of Sirt1 overexpression leads decreased transcriptional activity.

4.3.4. Dynamic monitoring of chromatin scaling shows differential response to TNFα stimulation as a result of Sirt1 overexpression

While static differences in nuclear structure and transcriptional activity are important in understanding the end effects of molecular states such as Sirt1 overexpression, they fail to provide information on how those molecular states respond to dynamic processes such as the onset of inflammation. In order to fully understand the dynamic process of chromatin remodeling and its transcriptional effects within the context of inflammation, it is essential to study these processes in live cells in real time. Understanding the role of Sirt1 in transcriptional stimulation can guide the understanding of how it modulates a cell's response to inflammation.

We have shown remarkable and immediate (within minutes) differences in real time chromatin remodeling in response to stimulation with TNFα as a result of Sirt1 overexpression. TNFα is a key regulator of the inflammatory response cascade and activates the heterodimeric transcription factor NF-κB. NF-κB translocates to the nucleus and is involved in the transcription of a vast array of proteins involved in the inflammatory response. Thus, TNFα induces transcription through the activation of NF-κB

as a function of time and can be used to study chromatin remodeling in control and Sirt1-overexpressing AoAF cells.

Using qRT-PCR, we quantified mRNA expression of NFkB in control AoAF cells and showed differences in the mRNA expression of NFκB following induction with the cytokine TNFα (Figure 4.5).
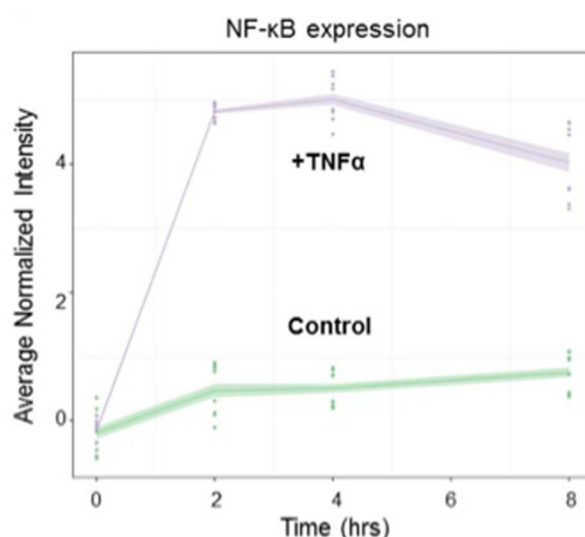
Figure 4.5. *mRNA expression of NFkB after TNFα stimulation.* qRT-PCR experiments were performed to measure transcripts after stimulation of AoAF cells with TNFα. NFκB activation occurs within the first two hours after stimulation and then levels off. Shaded region depicts the 95% confidence area. NFκB experiments were performed by Michele Jen, Ameer Lab, Northwestern University.

Using live cell PWS, we observed TNFα-induced differential dynamic changes in chromatin scaling within 30 minutes between the control and Sirt1-overexpressing cell lines (Figure 4.6). In control AoAF cells, chromatin scaling increased globally over time in response to TNFα. However, in Sirt1 cells, the chromatin scaling remained relatively constant over the same time period. Thus, the control cells undergo a significant increase in global chromatin scaling as a part of the NFkB inflammatory response, while Sirt1 appears to protect against inflammation response by limiting the chromatin scaling response.
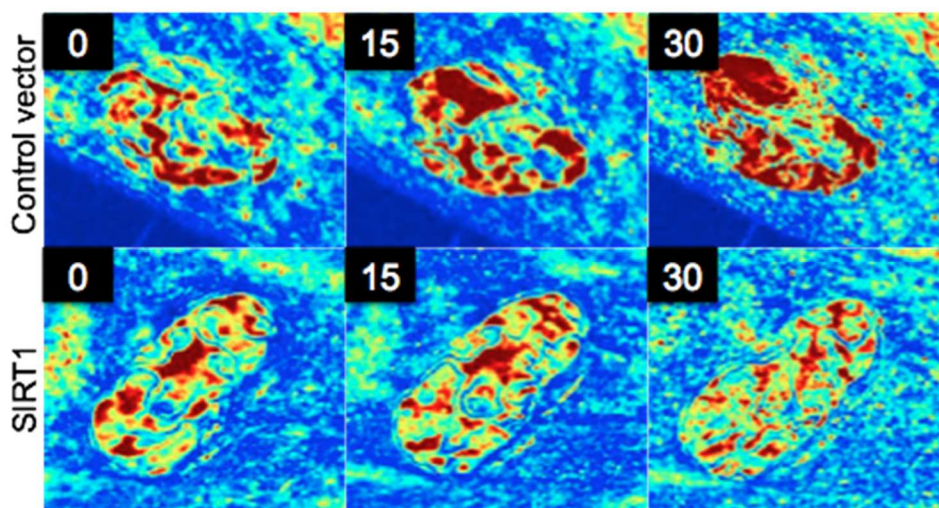
Figure 4.6. *Differential chromatin scaling response of control and Sirt1 AoAF cells to transcriptional activation by TNFα.* Images are taken before, 15, and 30 min. post TNFα treatment of control (top) and Sirt1-overexpressing (bottom) AoAF nuclei. Increase in red correlates with a higher level of chromatin remodeling and subsequent changes in gene transcription. Trends were consistent across three biological replicates.

We also performed qRT-PCR on two genes of interest, both NFkB target genes involved in the inflammatory response cascade: IL-1B and MCP-1. IL-1β is a member of the interleukin 1 family of cytokines, is an important mediator of the inflammatory response, and is involved in a variety of cellular activities, including cell proliferation, differentiation, and apoptosis. MCP-1 is a small cytokine that recruits monocytes, memory T cells, and dendritic cells to the sites of inflammation produced by either tissue injury or infection. GAPDH was used for normalization expression levels of the genes of interest. We hypothesized that if Sirt1 is protective against inflammation (as it deacetylates a key residue on NFkB that is essential for its activation), then we would not expect to see a change in expression of IL-1B and MCP-1 between control and TNFα treated cells for the Sirt1 OE cell line. Conversely, we expected to see an increase in IL-1B and MCP-1 expression in the CV line upon TNFα stimulation. Our experiments showed a 10-fold and 3-fold increase in expression of IL-1B and MCP-1 respectively for the control cells upon TNFα stimulation and a 0.3-fold and .26-fold decrease for IL-1B and MCP-1 respectively for the Sirt1 overexpressing cells upon TNFα stimulation. These data give transcriptional evidence to the model that nuclear nanostructural rearrangements associated with TNFα stimulation on Sirt1 overexpression lead to transcriptional repression.

Taken together, these data suggest a reason for Sirt1-overexpression resulting in a diminished response to TNFα stimulation. By deacetylating NFkB, Sirt1 inhibits the activation of the inflammatory response. We see with live cell PWS that Sirt1 minimizes the global increase in chromatin scaling seen in control cells upon TNFα stimulation, preventing the activation of the inflammatory response cascade and associated transcriptional activation.

4.4. DISCUSSION

Neointimal hyperplasia is a major challenge to the recovery process following vascular procedures. Mechanisms explaining the resulting inflammation and oxidative stress caused by neointimal hyperplasia point to the adventitia as a key player in neointima formation, however, the mechanisms are still poorly understood. Through our study, we sought to target the adventitia, as opposed to endovascular approaches, to reduce neointimal hyperplasia. Specifically, we used a Sirt1 overexpressing aortic adventital fibroblast (AoAF) model to study the role of nanoscale chromatin structure in the regulation of gene expression at the site of inflammation.

We first designed a Sirt1 overexpressing AoAF cell line and found it to exhibit increased lysine deacetylase activity and decreased NFkB activation and target gene expression. These findings are in line with the known role of Sirt1 to act as a histone deacetylase, which, as one of its targets, inhibits NFkB activation. NFkB target genes IL-1β and MCP-1 were found to have significantly decreased fold expression in Sirt1 overexpressing cells upon TNFα stimulation.

Furthermore, we found that Sirt1 overexpression prevents cellular senescence and transduces the adventitia of rat carotid arteries. When stimulated with doxorubicin, we observed increased p53 activity, which was attenuated by 66% in the Sirt1 overexpressing cells. This suggested that Sirt1 prevents cellular senescence, which has been linked to p53 activation. Indeed, we found that Sirt1 overexpressing cells allowed to age to senescence had 60% fewer cells positive for β-galactosidase than controls. Cellular senescence has been linked to several cardiovascular disorders such as atherosclerosis and arterial calcification, so the ability of Sirt1 to slow the process of senescence proves very promising for the treatment of such diseases.

Upon characterization of our cell culture model, we utilized Micrococcal Nuclease (MNase) digestions to study the effects of Sirt1 overexpression on global chromatin accessibility. Chromatin in the control cells was more accessible to the MNase and thus more easily digested at earlier time points, indicating Sirt1 deacetylase activity results in globally less accessible chromatin.

Structured illumination microscopy (SIM) on fixed AoAF cells allowed us to characterize transcriptional activity in the Sirt1 overexpressing cells. The Sirt1 cells displayed more transcriptionally repressed chromatin compared to control cells indicating a structure/function relationship between Sirt1-induced chromatin accessibility and transcriptional activity.

Most illustrative of Sirt1 function though was the live cell dynamic monitoring of Sirt1 chromatin scaling in response to stimulation with TNFα. We observed differential chromatin scaling responses of control and Sirt1 AoAF cells in response to transcriptional activation, as measured by live cell PWS. In control AoAF cells, chromatin scaling increased globally in response to TNFα, indicating high levels of chromatin remodeling and an increase in gene transcription. However, in Sirt1 cells, chromatin scaling remained relatively constant upon TNFα stimulation. Comparatively, TNFα stimulation induces differential changes in chromatin remodeling within 30 min between the cell lines. Again, NFkB downstream genes IL1-B and MCP-1 expression increased in control cells upon TNFα stimulation but did not significantly change in Sirt1 overexpressing cells. Together, the live cell data and key gene expression analysis suggests that Sirt1 acts to protect against inflammation by limiting changes in chromatin scaling and decreasing genome accessibility, thus preventing the activation of the NFkB pathway and minimizing the effects of inflammation.

The study of the effects of Sirt1 on chromatin scaling and transcriptional activity offer new insights into the dynamics of chromatin remodeling that are key in its role to protect against inflammation. Most current Sirt1 research focuses on biochemical explanations of gene expression, without addressing the structural contributions. Our studies have the unique advantage of utilizing new technology to study these structural interactions catalyzed by sirtuins and how they regulate biological activity. Better understanding of these nuclear dynamics would have implications in the scientific community far beyond gene transcription: a fundamental understanding of what contributes to the regulation of nuclear

reorganization and transcription have applications in any condition/disease in which inflammation plays a

role.

Chapter 5: Chromatin scaling in stem cells

This work done in collaboration with Vasundhara Agrawal from the Backman lab and with Bin Jiang and Xinlong Wang from Dr. Guillermo Ameer's Lab

5.1. INTRODUCTION

A hallmark of life is the capacity to adapt and acclimate to new environmental conditions. These capacities are defined by the timescales of the required response to stressors and growth cues. For instance, mutational adaptation typically requires cells to survive through a replication cycle before the advantage can be conferred. As replication can take on the order of days in eukaryotic cells, mutational adaption would have a minimal benefit in the face of stressors such as ischemia that occur on the hour timescale. At these time scales, the ability of cells to acclimate by sampling the information in their existing repertoire of genes would be helpful for such a response. Similarly, in order for cells and tissues to regenerate they must be capable of re-acquiring or developing new phenotypes to overcome stressors such as ischemia and the scarring process. The ability of cells to dynamically change their gene expression patterns may allow cells to acclimate and survive (promoting cellular fitness) when exposed to stresses at the expense of homeostasis. Conversely, the lack of ability to explore their genomic landscape may shift the balance towards homeostasis at the expense of the cells' fitness.

As most genomic information in eukaryotes is encoded and accessed within the cell nucleus, the capacity to generate these new functions depends on the barriers to the regulators of gene expression. Our data suggest that supranucleosomal chromatin scaling is critically involved in the regulation of the potential of cells to explore their transcriptional landscape. We also have evidence suggesting that these structures can be influenced and potentially controlled via pharmacological agents and morphological surface features that induce nuclear constraints. These controlling factors may act on chromatin nano-architecture leading to better exploration of genomic landscape. While the majority of studies have focused on molecular modifications that govern the transcription of individual gene networks, we have evidence that chromatin nano-architecture plays a regulatory role in governing global patterns of gene expression (Chapter 2) (15, 17). Thus, the capacity to modulate chromatin structure could potentially allow unprecedented control over gene transcription and cell re-programing, leading to new paradigms for

tissue regeneration. Through the use of PWS microscopy, we can identify strategies, both pharmacological and morphological, that regulate supranucleosomal chromatin scaling structure to enhance the adaptive potential of eukaryotic cells and help induce cellular stemness.

5.2. RESULTS AND DISCUSSION

5.2.1. Chromatin scaling in stem and differentiated cells

Whether totipotent or pluripotent, stem cells are characterized by their ability to differentiate into other cell types. Throughout differentiation, a stem cell's chromatin structure undergoes a whole host of physical and chemical changes that result in a completely new phenotype and function. In order to characterize the differences in chromatin scaling between stem and differentiated cells, we investigated several types of stem cells with PWS microscopy: OvCar5 ovarian cancer stem and non-stem cells, human mesenchymal stem cells and differentiated osteoblasts, induced pluripotent stem cells and differentiated endothelial cells, and patient-derived ovarian cancer stem and non-stem cells. Upon analysis with PWS microscopy, we found a universal pattern of higher chromatin scaling in the stem cells compared to their differentiated counterparts (Figure 5.1).
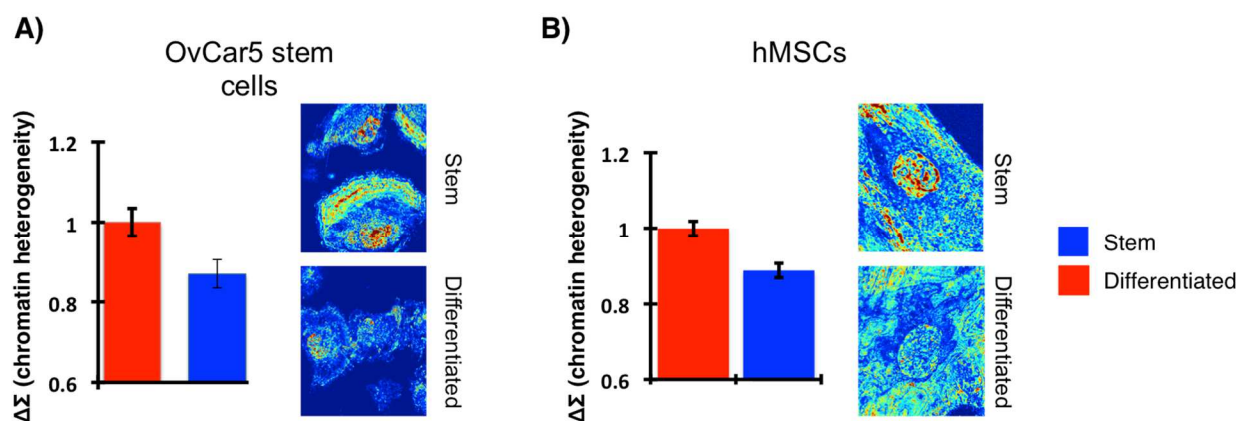
Figure 5.1. *Stem cells exhibit increased chromatin heterogeneity compared to their differentiated counterparts.* A) OvCar5 ovarian cancer stem cells (as categorized by the presence of ALDH) have on average 17% higher chromatin heterogeneity compared to their non-stem (ALDH-) counterparts. B) Human mesenchymal stem cells (hMSCs) have on average 12% higher chromatin heterogeneity compared to differentiated osteoblasts. Significance was determined using Student's t-test with unpaired, unequal variance on the average nuclear Σ normalized by the Σ of the accompanying control group between the conditions. Error bars are standard error for *N*=83 OvCar5 ALDH(+), 75 OvCar5 ALDH(-), 96 human mesenchymal stem, and 84 differentiatied ostoblast cells (***P<0.001).

The presence of distinct chromatin scaling "fingerprints" in paired stem and differentiation models suggest chromatin scaling may be a potential target to enhance the adaptive potential of these cells. Altering global chromatin scaling through pharmacological agents and/or morphological substrate may be effective in facilitating faster movement of cells along the stem cell continuum depending on the desired application.

5.2.2. Effect of pharmacological compounds on chromatin scaling and stem cell differentiation

Previous work (Chapter 3) has shown that there are multiple ways to pharmacologically target chromatin scaling based on the model of chromatin polymer. Given the relationship between chromatin scaling and global patterns of gene expression, there are likely different desirable targets in terms of changing chromatin scaling based on the intended application. In stem cells, targeting chromatin scaling has the potential to enhance cellular plasticity to either increase stem cell differentiation potential or respond appropriately to external stresses.

First, we aimed to determine the effect of various pharmacological compounds on chromatin scaling in stem cells. We utilized a human mesenchymal stem cell (hMSC) model cultured in Dulbecco's Modified Eagle Medium (DMEM), with 4.5 g/L glucose, and supplemented with 10% FBS and 1% penicillin-streptomycin. On day 4, these undifferentiated hMSCs were treated with non-cytotoxic concentrations of (i) HDAC inhibitors - Valproic Acid (100 μM) and 4-Phenyl butyrate (1 mM), (ii) lysosomal Cysteine Protease - Beta Cathepsin (0.1 μg/mL), and (iii) natural phenols - Resveratrol (50 μM) and Curcumin (2.5 μM). Resveratrol, Curcumin, B-cathepsin, 4-Phenyl butyrate, and Valproic acid all showed a significant change in chromatin heterogeneity (more than 10%) (Figure 5.2). Resveratrol showed an extremely strong effect in increasing chromatin heterogeneity (Figure 5.2B).
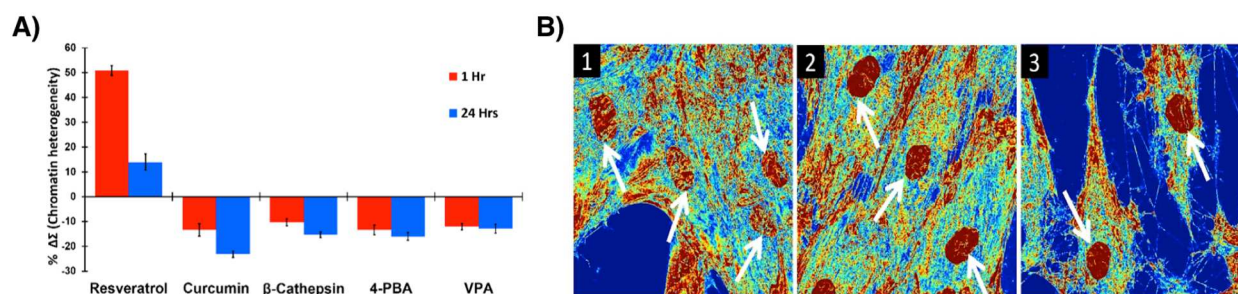
Figure 5.2. *Modulation of chromatin scaling of human mesenchymal stem cells with pharmacological agents.* A) Variations in chromatin packing density (normalized to control) for hMSCs treated for 1 hour and 24 hours with pharmacological compounds showing varying degrees of efficacy: Some show a moderate effect (≥10% D↓, ∑↓) and one shows a very strong effect (>50% D↑, ∑↑). B) Resveratrol increases variations in chromatin scaling. Representative PWS microscopy images of human mesenchymal stem cell nuclei before (1), 1 hour (2), and 24 hours (3) after 50 μM resveratrol treatment in regular culture media. Pseudo-color: heterogeneity of chromatin packing density (Σ). Arrows: cell nuclei.

Given the significant structural changes imparted by these compounds on chromatin scaling, the next step was to investigate whether these structural changes resulted in functional changes with regard to stem cell differentiation. To that end, hMSCs were now cultured in osteogenic cell culture media to promote differentiation in the presence of valproic acid (VPA), 4 phenyl butyrate (4-PBA), and beta-cathepsin, compounds which were shown to modulate chromatin scaling (Figure 5.2). Each of these treated groups of cells experienced enhanced osteodifferentiation compared to cells exposed to differentiation media without any additional pharmacological compounds (Figure 5.3).
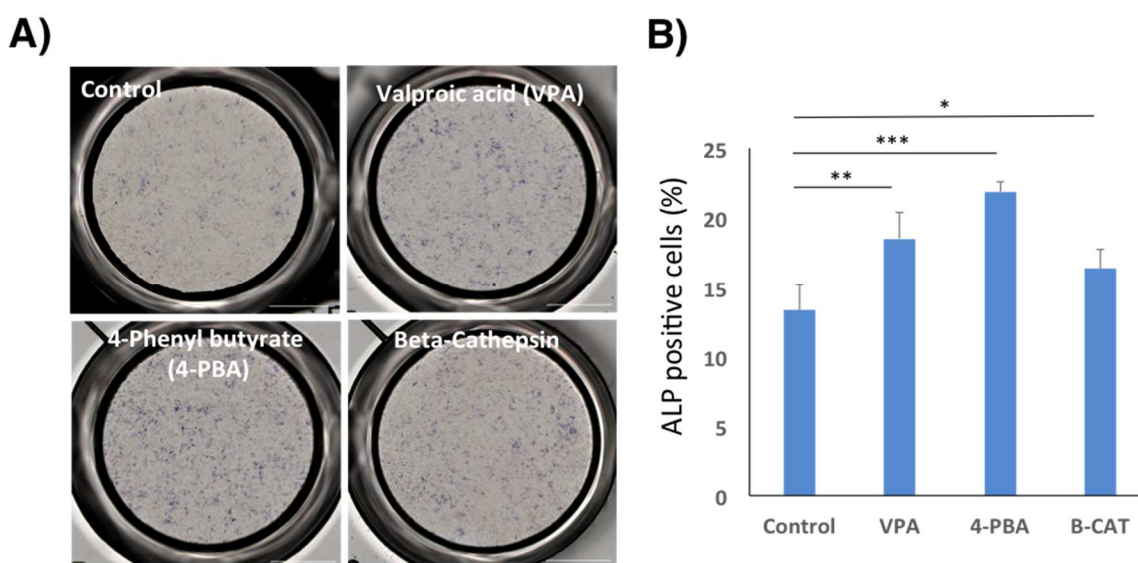
Figure 5.3. *Influence of pharmacological compounds that reduce chromatin scaling on osteogenic differentiation of hMSCs*. A) Alkaline phosphatase (ALP) staining of hMSCs treated with osteogenic

induction media (OM) only, OM + 100 µM VPA, OM + 1mM 4-PBA, and OM + 0.1 µg/mL β-CAT after 1 week culture. B) Osteogenic differentiation percentage of hMSCs treated with various CAPSs (Right). * p ≤ 0.05, ** p ≤ 0.01, *** p ≤ 0.001, n = 4 replicates. ALP staining and analysis was performed by Dr. Xinlong Wang, Ameer Lab, Northwestern University.

5.2.3. Effect of morphologically-induced nuclear deformation on chromatin scaling and stem cell function

While pharmacological compounds are one way to target chromatin scaling and control cell function, other methods can also lead to nuclear deformation and subsequent structural and functional changes. For example, morphological alterations of substrate can not only change the nuclear structure of a cell but also its motility and ability to divide or perform other cellular functions. In the context of stem cell differentiation, such morphological changes have the potential to affect differentiation.

To test the effects of altering substrate morphology on stem cell differentiation, we first measured chromatin scaling of hMSC cell nuclei with PWS microscopy that had been cultured on a micropillar substrate. Briefly, hMSCs were seeded on 7 µM high pillar substrates and were allowed to proliferate in regular media. PWS measurements were taken for cells on both flat surface and on pillars to determine the effect of the pillar substrate on chromatin scaling within nuclei. Cells on the edges of the pillar were excluded from the analysis. After capturing PWS images, the cells were fixed using 4% formaldehyde for about half an hour and then permeabilized with 0.1% Triton X-100 and blocked with Bovine Serum Albumin (BSA). Cells were then stained with DAPI and Alexa Fluor 488 phalloidin to locate the nuclear position and F-actin, respectively, for segmentation of PWS images and subsequent analysis. Nuclear deformation occurs for cells between pillars, and a decrease in chromatin scaling of stem cell nuclei on pillar substrate was observed (Figure 5.4).
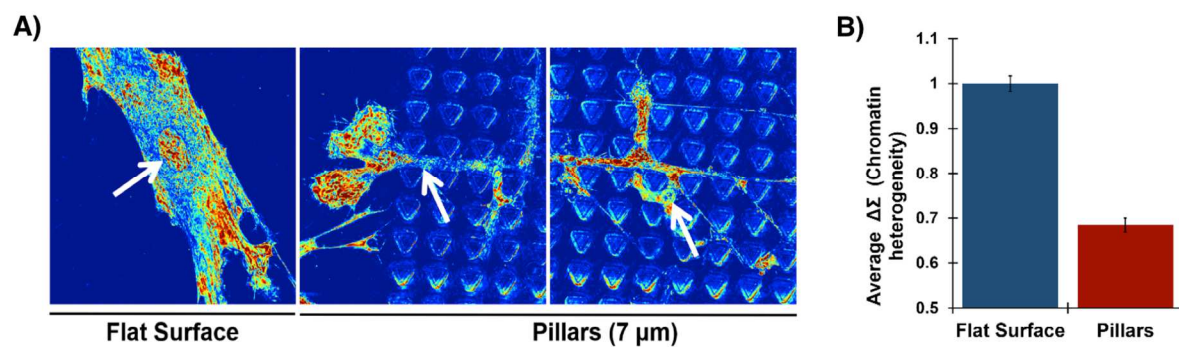
Figure 5.4. *7µm pillar substrate decreases chromatin scaling in hMSC cells.* A) Representative PWS microscopy images and quantification (B) of the effect of 7 µm pillar substrate on the variations of

chromatin scaling for human mesenchymal stem cells. Pseudo-color: heterogeneity of chromatin packing density (sigma). Arrows: cell nuclei. Variations in chromatin scaling decreased by 32% on the pillar substrate (p<0.001). Significance was determined using Student's t-test with unpaired, unequal variance on the average nuclear sigma normalized by the average nuclear sigma of the accompanying control group (flat substrate) between conditions for N=50 flat surface cells and 30 pillar cells.

To investigate whether these morphological alterations that resulted in changes in chromatin scaling for hMSCs had functional consequences, we cultured hMSCs on both micropillar and flat surfaces and induced differentiation with osteogenic culture media. Staining of F-actin and vinculin showed that the pillar structures also affected cell cytoskeletal organization as well as focal adhesion formation (Figure 4.5A, B). Cells on flat surface formed more stress fibers and mature focal adhesion relative to cells on micropillar surfaces. Additionally, osteogenic differentiation, which was assessed via alkaline phosphatase (ALP) and osteopontin (OPN) staining, cell nuclear shape index (NSI) = $4\pi S/l2$, where S and I represent the area and perimeter of nuclei, respectively, was further decreased relative to that of hMSC, suggesting more deformed cell nuclei. Quantification of the stains show significantly increased osteogenic differentiation, suggesting that the micropillar topography regulated gene expression and differentiation patterns of the hMSCs (Figure 4.5C, D).
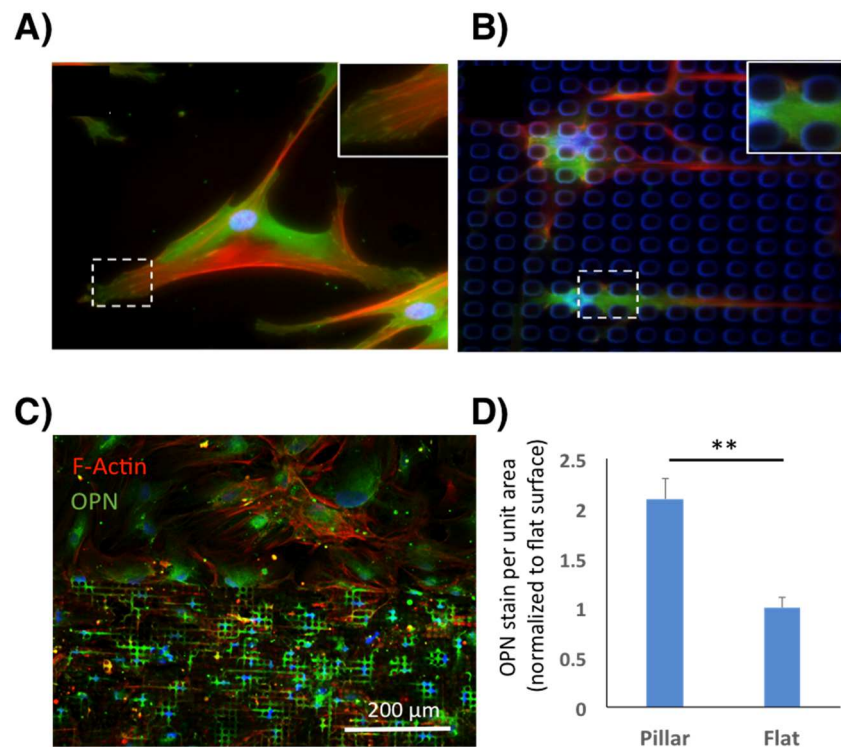
Figure 5.5. *Influence of morphological substrate on osteogenic differentiation of hMSCs.* A and B) F-actin (red), vinculin (green) and nuclei (blue) staining of cells on flat (A), and micropillar (B) surfaces. Inserts are magnified images of the dashed area highlighting the focal adhesion points. C and D) Immunofluorescence (C) and quantification (D) of osteopontin and F actin expression in hMSCs cultured on flat and micropillar surfaces for 21 days in osteogenic cell culture media. ** indicates $p < 0.01$. F-actin, vinculin, and nuclei staining and analysis was performed by Dr. Xinlong Wang, Ameer Lab, Northwestern University.

While experiments are ongoing and further mechanistic studies are necessary to fully explain the effect chromatin scaling is having on the differentiation process of these stem cells, this preliminary data shows that genome structure and compartmentalization can be affected through pharmacological and morphological stimuli and that such manipulation of chromatin scaling leads to cell phenotypic and/or differentiation changes that are potentially conducive to controlling cell fate in applications such as protecting or regenerating ischemic tissue.

5.3. CONCLUSION

Here we explored two strategies to increase cellular plasticity: pharmacological targets and morphological substrate alterations. Regarding the pharmacological strategy, we previously observed that certain compounds (β-cathepsin, a naturally secreted myokine, and 4-phenylbutyrate, a histone deacetylase inhibitor) can act on chromatin polymer to increase chromatin scaling, thus allowing for greater transcriptional exploration by the cells (16). Regarding the morphological strategy, although not fully understood, several researchers have reported changes in cell and nuclear morphology for cells cultured on micro- and nano-structured substrates (3, 104). Elongation of cell nuclei using micro-linear structures revealed the influence of cell nuclear shape on chromatin condensation, as well as epigenetic state modulation (105, 106). Enhanced expression of AcH3, H3K4me2 and H3K4me3 markers that regulate histone acetylation and methylation process was accompanied with elongation of cell nuclei, which facilitated the reprogramming of fibroblast to induced pluripotent stem cells (iPSCs). Depending on the specific features of the substrates, different deformation degrees of cell nuclei can be achieved (107,

108). Moreover, the differentiation potential of stem cells was found to be intimately related to the deformation degree of cell nuclei, which affected nuclear mechanical heterogeneity (109, 110).

We have identified pharmacological agents that decrease chromatin scaling in human mesenchymal cells and increase differentiation efficiency when co-treated during osteogenic differentiation. Similarly, we have identified a micropillar substrate that induces cellular and nuclear deformation, alters chromatin scaling, and subsequently likewise increases hMSC osteogenic differentiation. As gene expression and nuclear plasticity seem to be highly related, the capacity to engineer the topography of substrates to precisely control cell nuclear morphology and chromatin scaling may in the future enable them to function chromatin and cell fate regulators.

Future studies will also explore the effects of these pharmacological and morphological stimuli on cell response to hypoxia. We plan to develop an *in vitro* hypoxia model to identify the optimal pharmacological and/or morphological candidates or their combination, and then test these strategies *in vitro* in an ischemia/reperfusion model, which is well established in literature for small and large animals, to induce myocardial infarction in rats (111, 112).

While further study is needed to elucidate the mechanistic links between pharmacological or morphological applications to stem cell differentiation, these studies indicate that genome structure and compartmentalization can indeed be affected through pharmacological and morphological stimuli and that such manipulation of chromatin scaling leads to functional changes that can be applied to a variety of diseased states such as protecting or regenerating ischemic tissue.

Chapter 6: The transformation of the nuclear nanoarchitecture in human field carcinogenesis

This chapter is adapted from Bauer et al, Future Science Open Access, 2017, reference (113).

6.1. INTRODUCTION

For many decades, morphological alterations of the nuclear texture have been considered a hallmark of carcinogenesis. At later stages of disease, these changes are well characterized and detectable by light microscopy. Evidence suggests that similar albeit nanoscopic alterations develop at the pre-dysplastic stages of carcinogenesis. Using the novel optical technique Partial Wave Spectroscopic (PWS) Microscopy, we identified profound changes in the nanoscale chromatin topology in microscopically normal tissue as a common event in the field carcinogenesis of many cancers. In particular, higher-order chromatin structure at supra-nucleosomal length scales (20-350nm) becomes exceedingly heterogeneous, a measure quantified by the spatial arrangement of chromatin packing density scaling.

Traditional immunohistochemical staining and light microscopy have long been used as a way to identify alterations in nuclear structure during various stages of carcinogenesis. These alterations can have profound effects on many critical cellular functions, such as gene expression and DNA replication, but the role of chromatin structure on these processes in the earliest stages of cancer development is still not well understood. While the linear strand of DNA (the genetic code) contains all genes that can potentially be transcribed, other factors play a role in regulating its expression: the histone code helps to determine when and which of those genes are transcribed through modifications to histone tails, and the compartmentalization code, or how chromatin is packaged within the nucleus, also contributes to the regulation of gene transcription due to the relationship between chromatin scaling and accessibility of the genome. Despite this evidence of chromatin level alterations in carcinogenesis, the mechanisms of early nuclear alterations and the accurate identification of such alterations in a clinical setting require further understanding and the development of novel techniques.

Increasing evidence suggests morphological and genetic transformations that present once a tumor becomes microscopically identifiable also occur during early stages in the field of carcinogenesis. The field effect (also known as field carcinogenesis, field cancerization, or field defect) is the process

where the genetic/environmental milieu that produces a neoplastic lesion is present throughout the affected organ. Specifically, these genetic/epigenetic distortions provide a fertile field on which individual tumors eventually arise. Thus, the field effect can be used to identify and study the earliest events in carcinogenesis as some genomic, epigenomic, and structural transformations have likely occurred in tissue neighboring the tumor itself (114, 115). The field effect has been observed in colorectal, lung, esophageal, ovarian, cervical, breast, prostate, and head and neck cancers (114). Field carcinogenesis may explain the recurrence of tumors, whether metachronous or synchronous, and is already practiced in a clinical setting as a diagnostic marker (114, 116). In the case of colorectal cancer (CRC), many of the epigenetic (117), proteomic (118), and structural (119, 120) alterations have also been reported in the histologically-normal appearing colonic mucosa. Therefore, detection of markers representative of field carcinogenesis can be used to screen for and determine the risk of CRC development. However, as these physical transformations occur at the nanoscale, conventional microscopy cannot resolve the early, subtle structural alterations associated with field carcinogenesis.

Consequently, to detect these physical transformations that result from the field effect, we utilized Partial Wave Spectroscopic (PWS) microscopy, which quantifies the physical properties of cellular structure at the nanoscale (20-200nm), beyond the resolution limit of conventional microscopy (121). PWS microscopy measures the spatial heterogeneity of the nanoscale structure by measuring the variations in the refractive index quantified through the disorder strength (L_d). Using PWS microscopy, we have found that an increase in L_d is a universal event in many cancers, including colorectal, pancreatic, lung, esophageal, prostate, and ovarian cancers (120, 122-127). Furthermore, this increase in physical heterogeneity develops concurrently with the earliest known genetic events and precedes any known micron-scale alterations detectable by traditional histology (120).

From a biological perspective, the transformation in the cellular structure at these length-scales may have profound impact on a range of cellular processes. For example, in the nucleus, changes in chromatin scaling, either through alterations in compaction or the higher-order structure are associated with alterations in transcription (128, 129). While these transformations are often understood and analyzed through their underlying molecular transformation (e.g. differential in histone acetylation and methylation patterns), these molecular transformations converge on changes in the physical structure of

chromatin. Classically, these physical transformations have been measured by electron microscopy (TEM). Indeed, TEM has identified nanoscale changes in nuclei at the earliest stages of neoplasia in both the pre-neoplastic AOM (azoxymethane)-induced rat model, a commonly used inducible rat model for CRC, as well as in human colonic field carcinogenesis samples (44). While we found that several organelles display altered ultrastructure, the nucleus in particular is frequently transformed. Image analysis of the nanoscale chromatin distribution (e.g. differential chromatin compaction) was consistent with an increase in disorder strength as measured by PWS microscopy. Other optical techniques, such as quantitative phase microscopy, have observed similar results in field carcinogenesis (130-134). However, PWS is more sensitive than these methods.

Given their ubiquity and the role of chromatin in critical molecular processes, these results suggest that structural alterations in chromatin represent an early-stage event of carcinogenesis. There are several chromatin-remodeling mechanisms responsible for inducing changes in chromatin structure in early and field carcinogenesis. For example, using qRT-PCR methods, we found the histone deacetylases HDAC1, HDAC2, HDAC3, HDAC5, and HDAC7 all to be up-regulated in the field of human CRC (48). Aberrant regulation of chromatin has been implicated in functional alterations, such as changes in cell cycle, chromosomal stability, and gene expression (135). Recent work, including from our group, has focused on the importance of chromatin structure on transcriptional regulation (16, 76). Furthermore, we found that chromatin heterogeneity, as measured by the disorder strength, correlates with the heterogeneity of global gene expression and the heterogeneity of gene expression within genetic networks. Therefore, PWS microscopy is a powerful tool quantifying nanoscale chromatin structure and subsequent changes in gene expression and their role in the initial stages of carcinogenesis and tumor progression.

Through the analysis of voluminous clinical samples, we examined the interconnection of chromatin structure to pre-neoplastic spectroscopic markers of field carcinogenesis and its concomitant relationship to functional changes in biological processes often implicated in tumorigenesis. We found that an increase in nuclear disorder strength in carcinogenesis (i.e. topological heterogeneity within chromatin) is a common denominator of multiple molecular pathways, as it is observed in many different and diverse cancer types.

6.1.1. Nanoarchitectural transformation in early carcinogenesis

Electron microscopy has long been the gold standard for detecting nanoscale changes in cellular structure. To first measure nanoscale changes in the nucleus during early carcinogenesis, transmission (TEM) image analysis was performed on cells using colorectal field carcinogenesis as a model in humans. In this analysis, we found that there are significant physical alterations in the chromatin of pre-neoplastic cells that would otherwise be indistinguishable by standard histology and conventional light microscopy (Figure 6.1). As discussed above, however, traditional light microscopy is diffraction-limited and thus cannot provide information on the organization of structures below 200 nm. PWS microscopy addresses this problem by providing a nanoscale-sensitive technique as an efficient, low cost, and nanoscale sensitive cancer screening assay.
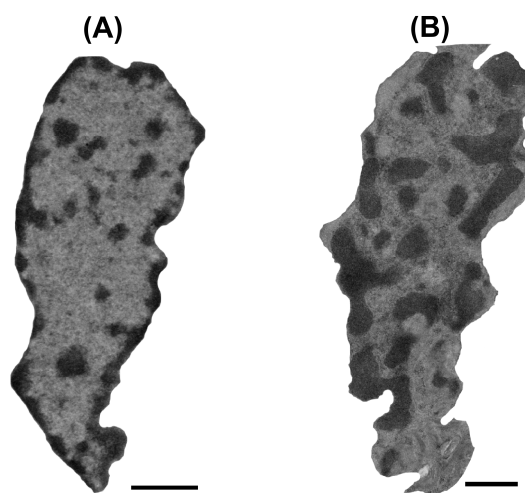
Figure 6.1. *Transmission electron microscopy (TEM) micrographs of rectal cell nuclei.* A) TEM section from healthy patient, and a (B) patient harboring tumor elsewhere in colon, representing the field effect of carcinogenesis. Scale bar corresponds to 1 um. TEM sample preparation and analysis was performed by Yolanda Stypula-Cyrus and Lusik Cherkezyan, Backman Lab, Northwestern University.

6.1.2. Summary of fixed-cell PWS microscopy measurements in human field carcinogenesis in seven different models

Using PWS microscopy, we have shown that, similar to commonly identified histological biomarkers, nuclear nanoscale alterations are a common denominator at the earliest stages in numerous types of solid tumors (Figure 6.2). In particular, we have previously shown using PWS microscopy that L_d is a measure of early neoplastic changes in cells, which quantifies the spatial heterogeneity of mass density at sub-diffractional length scales (~20-350nm). Table 6.1 summarizes the published L_d results

from over 1300 human patient samples across seven different types of cancers. The statistical significance of a difference between L_d values measured from patients falling into two different diagnostic categories was evaluated through the calculated effect size (the difference between the means of two groups divided by the cumulative standard deviation) and the p-value.

Tumor	Surrogate Site	Effect Size in **Nucleus**	*p*-value	Number of patients	Reference(s)
Colon	Rectum	144%	<0.01	343	(120, 123, 126)
Ovary	Endocervix	108%	<0.01	30	(122)
Thyroid	Histo-normal thyroid	85%	<0.05	18	(122)
Pancreas	Duodenum	109%	<0.01	35	(120)
Distal Esophagus	Proximal Esophagus	54%	=0.11	26	(124)
Prostate	Progressors vs. non-progressors	116%	<0.05	58	(125)
Lung	Oral Mucosa	104%	<0.001	825	(127, 136)

Table 6.1. *Summary of PWS microscopy measurements in human field carcinogenesis.* An increase in structural heterogeneity was observed in non-malignant cells obtained from cancer patients. In a cohort totaling over 700 patient samples from obtained from 7 different organs, topological heterogeneity increased in patients with malignancy. Within these studies, analysis of the nuclear structure was performed on 252 patients showing an increase in chromatin physical heterogeneity as measured by L_d across multiple cancer subtypes.

As seen, PWS microscopy measurements on clinical samples have shown an increase in L_d to be a universal event in multiple cancers, including colorectal, pancreatic, thyroid, lung, esophageal, prostate, and ovarian cancers (120, 122-127, 136). As an optical microscopy technique, PWS microscopy easily allows the user to localize L_d measurements within different cellular compartments of interest, giving quantitative values of nanoscale structural changes directly related to different organelles and in relation to various molecular functions (18). For example, squamous epithelial cells deposited onto glass slides are thin, flat, and have a large cytoplasmic area. Nevertheless, since PWS microscopy obtains spatially resolved maps of L_d, the disorder strength of the nucleus can be calculated independent of the ultrastructural transformation that occurs in neighboring organelles or within the cytoskeleton. Automatic detection and of nuclear L_d even within the context of the structural transformation occurring in the whole cell can be realized through the development of nuclear segmentation algorithms (137).
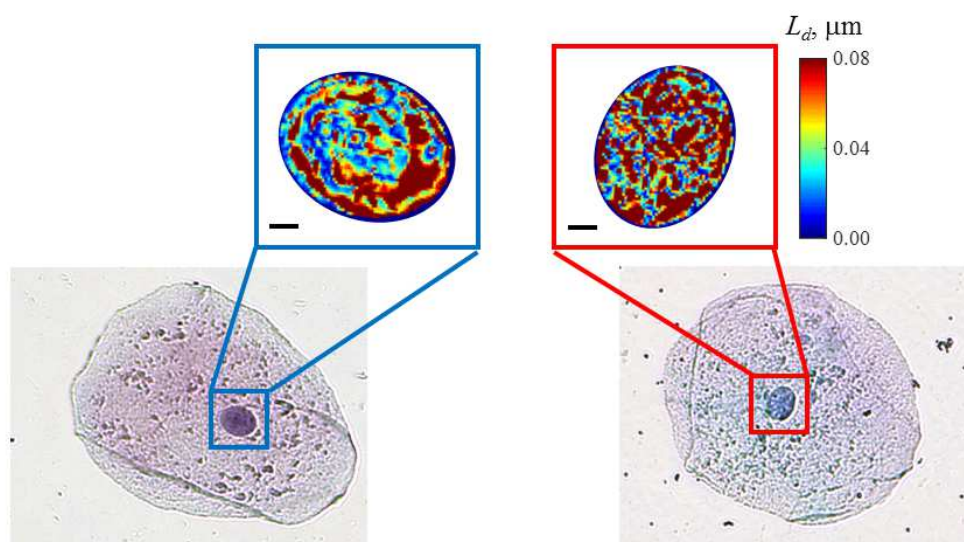
Figure 6.2. *Transmission bright field microscope images of histologically normal buccal cells.* Representative transmission bright field microscope images (bottom row) of histologically normal buccal cells from a healthy patient (left) and a patient with lung cancer (right). Nuclei were selected using the transmission images after which their disorder strength distribution was obtained (top row). Scale bar corresponds to 2 microns.

In the majority of cancer types shown in Table 6.1 (colon, pancreas, thyroid, and ovary), the PWS measurements were performed on tissue monolayers that were primarily comprised of columnar cells (colon – rectal cells, pancreas – duodenal cells, thyroid – thyroid cells, ovary – endocervical cells) in which the nucleus occupied > 80% of the cytology (122). Hence, the effect size and p-values reported in Table 1 are principally the changes in nuclear L_d in these organ types. However, in the case of other cancer types (lung and esophagus), the PWS measurements were obtained from isolated squamous cells (lung – buccal cells and esophagus – proximal esophageal cells). In these cell types, the nucleus in the cells we measured occupied a much smaller portion of the total cell. For example, the nuclei in the buccal cells occupied less that 25% of the total cell volume. Thus, to better understand the changes in nuclear L_d in squamous cells, we performed an independent study on 38 smokers with (25 subjects) and without (13 subjects) lung cancer. In this study, an image-processing algorithm was used to automatically calculate the nuclear L_d by measuring the changes to the nuclear nanostructure of oral epithelial (buccal) cells (Figure 6.3).
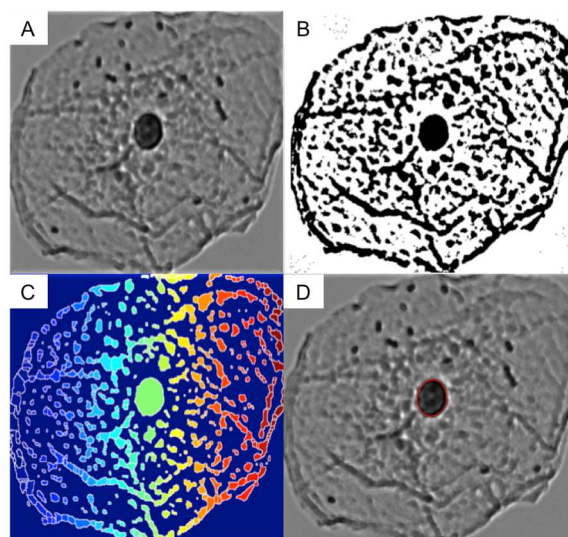
Figure 6.3. *Nuclei segmentation of an isolated, representative buccal cell.* A) Isolated buccal cell imaged with light transmission, (B) maximum entropy thresholding, (C) watershed segmentation, and (D) with resulting segmented nuclei outlined.

To examine the differences in buccal nuclear L_d due to lung cancer, we compared the nuclei from microscopically normal appearing buccal cells obtained from smokers with lung cancer to those of smokers who were neoplasia-free as confirmed by upper endoscopy. There was a significant increase in the nuclear L_d in buccal cells obtained from patients with cancer compared to those from control patients (Effect size 104%, p-value < 0.001) (Figure 6.4A). Importantly, the nuclear L_d and the cellular L_d (calculated as the average L_d from the nuclear and peri-nuclear area of the cell) had a very strong correlation (R > 80%). This increase in nuclear L_d is similar to the previously reported studies on human buccal cells in over 825 patients (including non-smokers, smokers with and without lung cancer etc) (127, 136). These results validates that PWS microscopy was able to detect changes to the nuclear nanostructure that provided indication of an early disease stage not detectable by traditional histological methods distal to the site of the tumor.
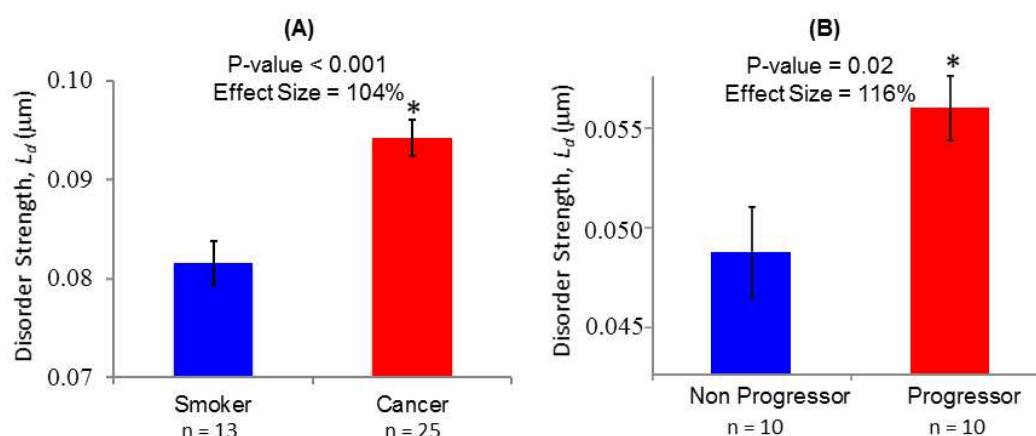
Figure 6.4. *Nuclear L_d increases in human field carcinogenesis.* A) The nuclear L_d was calculated from buccal cells obtained from the oral mucosa of smokers (control) compared to patients harboring lung cancer. Nuclear L_d is increased significantly in buccal cells from cancer patients (Effect size 1.04, *p*-value < 0.001, n = 38 patients total). Panel B) shows the nuclear Ld calculated form FFPE prostrate tissue samples from progressors and non-progressors. FFPE slides were stained with low concentration of H&E to provide contrast. Nuclear L_d is significantly increased in the patients who went on to develop the disease (progressors), compared to the benign form (non-progressors). Therefore, nuclear L_d be a useful marker in lung cancer screening, while the prostate nuclear L_d data represents the first test to differentiate those who will actually go onto to present malignant forms of the disease, which will correspond to alterations in biological pathways (i.e. chromatin structure and gene expression). Error bars represent standard error.

In addition to its ability to identify patients with early disease in multiple cancer types, we have also shown the utility of PWS microscopy as a prognostic tool to measure disease aggressiveness (125). As an example of this approach, we utilized PWS microscopy to measure topological alterations in the nucleus of progressor prostate cancer patients in comparison to non-progressor controls. Specifically, we studied the relationship between chromatin structure and prostate cancer aggressiveness by performing PWS microscopy measurements on prostate tissue sections obtained from patients by biopsy. Significantly, we observed an increase in L_d within the nucleus of future progressors compared to that measured in non-progressors (effect size 116%, p-value <0.05, n = 20 patients) (Figure 5.4B) (125). In this analysis, we examined nuclear L_d differences in these tissue sections obtained from the histologically normal prostate epithelium. Formalin-fixed paraffin embedded (FFPE) slides were stained with low concentration of hematoxylin and then segmented using the automated nuclear segmentation algorithm to automatically analyze the nucleus. Given the sensitivity to the resulting prostate cancer progression, PWS microscopy could be an important tool in prostate cancer screening, as the current prostate-specific antigen (PSA) test cannot differentiate men who will go on to develop aggressive cancer.

6.2. DISCUSSION

In summary, these studies indicate that the nanoscopic transformation of the nucleus is a universal event in early carcinogenesis seen across many cancer types including colon, lung, pancreatic, esophageal, thyroid, and ovarian cancers (122-127, 136, 138) and is potentially linked to cancer cell aggressiveness (125). Owing to the sensitivity of PWS microscopy to measure these physical alterations within the nucleus, this technology can (1) provide a non-invasive method for early cancer risk stratification, (2) provide a means to obtain prognostic information on tumor aggressiveness, and (3) shed light on the interplay between physical structure and molecular transformation in oncogenesis.   Given the importance of chromatin structure on biological processes and the observation of its transformation during cancer initiation and progression, we utilized PWS microscopy to examine the transformation of nuclear nanostructure as measured by our optical measurements during human field carcinogenesis. We have reported that similar alterations in the nanoscopic heterogeneity of chromatin structure develop at a pre-dysplastic stage of carcinogenesis (e.g. field carcinogenesis) in microscopically normal-appearing cells. For example, in colorectal tissue monolayers measured, the nucleus occupied a significant portion of the columnar cells (>80%) forming the colonic crypts. Thus, changes in nuclear L_d during carcinogenesis would dominate the measured PWS signal. Furthermore, as PWS measures fluctuations in refractive index, it would be expected that dense regions of nucleic acids, ie. chromatin, would dominate the PWS signal. Indeed, a cell line study showed that while the cytoskeleton also contributes to increased L_d, the nuclear signal dominates, and nuclear differences in heterogeneity are the driver of tumorigenicity between different HT-29 cell types (139, 140).

To demonstrate the utility of PWS microscopy as a tool in early cancer screening changes detected by PWS microscopy are inherently nanoscopic (on the order of 20-200nm) and have been independently identified on electron microscopy (44, 141). Within chromatin, the nanoscopic length scales to which PWS microscopy is sensitive are those that have been identified to be critical regulators of gene transcription. In particular, these lengths span from supra-nucleosomal organization all the way into higher-order looping domains. Optical techniques such as PWS microscopy that can quantify the alterations in chromatin folding at this nanoscale range can serve as sensitive, cost-efficient approaches

for cancer screening. Likewise, given its ubiquity in early carcinogenesis, this physical transformation may in fact serve as a universal marker for carcinogenesis (it has been invariably observed to increase in >700 patients across 7 different types of cancers (Table 1; (122-127, 138)). Thus, this increase in nuclear nanoscale structural heterogeneity, as measured by PWS microscopy, could be the common denominator of multiple unique molecular pathways associated with distinct cancer types and patients. In order to specifically measure the transformation of the chromatin nanostructure in early carcinogenesis, we analyze topological changes within the nucleus of cells for colon, ovarian, thyroid, pancreatic, esophageal, prostate, and lung cancers. Given the near universal observation of this transformation, the disorder strength can be used as a universal biomarker for pre-neoplastic changes. These results indicate not only the utility of optical biomarkers for cancer screening, but also the underlying drivers of cancerous processes, such as chromatin alterations.

Alterations in chromatin compartmentalization and folding can influence gene expression in several ways, such as by non-linearly changing the accessibility of chromatin binding sites to transcription factors or by modulating the diffusivity and binding affinity of enzymes such as RNA polymerases. Therefore, there is a significant effort to understand how the differential packaging of the genome impacts cellular processes as well as how these functions are altered during cancer (9, 142). The differential compaction of chromatin is influenced by a wide array of factors that range from molecular transformations (e.g. histone deacetylase activity) to the physio-chemical (e.g. local osmolarity, pH, and ionic conditions). While there are molecular methods to directly analyze and measure the alterations in histone acetylation or other chromatin modifying enzymes in carcinogenesis, there are a number of challenges to directly monitor these additional physio-chemical regulators of chromatin. As a result, indirect measurements of the overall nanoscopic folding of chromatin, such as those provided by TEM or PWS microscopy, could shed light on the convergence of these molecular and physiochemical forces during early carcinogenesis (48, 143).

6.3. CONCLUSION

Here we demonstrate the near-universal link between nanoscopic changes in chromatin physical topology in early tumorigenesis in colorectal, lung, esophageal, ovarian, cervical, breast, prostate, and head and neck cancers. These previously unidentified nanoscopic transformations mirror the widely recognized microscopic alterations recognized both in dysplastic and malignant cells. This observation of increased heterogeneity of higher-order chromatin structure at supra-nucleosomal length scales, as measured by PWS microscopy, is a common denominator of multiple molecular carcinogenesis pathways and may serve as a marker of early carcinogenesis across multiple cancer types and as a prognostic indicator of aggressiveness in prostate cancer. Given that these alterations in higher-order chromatin structure could alter molecular function, they could also potentially used to measure of chemoevasive. If this can be demonstrated, PWS microscopy would have significant clinical relevance to tailoring epigenetic therapies and personalized medicine as it would provide a means to assess pre-malignant risk, measure tumor aggressiveness, and assess chemoevasive potential. Furthermore, our group has recently developed a live cell PWS system (38), which can address the question of how nuclear nanostructure is organized in live cells, unobscured by potential artifacts of fixation, and the real-time functional consequences in human derived cell lines. While fixed cell PWS nanoscopy is expected to be vital for cost-effective cancer screening and risk-stratification, this live cell extension of PWS microscopy can have significant implications and applications in the field of personalized medicine and tailoring cancer therapeutics to an individual's tumor cells.

Chapter 7: The Greater Genomic Landscape: The heterogeneous evolution of cancer

This chapter is adapted from Almassalha, Bauer, Chandler, Gladstein et al, Cancer Research, 2016, reference (17).

7.1. Current models of tumor formation and their limitations

Classically, evolution has been studied as the set of mechanisms that confer heritable traits from parents to their progeny. In this view, evolutionary sampling confers traits that can be advantageous to the progeny under the appropriate circumstances. As such, under stress conditions that favor a given set of traits, the populations with those traits will clonally expand and predominate. In multicellular organisms the distinction between progeny and evolutionary fitness becomes blurred. Intuitively, clonal selection of cell populations within a tissue can be advantageous to the whole organism, but are not reproductively heritable to the multicellular progeny. For the cell population at the tissue level, the discovered adaptions are not classically *selective* but *capacitive*, i.e. the resulting heterogeneous population confers an advantage to a plurality of traits since a broader distribution can help in the face of new stresses. However, by definition, this increase in traits fundamentally changes the tissue over time.

The most studied model of this evolutionary driven functional transformation in humans is cancer (144-148). Largely unanswered, however, are the mechanisms by which adaptive sampling occur and how these events could result in the formation of tumors. Results have historically shown a plasticity in the origin of tumors, with heterogeneous mutational and epigenetic events occurring throughout a challenged organ preceding an eventual pathological expansion (146, 149, 150). Furthermore, tissues under constant energetic and replicative pressures account for the demonstrable majority of tumors (151). These observations, however, do not fully explain the broad distribution of molecular events that can precipitate tumor formation. Contemporary views on the origin of tumors derives from the monoclonal expansion of cells (tumor stem cells, clonal selection due to mutations or chromosome instability) into a lesion before the occurrence of the observed heterogeneous acceleration (145). This view, however, does not explain the functional diversity in tissues under non-perturbed conditions even within cells of the same lineage (152).

Here we present a hypothesis that tumors form due to heterogeneous adaptive selection in response to environmental stress through *intrinsic* genomic sampling mechanisms. Specifically, we propose that eukaryotic cells intrinsically explore their available information in response to stress under normal conditions, long before the formation of a cancerous lesion. This information, the Greater Genomic Landscape (GGL), is the available distribution of functional states: the current functions of the cell (proteomic/metabolic) and possible future states (genes that can be expressed/repressed or mutated). In essence, the GGL hypothesis merges critical traits of information theory and evolutionary biology to explain tumorigenesis as something other than an accidental byproduct, but a consequence of multicellular fitness. Specifically, the intrinsically encoded exploration of proteomic and genomic information is a main adaptive advantage of multi-cellularity and occurs primarily at three levels and time scales: (1) post-translational proteomic sampling (rapid), (2) epigenomic sampling (intermediate), and (3) mutational sampling (long term).

Briefly, let's consider some of the intrinsically encoded mechanisms of information sampling for these three mechanisms. At the proteomic level, there are numerous non-transcriptional ways to alter cellular function. For instance, studies of yeast under stress demonstrate eukaryotic cells employ a plurality of strategies to respond to conditions, including varying abundance and location of proteins (and mRNA), leading to a heterogeneity of initial conditions and variability of response to stress (153, 154). At the epigenomic level, there are both enzymatic and non-enzymatic ways to alter the information space. In tumorigenesis, there are numerous demonstrations of chromatin remodeling enzymes being critical drivers in chemoevasion and tumor formation. However, there is also an often-overlooked level of epigenetic heterogeneity, which is to vary the initial configurations of chromatin structure to change accessibility and probability of expression for genes from cell to cell. Critically, both the proteomic and epigenetic mechanisms happen at time scales that are faster than the division of cells, allowing cells to discover new adaptions during exposure to stress (Figure 7.1A). As demonstrated in (Figure 7.1B), the presence of rare subpopulations occurs at significant levels even while maintaining an "average" population. An increase in the heterogeneity of subpopulations does not necessarily transform the overall tissue function, but it can have a profound effect on the information space available to respond to stress conditions. Classically, this is considered at the time scale of cell division, with mutational alterations are

as the predominant mode of increasing the information space for a tissue by creating inherently new potential functions. In this way, mutational transformation is also the most classical example of tumor heterogeneity, but occurs at time scales that are challenging to target pharmacologically.
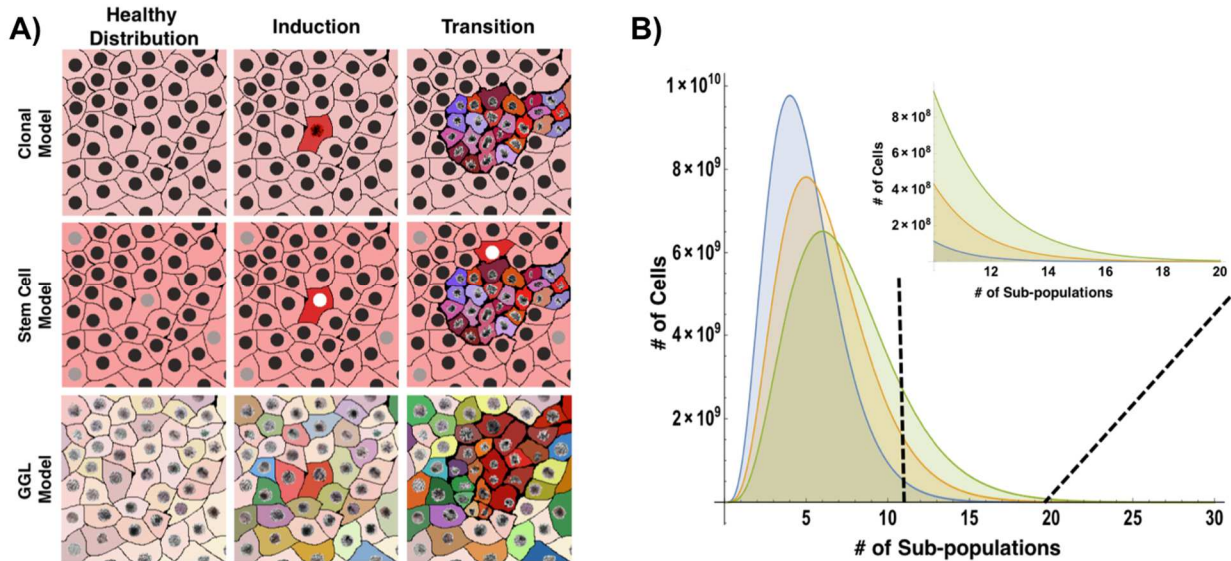
Figure 7.1. *Tumor formation models.* A) Clonal expansion secondary to perturbation is classically defined as the cause of tumorigenesis. Clonal expansion often well characterizes haematopoietic tumors and pediatric tumors, but often fails to explain the underlying heterogeneity observed in solid organ tumors. In the CSC model, tumors arise due to the formation of stem cells that give rise to new tumor with multiple subtypes, allowing for a partial heterogeneity in cell origin within a tumor. In contrast, the Greater Genomic Landscape focuses on the general feature of multicellular systems: their potential to change their function in the face of stress. In the GGL model, tumors arise due to the probability of a population arriving at a cancer state due to the selection of a large distribution of cell subpopulations (and functions) and from increased information sampling that it produces. B) Consider the case of 5 predominant subpopulations within the tissue for a given cell type. Assuming a population follows from a gamma distribution, small changes in the heterogeneity (scale parameter) result in large deviations in the number of subpopulations. As such, while the average population and tissue function does not change significantly, the total number of possible states (and functions) has increased.

7.2. Greater Genomic Landscape model of tumor formation

Consequently, repeated and multidimensional stressors are more likely going to select for cells with traits that enhance the capacity to search the GGL, not just for a particular set of proteomic pathways or initial traits, which in single cell systems is often termed "bet-hedging". As a result, each perturbation increases the heterogeneity of the underlying tissues by favoring a broader distribution of semi-unique states and cells that have the greatest plasticity (capacity to search for new functions). Over time, this

differential sampling of the genome produces an increasingly diverse population, commonly observed at the detection of overt tumors. It is this tissue heterogeneity and intrinsic plasticity that acts as a conserved evolutionary mechanism that favors more exploratory cells in eukaryotic systems, commonly resulting in tumor formation.

In this view, tumor formation is an evolutionarily-driven information-sampling problem arising as stress induces the population of cells to sample the information coded within their genomes and proteomes to collectively maintain tissue function. The origins of these stresses are innumerable (alcohol, smoking, infections, etc) and as such, the tissue does not *a priori* know what mechanism of evasion will work for every perturbation. Instead, cells carry a limited repertoire of encoded proteins that include intrinsic samplers to rapidly and probabilistically search the GGL for solutions to maintain the underlying function of the tissue. This occurs not by just rapidly inducing all genes, but by combinatorially exploring the information space encoded across numerous subpopulations. Within an individual cell, these intrinsic samplers initiate a probabilistic search response at both the proteomic (post-translational modification) and genomic (chromatin remodeling, mutational transformation) levels. The cells that fail during this sampling under stress undergo apoptosis or mitotic arrest after a few hours.

For this mechanism to be a central evolutionary property of multicellular organism, there must first be a distribution of time scales during which the levels of stress response occur. In particular, sampling must be relatively rapid in comparison to mechanisms of cellular clearance, i.e. apoptosis and immune-clearance. Interestingly, evidence of this separation of timescales has been observed previously, even indicating possible transition states between death and survival (155). Irreversible commitment to apoptosis occurs over the course of several hours, while proteomic transformation and chromatin remodeling are very rapid (< a few minutes). This suggests that irreversible commitment to apoptosis is delayed in order to give cells time to find stress evasion mechanisms. Without this complementary intrinsic sampling mechanism, our tissues would fail under mild perturbation from unique stressors.

A second requirement of such a mechanism is the presence of a central convergence point between exploration, apoptosis, and cellular arrest. As such, we propose that one regulator of intrinsic sampling of the *Greater Genomic Landscape* is mitochondrial membrane potential, Ψ_m. Mitochondria are ubiquitously implicated in diseases, specifically diseases of aging; e.g. tumors, neurodegeneration, and

atherosclerosis (156). Beyond this central association, disruption of Ψ_m has been shown to regulate the epigenetic structure of chromatin, molecular signaling cascades, and post-translational modification of cytoplasmic proteins (156). Furthermore, processes directly linked to Ψ_m include apoptosis, proliferation, and senescence (157). Consequently, Ψ_m could serve as the central barometer of cellular fitness, mediating sampling, apoptosis, and senescence concurrently. In this model, the disruption of Ψ_m would simultaneously induce proteomic and genomic exploration, initiate the apoptosome, and potentiate cell cycle arrest. If the stressor is not resolved, either extrinsically or intrinsically, cells would commit to apoptosis to limit their use of resources required for the remaining cells.

The evolutionary selection of more robust samplers and an increasingly heterogeneous population of cells occurs primarily for two reasons. First, continuous maintenance of many traits is energetically unfavorable for an individual cell. Secondly, more robust samplers and a greater number of initial states will increase the likelihood of finding traits that prevent tissue failure during duress. With each perturbation event, selective pressures will transform tissues by increasingly favoring a broader distribution of cellular configurations and cells with increased plasticity. Over time, this accelerates the evasive fitness and increases the cellular heterogeneity present within the affected tissue (145). Currently, this process is considered as an accidental byproduct of selective pressure favoring the initial configurations (tumor stem cells, clonal expansion) over the general feature (heterogeneous, elastic sampling in response to normal stress across entire cell populations) (144, 145, 147-149). Unlike evolutionary fitness being derived from tumor stem cells or accumulated variations from clonal expansion, the GGL hypothesis indicates that differentiated cells are a major component in tumor formation because of their capacity to still explore their information space in the face of repeated stressors *at timescales preceding cell division*.

With Ψ_m acting as one barometer of fitness, we expect evolutionary selection to produce cells with the following combinations of features. Cells that (1) more rapidly and thoroughly explore of the genomic space; (2) have previously acquired a higher stress tolerance; (3) preferentially arrest to extend the survival; and (4) have a broad distribution of initial states (Figure 6.1B). Most commonly, we study the mechanisms that increase damage tolerance, preferentially induce arrest, or more recently, increase the initial states (144-149). Unfortunately, we are currently lacking thorough studies that focus on the primary

feature of tumor formation: heterogeneous initial states and rapidly adaptive configurations that result in a larger exploration of the Greater Genomic Landscape in healthy tissues.

Previous characterizations of such an exploratory mechanism have too narrowly focused on global gene induction as a fitness mechanism. However, global gene induction should not be confused with differential exploration and tissue heterogeneity. In the GGL model, differential exploration selects for numerous populations of cells within a healthy (or unhealthy) tissue under the same stress. For example, at least two different mechanisms can favor cell survival in the presence of a toxin: (1) inactivating genes involved in the apoptotic cascade or (2) creating proteins that expel the stressor. As a result, repeated or multidimensional perturbations do not select for one trait, but instead broaden the distribution of initial cell states and favor more elastic samplers. Critically, this feature is likely conserved in normal tissues, not an adaption unique to carcinogenesis.

If evolutionary sampling of the available information space (GGL) is a critical feature of tumorigenesis and normal tissue function, what are some potential mechanisms that would increase the exploration of the GGL and enhance the chance of cellular survival during stress conditions? One possible mechanism would be to delay the irreversible commitment to apoptosis, thereby extending the duration of exploration and allow the search of more possible evasive combinations (158). A second mechanism would be the transformation of chromatin remodeling enzymes to increase the efficiency of combinatorial searches in response to stress (159, 160). A third mechanism could be to broaden the heterogeneity of chromatin structure of the cellular population, i.e. – vary the configurations to increase the coverage across the entire population (161). By increasing the distribution of chromatin organization across cells, each cell within the population has a different initial configuration state that produces a semi-unique exploration, enhancing the total information space (Figure 7.2). Deviations between subpopulations in structure (as small as a 1% difference in the physical configurations of chromatin), significantly influence the total possible configurations within a subpopulation.
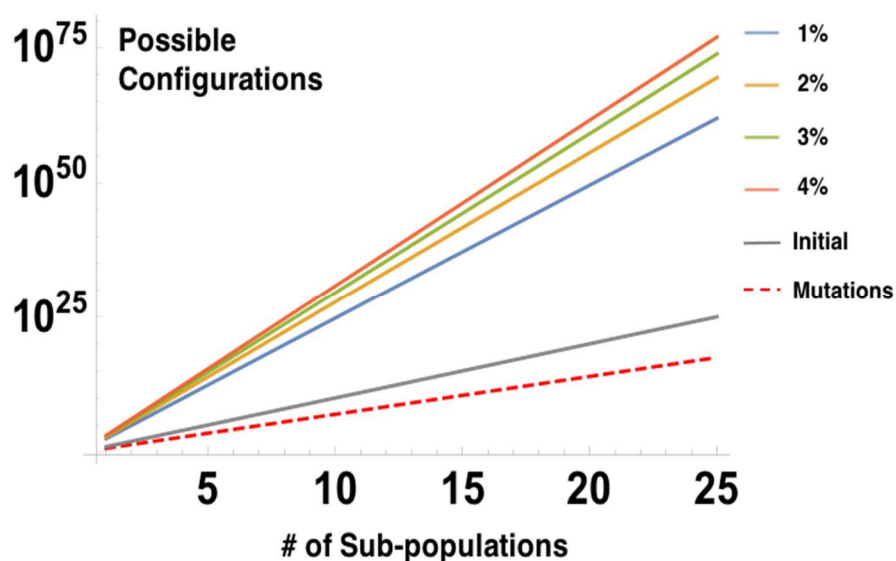
Figure 7.2. *Available information space for cellular subpopulations.* Conservative estimates in the heterogeneity of subpopulations for different types of cellular variance (assuming subpopulations are distinct, but largely share the same features). If cells each express 1000 proteins and only 10 are different between subpopulations (99% overlap in function), then 10^n potential variations are possible. Likewise, if each subpopulation has 5 distinct mutations, $\sim 3 \times 10^{17}$ genetic states are possible. Often overlooked, however, is the effect of varying the physical configurations of chromatin. Even a 1% difference in the organizational topology would allow 8.4×10^{61} potential responses for 25 subpopulations. Given this asymmetry, drugs targeting variations in chromatin organization (Chromatin Protective Therapies) can greatly reduce the probability of either acquiring tumorigenic characteristics or chemoevasive expression.

Even with conservative estimates, this suggests that the underlying heterogeneity of chromatin organization (and the ability to modulate the structure) have a disproportionate influence on potential tissue function, cellular diversity, and fitness. Even without taking into consideration additional influences such as information sharing between cells, distinct cellular populations, and the time evolution of chromatin structure, this suggests an overwhelming non-mutational/non-chemical influence of physical organization of chromatin on the probability of tumor formation. While not every potential configuration would be attempted in every stress, it is the potential variations (the total number of possibilities) that assist the tissue in the face of stress. It is important to note most states would have no effect (or could be a negative) in a particular situation, but across many different exposures, the potential space becomes the critical feature. The obvious trade off is increased variations increase the probability of acquiring negative traits. Interestingly, the observation of physical heterogeneity of chromatin (variations in fractal

dimension) as a prognostic marker in cancer is well conserved in solid tumors and may be a proxy for the underlying information space within a tissue (4, 162).

7.3. Implications of the Greater Genomic Landscape model

Finally, if exploration of the Greater Genomic Landscape is a critical feature in tumor formation and the emergence of chemotherapeutic resistance, what would the implications be on the treatment and prevention of tumorigenesis? To date, the predominant approach to tumor treatment largely couples local resection with combination chemotherapy. The essence of this strategy is to reduce the number of initial configurations by resection, inhibit a predominant growth mechanism if possible, and non-selectively overwhelm as many evasion mechanisms present in tumors as possible (163). This approach can be highly efficacious but has significant limitations and risks, as such, newer strategies have attempted to more narrowly target tumor cells based on theories of clonal expansion as the predominant feature of tumor initiation (163). However, if exploration of the Greater Genomic Landscape is a general evolutionary feature, such narrowly focused strategies will prove generally ineffective due to the inherent heterogeneity and plasticity of the target cells – cells will always have more mechanisms to promote survival than can be focally eliminated. Furthermore, both approaches would not be adaptable to the prevention of tumor formation, a long sought-after but largely elusive strategy (164).

Instead of only targeting particular *drivers* for each tumor, one approach would be to limit genomic exploration mechanisms (sampling) by targeting the physical structure of chromatin using low-dose Chromatin Protective Therapies (*CPTs*). As described above, alterations in the configurations of chromatin from cell-to-cell and the remodeling of chromatin allows cells to search for new mechanisms that aid in cell survival at low cost. Furthermore, work from our lab suggests a correlation with the underlying chromatin organization and the heterogeneity of gene expression for critical processes, including proliferation and apoptosis. Moreover, we have consistently found that structural alterations in chromatin precede the development of tumors in both human and animal models of carcinogenesis (44, 48, 120, 121, 123, 127). Likewise, theoretical modeling and experimental results have shown that changes in the physical environment can independently modulate transcription (76, 165, 166). As such, the physical transformation of chromatin could have a significant role in tumor formation and

chemoresistance independent of effects mediated by epigenetic chemical modifications. Therefore, we propose expanding beyond only focusing on molecular pathways and specific chemical regulators, but to develop tools that can control the overall physical topology of chromatin.

Through this approach, CPTs would complement existing strategies by decreasing the cumulative adaptive potential of cells. Specifically, an adjuvant CPT would work by decreasing the probability of emergence of secondary proliferative and evasive mechanisms by preventing genomic sampling through restriction of the possible configurations of chromatin. By acting on the overall physical structure of chromatin, CPTs restrict the global sampling capacities of cells to reduce the combinatorial dimensions of evasion (Figure 6.2). Likewise, CPTs could be a long-sought-after prophylactic approach for patients with high-risk mutations by preventing accumulated sampling in addition to the known drivers of tumor formation. These prophylactic CPTs could additionally be employed therapeutically to restrict the accumulation of adaptions between courses of conventional treatments. In this approach, CPTs would prevent the possible sampling of different states during stress – reducing the probability of survival to cells to a considerably smaller population of cells that had previously acquired a favorable configuration.

In summary, we propose an evolutionarily conserved mechanism derived from information sampling that drives the observed heterogeneity in tumor formation at the origin of healthy tissues. Specifically, we propose that tumor formation results from repeated stressors driving normal tissues to explore their *Greater Genomic Landscape*, i.e. the collective information space available to cells, to prevent organismal death in the face of stress. The exploration of the *Greater Genomic Landscape* is potentially mediated by mitochondrial membrane potential in conjunction with the potentiation of apoptosis and induction of cell cycle arrest. Further, we propose that this could lead to the development of *Chromatin Protective Therapies*, which target global genomic exploration by controlling the physical topology of chromatin and the ability of cells to generally access genomic information. These *Chromatin Protective Therapies* would be a new class of prophylactics and neoadjuvants that lower the probability of premalignant transformation and the development of chemoevasion mechanisms by restricting the cellular capacity to explore their greater genomic landscape.

Chapter 8: Chromatin scaling and macrogenomic engineering in cancer evolution

This chapter is adapted from Almassalha, Bauer, Wu et al, Nature Biomedical Engineering, 2017, reference (15).

8.1. INTRODUCTION

Fully sequencing the human genome has allowed unprecedented exploration of the roles that genes play in diseases, including neurological and autoimmune disorders, heart disease, and cancer. One of the most significant findings from the human genome project was the fact that, in many cases, these diseases do not depend on the behavior of individual genes, but on the complex interplay between tens to thousands of genes over long periods of time (167-169). Despite this emerging understanding that many human diseases are thus inherently multifactorial and genomic in nature, no technologies have been developed that allow for the simultaneous, predictable engineering of multidimensional transcriptional interactions.

In this regard, many studies have explored the mechanisms that control the transcription of genes and provided new understanding of the epigenetics that govern diseases. At the level of histones and nucleosomal organization (~10 nm), it is widely recognized that the physical structure of chromatin plays an important role in governing gene expression (170, 171). In a disease where particular genes or their mutational variants produce a hierarchal, central network topology, this information can be leveraged to control many genes simultaneously by targeting a key node (Figure 8.1A). These insights have greatly expanded our knowledge of the basis of genetic diseases, but they face the limitation that genetic changes to transcription factor binding sites, nucleosomal remodeling, or specific gene compartments (172, 173) determine the activity of a few genes only; yet most genetic networks are inherently decentralized or diffuse (Figure 8.1B). Therefore, methods to manipulate the expression patterns of many genes simultaneously for non-hierarchal diseases, including most cancers and many diseases of aging (Figure 8.1C), are largely missing. To address this need, here we present a method to target supra-nucleosomal (>10 nm) chromatin physical structure as a means to predictably modulate global patterns in gene transcription.
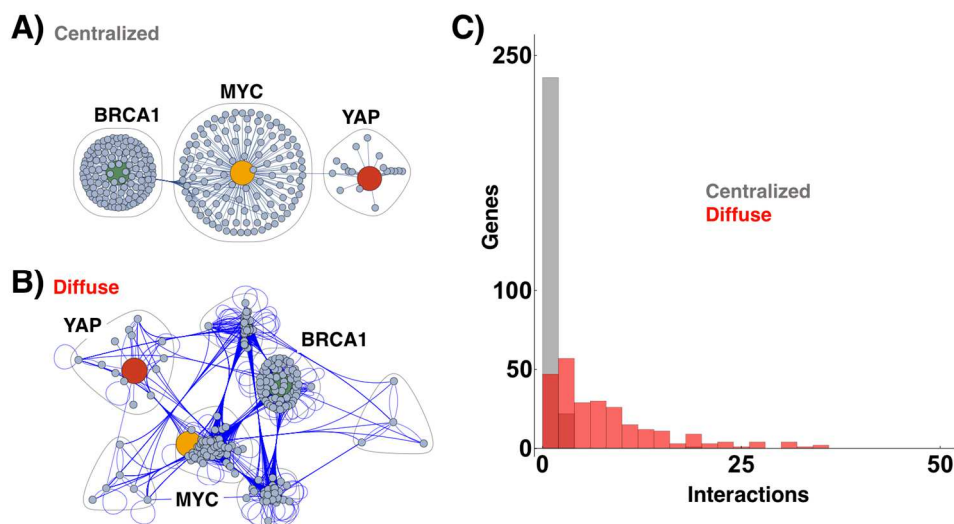
Figure 8.1. *Genomic networks are highly interconnected and decentralized.* A) Classically, the role of critical genes such as MYC, BRCA1, and YAP has been viewed in the context of a hub-spoke model, where these genes form the critical link between the elements in the system. B) However, evidence has shown that the full mapping of the interactions that occur for all genes within a given interaction network shows a diffuse plurality of connections and broad network redundancy. C) Mathematically, the divergence in these models can be represented by the number of connections each gene shares. In the classical hub-spoke system, most genes are anchored only by the central elements (such as BRCA1, c-MYC and YAP). In most genetic networks, however, this is a major oversimplification. Indeed, most genes share direct interactions with at least 5 other genes within the network necessitating a strategy to target the overall regulators of gene transcription. Gene network analysis was performed by Luay Almassalha and Wenli Wu, Backman Lab, Northwestern University.

We developed a model that explains the role of supra-nucleosomal chromatin organization on gene expression at the level of physiochemical interactions (summarized in chapter 2). Testing the predictions from this model with experimental results obtained from nanoscale measurements of chromatin structure using partial wave spectroscopic (PWS) microscopy, which measures nanoscopic alterations in the scaling of chromatin packing density with a sensitivity to chromatin organization between 20 and 350nm, in live cells and from measurements of gene expression using mRNA microarrays, we show that altering the packing-density scaling of chromatin produces predictable changes in gene expression and that one of the main functional roles of the physical organization of chromatin is controlling the genomic information space as well as intercellular transcriptional heterogeneity. Accordingly, whereas existing understanding of transcriptional regulation has focused on means that regulate individual genes (modifying transcription-factor binding domains, performing nucleosomal post-translational modifications, or localizing genes to chromatin compartments), the approach introduced in

this work modulates the physical structure of chromatin for global transcriptional modulation (Figure 8.2A-D).
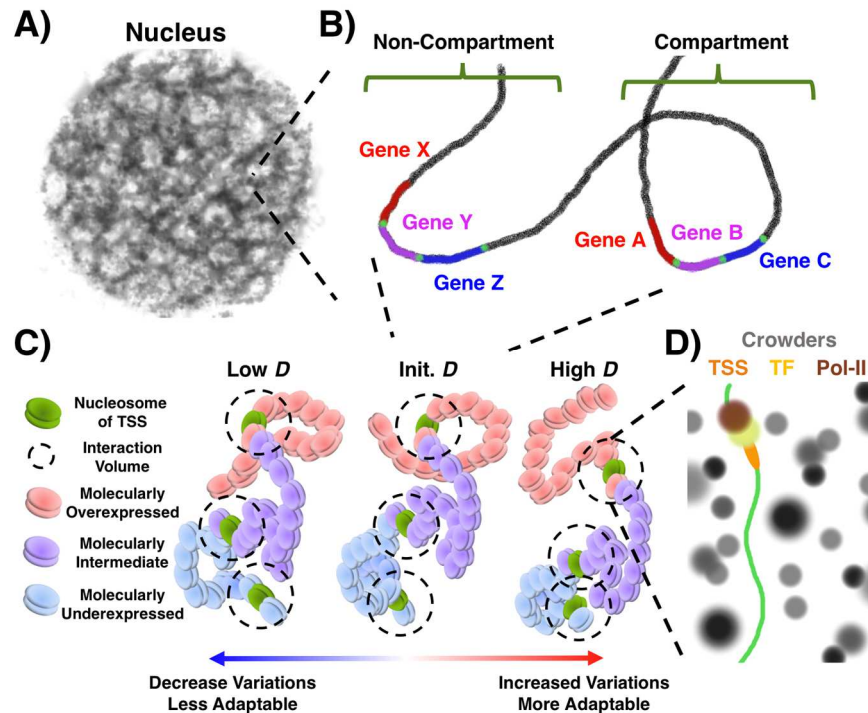
Figure 8.2. *Genomic interactions depend on a complex physical nanoenvironment.* A) One universally shared feature of all genes is the physical nanoenvironment that is determined by the supra-nucleosomal (>10nm) packing density of chromatin within the nucleus. B) While previous work has shown that localizing genes into or out of compartments will influence their expression, both genes within compartments (Genes A-C) and outside of compartments (Genes X-Z) will respond to the physical forces produced by their differential packing density. C) As a consequence, while genes are regulated by distinct molecular characteristics (transcription-factor binding affinity, compartment concentrations of factors, nucleosomal modifications) that predispose them toward a preferred expression state (overexpressed, intermediate, underexpressed) the transcription of these genes into mRNA will also depend on local physical forces. Thus, regardless of the determinant of expression, overexpressed genes (A, X) will differentially respond to local physical organization produced by chromatin packing when compared to intermediately expressed (B, Y) or under expressed (C, Z) genes. To integrate these effects, we consider the power-law scaling of chromatin packing density through fractal dimension, *D*. Increased *D* produces increased variations in chromatin packing density whereas decreased *D* does the opposite. D) Ultimately, the physical geometry of chromatin (scaling) determines accessible surface area as well as local crowding conditions that will influence the chemical reactions governing transcription by altering gene accessibility, molecular mobility of reactant species, and the free energy of the transcriptional reactions.

Owing to this role of physical structure of chromatin as a major regulator of the genomic information space through shaping the physiochemical nanoenvironment, we then apply the predictions in our model to target cancer cells at the level of transcriptional heterogeneity (17, 174). One of the main

challenges in cancer therapy is the innate ability of cells to adaptively sample their genome in order to develop mechanisms of chemotherapeutic evasion (175). To target this process, we employ our model to show that the use of agents that reduce intranuclear variations in chromatin packing density should reduce this transcriptional heterogeneity, thereby limiting the replicative adaptability of cancer cells (17). Using live cell PWS microscopy(38), we test this hypothesis on a handful of compounds to see if they can both reduce both chromatin scaling and transcriptional heterogeneity in cancer cells. We validate this hypothesis in four models of aggressive gynecological tumors and show that these compounds do indeed reduce chromatin scaling and transcriptional heterogeneity, matching model predictions. Hence, we show that global patterns in gene transcription can be controlled by manipulating the physical nanoenvironment within the nucleus. Although we apply the functional consequence of such macrogenomic engineering to cancer, the approach paves the way for the study and treatment of diseases — such as Parkinson's disease, atherosclerosis, and autoimmune disorders — that are governed by the complex interplay of dozens of genes.

8.2. MATERIALS AND METHODS

8.2.1. Cell culture and *in vitro* studies

Leiomyosarcoma (MES-SA and MES-SA.MX2), breast (MDA-MB-231), colon (HCT-116, HT-29) and mouse embryonic fibroblast (MEF) cell lines were purchased from ATCC and maintained in their respective media according to ATCC protocol, supplemented with 10% FBS (ThermoFisher Scientific, Waltham, MA). Ovarian (A2780, A2780.M248, A2780.M273, A2780.M175, and Ovcar8) cell lines were a gift from Dr. Chia-Peng Huang Yang and obtained from the lab of Dr. Elizabeth de Vries at Albert Einstein College of Medicine. Previous work on these cell lines was published in 2015 (Gynecologic Oncology, 2015 Seagle et al). M9K mesothelioma and BxPC3 pancreatic ductal carcinoma cells were obtained from the Northwestern University Developmental Therapeutics core. All cell lines were tested for mycoplasma contamination with Hoechst 33342 within the past year. All experiments were performed on cells from passage 5-20.

Human mesenchymal stem cells (hMSCs, ATCC) were cultured in Dulbecco's Modified Eagle Medium (DMEM), with 4.5 g/L glucose, and supplemented with 10% FBS and 5ml 10x penicillin-streptomycin. For differentiation studies, cells were plated 1.5x10^4 cell/ml in 24 well glass-bottom PWS plates. After 2 days, regular DMEM was switched to hMSC Osteogenic Differentiation Medium (Lonza) containing B-glycerophosphate, ascorbate and dexamethasone. Media was changed every other day and cells were imaged on day 4 post-induction.

Prior to imaging, cells were cultured in 35mm glass bottom petri dishes (Cellvis, Mountain View, CA) until 60-85% confluent. All cells were given 24 hours to re-adhere prior to pharmacological treatment. All chemotherapeutic agents were purchased from Sigma Aldrich, St. Louis, MO. Potential chromatin scaling-reducing agents celecoxib, sulindac sulfide, valproic acid, aspirin, digoxin, UNC0638, UNC1999, EGCG, ginseng, curcumin, 4-phenylbutyrate, simvastatin, mevastatin, resveratrol, and valinomycin were purchased from Sigma Aldrich, St. Louis, MO. Compounds A4 (HDAC inhibitor), A10 (sirtuin), A12 (HMTase), and B2 (HMTase) were obtained from the Northwestern University High Throughput Analysis Laboratory small molecule compound libraries. 9-ING-41 was provided by Actuate Therapeutics, Inc., Ft. Worth, TX.

Chemotherapy treated cells were treated when cells were ~30% confluent for at least 48 hours prior to imaging with paclitaxel (48h, 5 nM), oxaliplatin (48h, 15 μm), 5-fluorouracil (72h, 500 nM), docetaxel (48h, 5nM), or gemcitabine (48h, 50 nM). Putative chromatin scaling-reducing -treated cells were given at least 24 hours to adhere after trypsinization and treated for 30 minutes prior to imaging with either celecoxib (75 μM), sulindac sulfide (100 μM), valproic acid (100 μM), aspirin (1 mM), 9-ING-41 (5 μM), digoxin (100 nM) UNC0638 (1 μM), UNC1999 (1 μM), EGCG (25 nM), ginsenoside RB2 (1 μM), curcumin (25 μM), 4-phenylbutyrate (100 mM), A4 (1 μM), A10 (1 μM), A12 (1 μM), or B12 (1 μM). Each population of treated cells measured by PWS microscopy was compared to an untreated control population of the same cell type that had been plated on the same day with the same seeding density as the treated cells. All cells were maintained and imaged at physiological conditions (5% CO_2 and 37°C) for the duration of the experiment.

Significance was determined using Student's T-test with unpaired, unequal variance on the average nuclear Σ normalized by the average Σ of the accompanying control group between the

conditions indicated in the experiment using Microsoft Excel (Microsoft, Redmond, Washington). Significance threshold for all comparisons was set to 0.05/N to account for multiple comparisons with the respective control groups, where n is the number of groups. For example, significance for chemotherapy treated A2780 cells was 0.05/3 as comparisons were made between control cells and 5FU, paclitaxel, and oxaliplatin treated cells. All structural measurements were performed at least in triplicate and resulting in analysis of the following number of cells: 1877 control, 132 paclitaxel-, 148 5FU-, 102 oxaliplatin-, 132 celecoxib-, 130 digoxin-, 117 VPA-, and 161 sulindac sulfide- treated A2780 cells; 1231 control, 90 paclitaxel-, 100 5 FU-, 85 oxaliplatin-, 72 celecoxib-, 91 digoxin-, 51 VPA-, and 57 sulindac sulfide -treated m248 cells; 309 control M273 cells; 237 control M175 cells; 836 control, 138 docetaxel-, 160 gemcitabine-, 275 celecoxib-, and 342 digoxin-treated MES-SA cells; 558 control, 106 docetaxel-, 103 gemcitabine-, 216 celecoxib-, and 252 digoxin-treated MES-SA.MX2 cells; 324 control, 217 oxaliplatin-, 130 aspirin-, 75 celecoxib-, and 85 9-ING-41-treated HCT116 cells; 264 control, 72 paclitaxel-, 81 5 FU-, 118 oxaliplatin-, 86 celecoxib-, and 82 sulindac sulfide -treated MDA-MB-231 cells; 87 control, 87 EGCG-, and 82 curcumin-treated SW620 cells, 184 control and 109 celecoxib-treated NCI-H1299 cells; 65 control and 61 9-ING-41-treated OvCar8 cells; 100 control and 103 9-ING-41-treated M9K cells; 107 control and 111 9-ING-41-treated AsPC1 cells; 150 control and 163 9-ING-41-treated L3.6pl cells; 157 control, 62 celecoxib-, 54 9-ING-41-, 87 VPA-, and 86 digoxin-treated hMSC cells; 130 control, 44 celecoxib-, 83 VPA-, and 60 digoxin-treated osteoblast cells; and 229 control and 318 4-phenylbutyerate-treated MEF cells. In total, nanoscale measurements were collected from over 12,361 cells.

Each individual experiment consists of 5-10 independent fields of view for analysis with variations in the size and density of cells accounting for the variability in total cell counts for each group. All pseudo-colored live cell PWS images were produced using Matlab® v. 2015b using the Jet color scheme with Σ scaled from 0.01 to 0.065.

8.2.2. Flow cytometry

Apoptotic induction was measured by flow cytometry (BD LSRII at the Northwestern Flow Cytometry Core) using CellEvent® Caspase-3/7 Green Detection Reagent and Hoechst 33342 (all ThermoFisher Scientific, Waltham, MA). In brief, cells were trypsinized and immediately stained with 2 µM

Caspase-3/7 and 4 µM Hoechst 33342 for 30 min. Cells were then centrifuged for 5 minutes at 500xg, washed with PBS, and resuspended in 1 mL of fresh media. Mock-stained cells were collected under the same preparation conditions. Flow cytometry was performed on the following groups of A2780 cells: unstained controls cells, stained control cells, stained 48 hour pac mono-treated cells, stained 48 hour putative chromatin scaling agent- treated cells (sulindac sulfide, valproic acid, celecoxib, and digoxin), and stained 48 hour co-treated pac + putative chromatin scaling agent- cells. 20,000 cells were collected by forward and side scattering channels for each group, with illumination intensities set for all conditions for Hoechst 33342 and Caspase-3/7 staining laser lines to minimize autofluorescence produced from unstained cells. Analysis of flow cytometry was performed using open source Python software package, FlowCytometeryTools 0.4.5. Gates were set for Caspase-3/7 staining and Hoechst 33342 to minimize false positives from unstained cells (<0.1% of total). Percentage of apoptotic cells was assessed as the ratio of Caspase-3/7+ cells divided by the population of Hoechst 33342 positive cells. Errorbars represent uncertainty based on ±10% change in gating thresholds.

8.2.3. Cell counting

Cell count was measured by automatic cell counter (Countess II FL Automated Cell Counter) in lab. In brief, cells were trypsinized and added to the floating cells from the same population that had been previously removed. Cells were either stained with 1uM Image-iT® DEAD™ Green viability stain, 4 µM Hoechst 33342, or 2 µM YO-PRO™-1 Iodide. Cells were then centrifuged for 5 minutes at 1000 rpm, washed with PBS, and resuspended in 1mL of fresh media. Automated cell counting was performed on the following groups of A2780 cells: control cells, 48 hour sulindac sulfide treated cells, 48 hour celecoxib treated cells, 48 hour paclitaxel treated cells, 48 hour sulindac sulfide and paclitaxel co-treated cells, and 48 hour celecoxib and paclitaxel co-treated cells. Analysis was performed using Microsoft Excel.

8.2.4. RNA-seq transcriptional analysis

RNA-sequencing data was obtained from NCBI GEO from data produced by Lee et al. (175) for MDA-MB-231 cells treated with paclitaxel as well as by Li et al (176). for androgen resistant LNCap cells treated with digoxin were aligned to human reference genome hg38 using HISAT2, STRINGTIE, and

BALLGOWN using the methods described in Pertea et. al. (177) Sequencing results for each gene were calculated as fragments per kilobasepair per million reads (FPKM). Variants for the same gene were averaged for each cell. Genes with no expression for all cells were not considered in downstream analysis. GO ontologies available from Mathematica v10 using inbuilt GenomeData® were utilized to classify genes according to the biological process to which they are involved.

8.2.5. Intranetwork transcriptional heterogeneity

FPKM values for each condition were averaged across the five individual replicates for paclitaxel-treated cells and three replicates for digoxin-treated cells which were rounded to the nearest tenth of a decimal. To approximate the change in the genomic information space at the level of intranetwork transcriptional heterogeneity, the entropy, $S = -\sum_k p_k \ln(p_k)$, where p_k is the probability of an observed expression value, was calculated for genes belonging to the listed biological processes. Size of each circle represents the relative number of genes belonging to each process and thickness of connecting lines indicates number of shared genes for each data set (paclitaxel vs. digoxin). Color intensity represents the percentage change in entropy for the paclitaxel or digoxin treated cells in comparison to the untreated controls for each respective group.

8.2.6. Intercellular transcriptional heterogeneity

FPKM values for each cell were rounded to the nearest tenth of a decimal as described above. To approximate the change in the genomic information space at the level of intercellular transcriptional heterogeneity, the variance in expression for each gene was calculated across the 5 replicates of paclitaxel treated cells and the three replicates of the digoxin treated cells. For each process, the median variance was calculated in order to account for the presence of large outliers that could skew the mean. Size of each circle represents the relative number of genes belonging to each process and thickness of connecting lines indicates number of shared genes. Color intensity represents the percentage change in median variance for the paclitaxel or digoxin treated cells in comparison to the untreated controls for each respective group.

In addition, the variance in expression was examined for individual oncogenic genes and chromatin remodeling genes, showing an increased in intercellular transcriptional heterogeneity due to paclitaxel treatment for c-Myc, KLF4, p21, NOTCH2, p53, BRCA1, BAX, BAK1, MXD1, EZH2, Arid1a, Brg1, SUZ12, SUV39H1, BRD8, JARID2, JMJD1C, NuA4 complex (EP400, RUVBL2, MORF4L1, YEATS4), SMYD3, L3MBTL2, RNF20, NCOR1, and GSK3b.

Data availability: RNA-seq data analyzed for this manuscript is available in the NCBI GEO database from *Lee et al.*,2014, accession number SRP040309 and *Li et al*. 2012, accession number GSE35126.

8.3. RESULTS

8.3.1. High-level overview of macromolecular crowding and gene expression molecular dynamics models

In chromatin, chemical reactions such as gene transcription take place in a highly dense and heterogeneous physical nanoenvironment, the consequence of which is not yet fully understood. We developed a predictive model to leverage the effects of this physical nanoenvironment on gene transcription in order to control global patterns in gene expression (Chapter 3). The model achieves this by considering that these chemical reactions depend on (1) the accessibility of the genome (47), (2) the intrinsic molecular characteristics of the gene (binding affinities, local concentration of reactant species, and reaction rates, among others) (76), and (3) the effects of physical interactions on these chemical reactions (76, 166, 178). Notably, the supra-nucleosomal physical organization of chromatin and the associated spatial fluctuations of concentration and the overall accessibility of chromatin have a role in determining the behavior of these chemical reactions. In brief summary, the model predicts that increasing chromatin packing scaling, D, will result in an increase in 1) relative transcriptional diversity, 2) relative intercellular gene expression heterogeneity, and 3) gene network heterogeneity. Thus, macrogenomic regulation can be achieved by targeting chromatin scaling, D.

8.3.2. Chromatin packing density heterogeneity increases with selective resistance to chemotherapy

In this context, carcinogenesis may present a test bed for macrogenomic transcriptional regulation. Indeed, increased chromatin packing-density fluctuations are a near universal hallmark of early oncogenesis. The model described above would suggest that chromatin packing-density heterogeneity could facilitate tumorigenesis by expanding the genomic information space available to neoplastic cells to stabilize otherwise deleterious states (44, 48, 121, 123-127, 139, 179, 180). By extension, this principle would also be expected to apply to the cellular response to cytotoxic chemotherapeutic stress, because increasing intra-network and intercellular transcriptional heterogeneity for functional processes (such as stress response, proliferation, and cell-cycle maintenance) would allow cells to stochastically develop chemotherapeutic resistance in real time (17).

We began by investigating the relationship between chemotherapeutic resistance and chromatin packing density scaling by measuring chromatin packing density heterogeneity (Σ) in two paired cell line models previously described to confer chemotherapeutic resistance by different mechanisms. For a mutationally induced model, we utilized ovarian A2780 WT cells with mutations to the TP53 DNA binding domain: A2780 TP53.m273 (M273), A2780 TP53.m175 (M175), and A2780 TP53.m248 (M248) mutant cells. TP53 mutations are present in over 95% of high-grade serous epithelial ovarian carcinoma (HGS EOC), and missense mutations at these codons, R273, R175, and R248, are the most predominant in HGS EOC patients (181). Additionally, these are gain-of-function mutations result in interaction between TP53 and the cohesin complex protein, Rad21, suggesting they would be associated with alterations in chromatin structure (182). Under normal growth conditions (10% FBS, 5% CO_2), Σ was significantly higher in the M248 subclone than the wild-type TP53 line (A2780), and significantly lower in the M273 subclone than the wild-type (Figure 8.3A, B). When median survival time for HGS EOC patients with these mutations was compared using The Cancer Genome Atlas (TCGA) data, we found a strong correlation between median survival and Σ for each hot-spot mutation (Figure 8.3C). Patients with the M273 mutation had the longest median survival (84.1 months) while patients with the M248 had the worst median survival (33.6 months) and those with the M175 mutation had an intermediate survival (62.1 months). While all of these mutations produce a gain of function interaction with Rad21, their effect on chromatin scaling was inversely associated with the median patient survival duration.
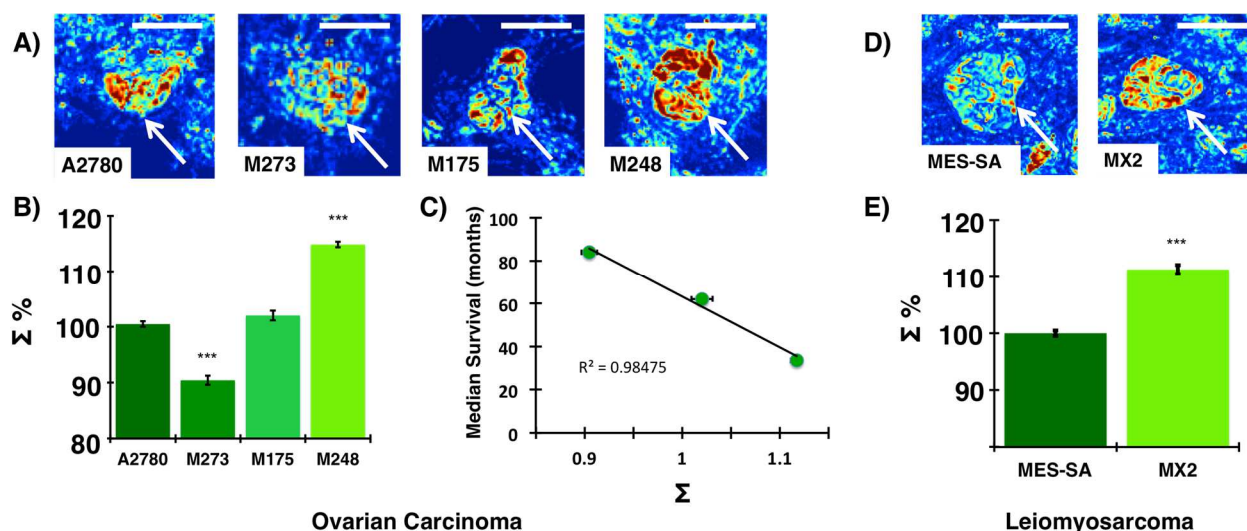
Figure 8.3. *Chromatin packing density heterogeneity increases with selective resistance to chemotherapy.* A) Representative PWS microscopy images of ovarian carcinoma A2780 wild type (WT), and TP53-mutant A2780.M273 (M273), A2780.M175 (M175), and A2780.M248 (M248) cells. Arrows indicate representative nuclei. Scale bars, 10µM. Pseudo-color: heterogeneity of chromatin packing density (Σ). B) Under normal growth conditions, chromatin packing density heterogeneity was decreased in the M273 subclone ($P=2.9 \times 10^{-12}$) and increased in the M248 subclone ($P=1.0 \times 10^{-59}$) relative to the WT A2780 cells. C) Analysis of TCGA data for high-grade serious epithelial ovarian carcinoma patients (N=17, 7, and 13 patients with M273, M175, and M248 mutations respectively) revealed a strong correlation between median survival (as reported to TCGA) and chromatin packing density heterogeneity (Σ) (as measured by PWS) ($R^2=0.98475$). D) Representative PWS microscopy images of leiomyosarcoma MES-SA and mitoxantrone resistant MES-SA/MX2 derivative (MX2) cells. Arrows indicate representative nuclei. Scale bars, 10µM. Pseudo-color: heterogeneity of chromatin packing density (Σ). E) Under normal growth conditions, chromatin packing density heterogeneity was increased in the MX2 chemoresistant subclone ($P=3.1 \times 10^{-30}$) compared to the sensitive MES-SA subclone. Significance was determined using Student's t-test with unpaired, unequal variance on the average nuclear Σ normalized by the average Σ of the accompanying control group between the conditions. Error bars are standard error for *N*=1877 A2780, 309 M273, 237 M175, 1321 M248, 836 MES-SA, and 558 MX2 cells (***P<0.001).

Next, we explored whether inductive resistance in cell line models was likewise associated with increased chromatin scaling. To test this relationship, we utilized a uterine leiomyosarcoma line (MES-SA) with a mitoxantrone resistant MES-SA/MX2 subclone (MX2), which displays constitutive atypical topoisomerase II and MDR1 activity. Similarly to the TP53 mutationally induced resistance models, we observed that Σ was significantly increased in the resistant subclone (MX2) compared to the wild-type MES-SA cell line (Figure 8.3D, E). As these results indicated that increased chromatin scaling correlates with patient prognosis and chemotherapeutic resistance, we hypothesized that chemotherapeutic intervention would confer a selection advantage on the population resulting in the surviving,

chemoevasive population displaying increased chromatin packing density scaling relative to the initial population.

8.3.3. Chemotherapeutic stress increases variations in chromatin packing density

Cytotoxic stressors can be overcome by numerous means and can depend on the capacity of cells to sample their genome to acclimate to the stressful environmental conditions. Since apoptotic and non-apoptotic decisions occur over a concomitant but separated timescale that spans several hours (183), decreasing the accessible genomic information space is expected to shift behavior toward the initial stress-response activity, that is, apoptosis. Conversely, rapidly increasing the information space provides a means for cells to arrive at one of a number of successful evasive mechanisms. Experimentally, intercellular transcriptional heterogeneity has so far been observed as a critical determinant of chemoevasion without a clear mechanistic basis (184). However, as demonstrated by our model, increased scaling of chromatin packing density and the resulting density fluctuations can produce the observed transcriptional heterogeneity.

To test this hypothesis, we treated several cancer cell lines with three classes of chemotherapy drugs: DNA intercalators (oxaliplatin), microtubule assembly inhibitors (paclitaxel and docetaxel), and nucleotide analogs (5-fluoruracil, gemcitabine). In brief, cells were treated with previously reported concentrations of these chemotherapeutics based on which chemotherapies are currently used as standard of care for a given malignancy (181, 185). Specifically, A2780, M248, and MDA-MB-231 cells were treated individually with paclitaxel, oxaliplatin, or 5-FU; leiomyosarcoma cells were treated with docetaxel or gemcitabine; and HCT116 cells were treated with oxaliplatin. Significantly, exposure to cytotoxic chemotherapy resulted in increased Σ within the surviving cells independent of the mechanism of the drug or the model in all cell lines tested (Figure 8.4A, C, D**)**. Additionally, over the course of chemotherapeutic intervention, the average Σ of the population steadily increased, with one potential explanation being those cells with initially higher chromatin scaling are more structurally and transcriptionally diverse and are able to evade chemotherapeutic intervention (Figure 8.4D) (15)**.** To verify that these surviving cells were representative of the non-apoptotic population, we performed live cell Cas3/7 activation staining and observed no significant accumulation of the stain within the analyzed

(adherent) population. To further verify their viability, we performed a 1-hour Brd-U pulse chase on the ovarian parental A2780 and the M248 clone for oxaliplatin, 5-FU, and paclitaxel treated cells. A significant fraction of the adherent cells treated with these chemotherapeutic agents maintained replicative capacity, which indicated that these cells did indeed represent the chemoevasive population. Consequently, these findings confirmed that a convergence between both chromatin packing density scaling and chemoevasion was model and drug independent – with cytotoxic intervention selecting for an increasingly heterogeneous chromatin packing state.
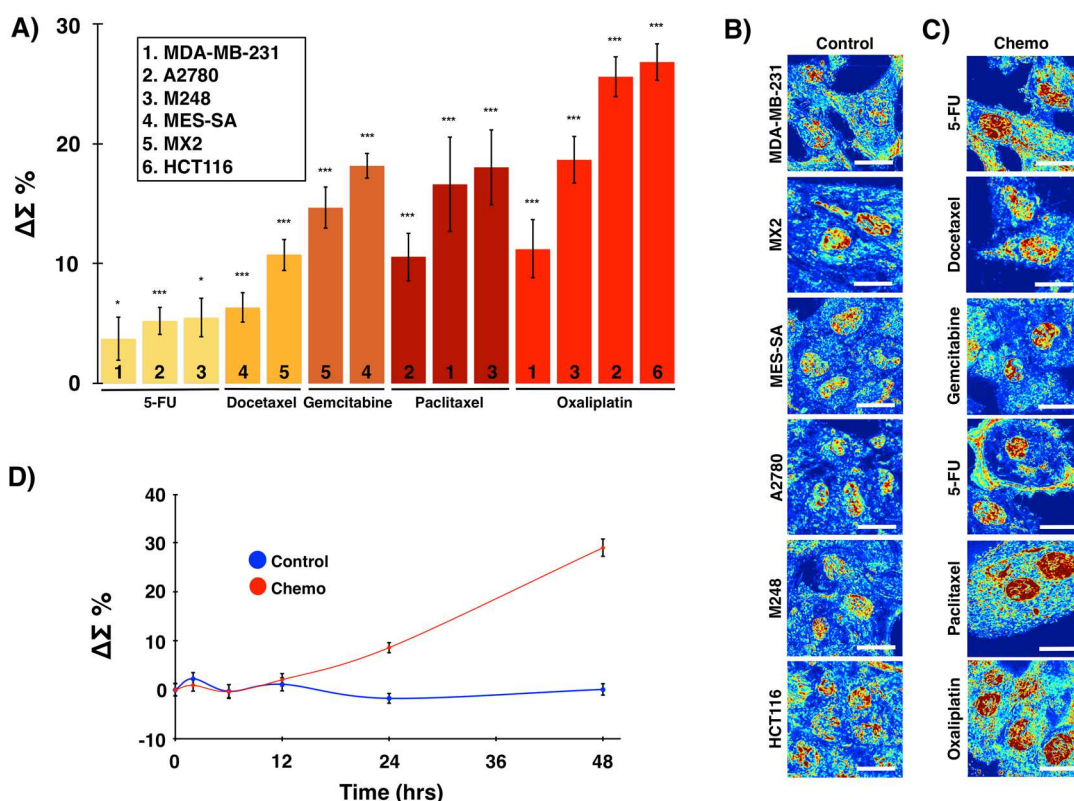
Figure 8.4. *Chromatin packing density heterogeneity increases during chemoevasion.* A) Exposure of cancer cell lines to standard concentrations of chemotherapeutic agents for 48 hours results in increased chromatin packing density heterogeneity of surviving cells. Bars correspond to 5-FU treated MDA-MB-231 ($P=4.9 \times 10^{-2}$), A2780 ($P=2.5 \times 10^{-4}$), and M248 cells ($P=2.2 \times 10^{-3}$); Docetaxel treated MES-SA ($P=2.1 \times 10^{-6}$) and MX2 ($P=6.6 \times 10^{-12}$) cells; Gemcitabine treated MX2 ($P=3.7 \times 10^{-13}$) and MES-SA ($P=1.1 \times 10^{-19}$) cells; Paclitaxel treated A2780 ($P=2.0 \times 10^{-7}$), MDA-MB-231 ($P=1.5 \times 10^{-4}$), and M248 ($P=6.6 \times 10^{-7}$) cells; and Oxaliplatin treated MDA-MB-231 ($P=5.7 \times 10^{-5}$), M248 ($P=5.0 \times 10^{-15}$), A2780 ($P=2.8 \times 10^{-28}$), and HCT116 ($P=6.6 \times 10^{-39}$) cells. B&C) Representative PWS microscopy images of control and chemoevasive cells for each chemotherapy tested. Scale bars, 20µM. Pseudocolor: heterogeneity of chromatin packing density (Σ). Control MDA-MB-231, MX2, MES-SA, A2780, M248, and HCT116 cells (B) were treated for 48 hours with 5-FU, Docetaxel, Gemcitabine, 5-FU, Paclitaxel, and Oxaliplatin respectively for 48 hours (C) as representatives of all cell line and chemotherapy combinations. D)

Average population chromatin packing density heterogeneity of surviving cells steadily increases over the course of chemotherapeutic intervention with oxaliplatin in HCT116 cells.   Significance was determined using Student's t-test with unpaired, unequal variance on the average nuclear Σ normalized by the Σ of the accompanying control group between the conditions. Error bars are standard error for N=81 MDA-MB-231, 148 A2780, and 100 M248 cells treated with 5-FU; N=160 MES-SA and 106 MX2 cells treated with docetaxel; N=138 MES-SA and 103 MX2 cells treated with gemcitabine; N=132 A2780, 72 MDA-MB-231, and 90 M248 cells treated with paclitaxel; and N=118 MDA-MB-231, 85 M248, 102 A2780, and 217 HCT116 cells treated with oxaliplatin (***$P<0.001$, *$P<0.05$).

8.3.4. Pharmacological agents can rapidly decrease the spatial variations in chromatin packing density in cancer cells

By taking advantage of the knowledge that chromatin scaling is indeed predictably and directly coupled to the chemotherapeutic response, we explored whether compounds (see section 3.3.5) that can rapidly (<30 min) reduce chromatin packing-density fluctuations would act as adjuvant agents for chemotherapeutic efficacy. This short time point was chosen to avoid potential confounding from protein translation on chromatin structure. To test the macrogenomic engineering approach, we selected two compounds that act on biological processes that were transformed by paclitaxel treatment: celecoxib (stress response) and digoxin (ion homeostasis). Utilizing live cell PWS microscopy, we measured the transformation in chromatin-scaling within 30 minutes for A2780, A2780.M248 (M248), MES-SA, and MES-SA.MX2 (MX2) cells treated with either digoxin or celecoxib. We focused on uterine leiomyosarcoma and ovarian carcinoma, as we had both a resistant and sensitive subclone for each model. Notably, each cell-type's response to these compounds varied, but a substantive response was identifiable (Figure 8.5A-D).
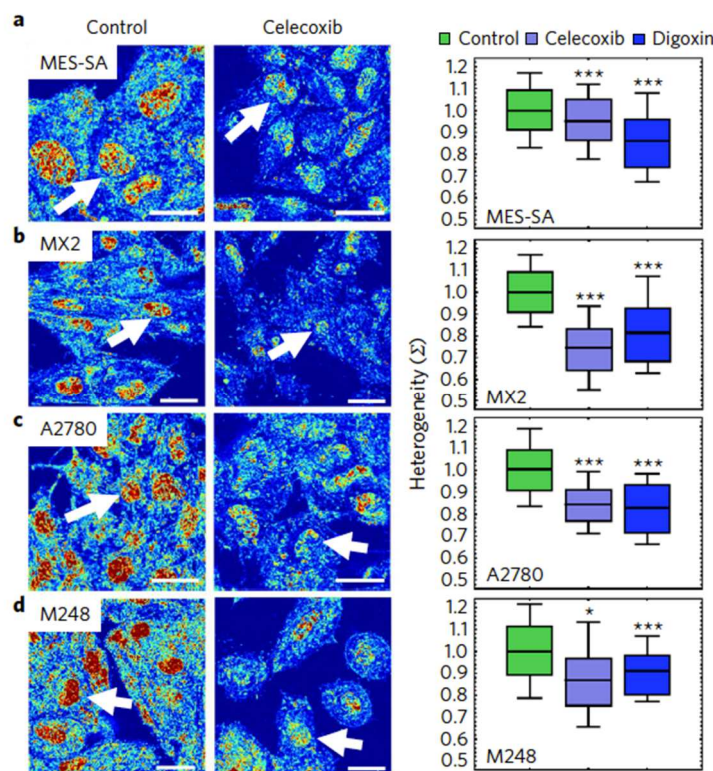
Figure 8.5. *Pharmacological agents rapidly decrease the spatial variations in chromatin packing density in cancer cells.* A-D) Representative PWS images (left) and quantification (right) of the effects of various agents on the variations of chromatin packing density for MES-SA (A), MES-SA.MX2 (MX2) (B), A2780 (C), and A2780.M248 (M248) (D) cells. Notably, variations of chromatin packing density for each cell line model have a differential response to pharmacological agents celecoxib ($p=3.9\times10^{-34}$, 1.5×10^{-53}, 1.5×10^{-30}, and 1.3×10^{-3} for MES-SA, MX2, A2780, and M248 cells respectively) and digoxin ($p=2.7\times10^{-8}$, 7.6×10^{-69}, 3.1×10^{-36}, and 6.2×10^{-9} for MES-SA, MX2, A2780, and M248 cells respectively). Significance was determined using Student's t-test with unpaired, unequal variance on the average nuclear Σ normalized by the average Σ of the accompanying control group between the conditions. Box represents the 25-75% range and whisker represents the 10-90% range of values around the mean for N=(836 control, 275 celecoxib, and 342 digoxin) MES-SA cells, N=(558 control, 216 celecoxib, and 252 digoxin) MX2 cells, N=(823 control, 132 celecoxib, and 130 digoxin) A2780 cells, and N=(525 control, 36 celecoxib, and 91 digoxin) M248 cells. Scale bars are 15μm. Pseudo-color: heterogeneity of chromatin packing density (Σ). Arrows: cell nuclei. (p-value <0.001 ***, p-value <0.05 *).

We additionally compared the effects of multiple compounds with similar molecular mechanisms of action (NSAIDs, histone deacetylase inhibitors (HDACi), and histone methyltransferase (HMTase) inhibitors). It is significant to note here that not all compounds from the same class of drugs act on chromatin scaling: while celecoxib and sulindac are both NSAIDs, celecoxib substantially reduced Σ while sulindac sulfide did not (Appendix C1). Additionally, celecoxib had a demonstrated remodeling effect even in the COX-2 deficient HCT-116 cells at these short timescales (Appendix C2). Likewise, aspirin, another

NSAID, displayed a significant but relatively attenuated decrease of Σ within 30min of treatment in HCT-116 cells when compared to celecoxib. Other classes of compounds, including HDACi, displayed similarly divergent results: VPA significantly reduced Σ while 4-phenylbutyrate did not despite both compounds being classified as HDAC inhibitors. Finally, some known chromatin remodelers such as HTMase inhibitors UNC0638 and UNC1999 displayed no ability to affect Σ.

We were additionally interested to see if we could identify compounds that significantly reduced scaling in cancer cells but produced less than a <5% change in Σ in nontumorigenic cell lines. To identify which of these compounds with a large effect on cancer cells would minimally influence normal cells, we selected the four most effective compounds in terms of reducing chromatin scaling – VPA, digoxin, celecoxib, and 9-ING-41 – and tested them on a noncancerous cell line model. When administered to osteoblasts for the same duration and at the same concentration as used with great modulatory efficacy in cancer cells, VPA and digoxin decreased Σ by >5% (Appendix C3). Conversely, Celecoxib and 9-ING-41 met our screening criteria as they had a very minimal effect on Σ in osteoblasts as well as in human mesenchymal stem cells (Appendix C3).

8.3.5. Regulation of chromatin packing density scaling modulates transcriptional heterogeneity

In view of the differential response between compounds that reduce chromatin scaling and chemotherapeutic agents at the level of variations in chromatin packing-density scaling, we next tested if these observations would extend into transcriptional heterogeneity. Critically, analysis of single-cell RNA-seq data of MDA-MB-231 cells treated with paclitaxel in comparison to control cells (175) shows the expected shift towards increased intercellular transcriptional heterogeneity, as well as towards intra-network transcriptional heterogeneity, owing to chemotherapeutic intervention. The shift affects numerous biological processes, as it includes genes involved in proliferation, apoptosis, oxidation/reduction, ion transport, and nucleosome assembly (Figure 8.6A-C). Furthermore, analysis of RNA-seq data of digoxin-treated cells shows that decreases in the chromatin packing-density fluctuations through pharmacological agents likewise correlated with decreases in intercellular and intra-network transcriptional heterogeneity (Figure 8.6A-C). This differential response between chemotherapeutic agents (taxols) increasing scaling and chromatin scaling-modulatory agents (digoxin) decreasing scaling (Figure 8.6A) paired with the

expected changes to gene expression (Figure 8.6B, C) supports our finding that controlling chromatin packing-density scaling can be used to modulate the genomic information space.
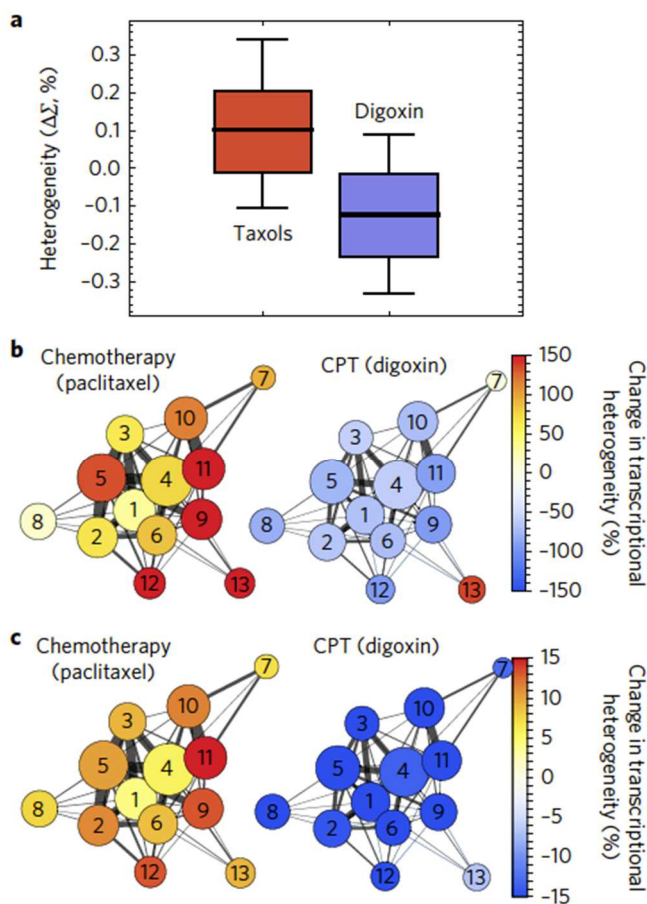
Figure 8.6. *Regulation of chromatin packing-density scaling modulates transcriptional heterogeneity.* A) Comparison of the alterations in the variations of chromatin packing density due to taxol treatment (paclitaxel or docetaxel) in contrast to chromatin scaling-reducing agent digoxin for five cell line models (A2780, M248, MDA-MB-231, MES-SA, MX2). Notably, chemotherapeutic intervention produces increased variations in chromatin packing density whereas a chromatin scaling-reducing agent (digoxin) decreases variations in chromatin packing density. Box represents the 25-75% range and whisker represents the 10-90% range of values around the mean for N=401 taxol treated cells (132 A2780, 25 M248, 102 MES-SA, 106 MX2, and 36 MDA-MB-231) and N=815 digoxin treated cells (130 A2780, 91 M248, 342 MES-SA, and 252 MX2). B&C) As expected, intercellular (B) and intra-network (C) transcriptional heterogeneity increases in cells treated with the chemotherapy agent and decreases in cells treated with the CPT agent for critical biological processes including (1) cell cycle, (2) apoptosis, (3) proliferation, (4) transcription, (5) signaling, (6) differentiation, (7) glycolysis, (8) translation, (9) ion transport, (10) metabolism, (11) oxidation/reduction, (12) stress response, and (13) nucleosome assembly. Circle size represents the number of each genes belonging to a functional network/process and thickness the number of shared genes. Color intensity represents the % change in transcriptional heterogeneity in paclitaxel treated vs. controls and in digoxin treated cells vs. control (see *RNA-Seq transcriptional analysis*, *Intranetwork transcriptional heterogeneity*, and *Intercellular transcriptional heterogeneity* in the methods section for calculation.) Gene network analysis was performed by Luay Almassalha, Backman Lab, Northwestern University.

8.4. DISCUSSION

Supra-nucleosomal chromatin can have profound effects on gene expression by acting on accessibility, mobility, and the binding affinities between reactant molecules. Previous investigations of the interaction between molecular behavior and physical organization have focused on the regulators of local compaction/decompaction in the context of the expression of individual genes (170, 171). Whereas previous work has demonstrated the role of genetic modifications, histone post-translational modifications and genomic compartments in the regulation of the expression of individual genes, the role of the physical environment within the nucleus on the broad regulation of gene expression has not been previously explored. Here, we have described a physiochemical framework that maps the collective behavior of multiple genes simultaneously on the basis of chromatin's physical nanoenvironment (Figure 8.2A-D). These capabilities are derived from experimental evidence indicating that chromatin is the dominant crowder within the nucleus. In this context, modulating the packing-density scaling of chromatin is one mechanism to shape the nuclear physical nanoenvironment and alter global patterns in gene expression. In particular, we have demonstrated that macrogenomic engineering can control the transcriptional activity of many genes simultaneously and can be applied to the selection of adjuvant compounds to increase the efficacy of chemotherapeutic agents *in vitro*. Physicochemical modulation of the chromatin nanoenvironment influences patterns in gene expression owing to the sensitivity of genes to changes in the local physical conditions.

Although previous work investigating supra-nucleosomal organization has shown that gene expression depends on gene localization into a compartment or outside of it, we have shown that both genes within compartments and those outside of them respond to the physical forces produced by the physical nanoenvironment (Figure 8.2B, C). We integrated Brownian dynamics and Monte Carlo simulations of the chemical reactions governing transcription with analytical predictions of the change in global accessible surface area and of the variations in local density of chromatin packing. The combined model allows the analytical prediction of transcriptional consequences of changes in the power-law scaling of chromatin packing density. Critically, the results from the model are in strong agreement with experimental results obtained through a combination of microarray measurements of gene expression and of live-cell PWS microscopy of the cell's physical structure. The model appears to be best equipped

to explain collective patterns in gene expression, and ultimately becomes the dominant predictor of expression patterns for larger groups of genes (15).

A major functional consequence of this asymmetric response is the transformation of the genomic information space, as the level of intercellular transcriptional heterogeneity, genomic divergence, and intra-network transcriptional heterogeneity relate directly to chromatin packing-density scaling (Chapter 2) (15). As this intercellular transcriptional heterogeneity is a major factor in chemotherapeutic resistance, we predicted that (1) cytotoxic chemotherapeutic intervention would produce increased variations in chromatin packing density and (2) agents could be selected to reverse this effect in cancer cells. As predicted, treatment with cytotoxic chemotherapeutic compounds selected for cells with increased chromatin packing-density heterogeneity independent of the cell line model (Ovarian, Breast, and Sarcoma) and of the mechanism of the chemotherapeutic agent (DNA intercalators, microtubule assembly inhibitors, and DNA analogs). Furthermore, the transformation of chromatin towards increased packing-density fluctuations corresponded with increased intra-network and intercellular transcriptional heterogeneity as demonstrated by single-cell RNA sequencing. As these findings are in strong agreement with our model predictions, we therefore began to identify compounds that could reverse this process (decrease chromatin packing-density heterogeneity) at short time scales.

We tested this hypothesis by examining the effects of compounds predicted to act on chromatin scaling based on the model of chromatin polymer that act on processes that demonstrated increased intercellular and intra-network transcriptional heterogeneity during paclitaxel treatment: stress response (celecoxib) and ion homeostasis (digoxin). Both of these compounds have some anti-neoplastic inhibitory effects, but our results suggest that they also modulate chromatin packing density. Further studies will undoubtedly need to sort out chromatin-mediated effects from signaling or growth inhibitory pathways in terms of the long-term and potentially therapeutic effects of these compounds on cancer cells. However, the robust agreement between the observed changes in gene expression and the predictions of our model, the effect of chemotherapeutics on transcriptional and chromatin packing-density heterogeneity, and the effects of chromatin scaling-reducing agents on decreasing both transcriptional and chromatin packing-density heterogeneities support the overall potential of macrogenomic engineering for modulating chromatin packing density scaling.

8.5. CONCLUSION

We have shown that macrogenomic engineering can predictably modulate global patterns in gene expression by controlling the physiochemical environment within the cell's nucleus. Whole-transcriptome manipulation based on the control of the physiochemical nanoenvironment of chromatin should be widely applicable to address many illnesses, including cancer, inflammatory disorders and auto-immune diseases. Macrogenomic engineering could complement gene-editing techniques: whereas the latter work at the level of the linear genetic code and thus target individual genes, the regulation of chromatin packing density affects global patterns of gene expression.

Chapter 9: Discussion, conclusion, and future directions

9.1. SUMMARY

Despite the fact that chromatin organization is essential in governing key cellular process like transcription and proliferation, there are very few methods to interrogate exactly how chromatin structure governs function between about 20 and 350 nm. Here we present a technique, Partial Wave Spectroscopic (PWS) microscopy, that gives us the capability to study such structures in label free, live cells in real time. PWS (i) provides nanoscale sensitivity to structures between 20 and 350 nm, (ii) uses label-free contrast to capture nanoscopic information, (iii) is nonperturbing to biological samples by using low-power illumination and label-free contrast, (iv) quantifies the cellular nanoarchitecture, and (v) rapidly captures the temporal evolution of nanoscale structures, providing contrast in multiple cells in seconds. With this technique we show the structure–function relationship between critical processes and chromatin structure, including DNA repair, replication, and transcription. With this technique, we determined that live-cell DNA-binding dyes, such as Hoechst 33342, cause rapid destruction of the higher-order chromatin structure at timescales (seconds) not previously recognized and showed that mitochondrial function is intimately related to chromatin structure.

Given the tightly-paired relationship between chromatin and transcription, we next sought to define how chromatin scaling influences not the transcription of individual genes, but how it regulates global patterns of gene expression. We demonstrated, both computationally and experimentally, that physico-chemical regulation of chromatin packing scaling can be used to influence and alter transcriptional diversity, intercellular heterogeneity, and gene network heterogeneity. The ability to influence such global patterns of transcription implies the ability to target chromatin scaling as a means to regulate critical cellular processes and the overall plasticity of cells as they respond to extracellular conditions.

After using PWS to define the relationship between chromatin scaling and critical processes such as DNA repair, replication, transcription, cell cycle, and proliferation, we then demonstrated the driving force of chromatin scaling and its regulation in the context of cardiovascular inflammation, stem cell plasticity, and carcinogenesis and chemoevasion and suggested that the physico-chemical regulation of

chromatin packing scaling, as measured by PWS, could be used in the context of these cellular states: Within the context of cardiovascular inflammation, we focused on Sirt1, a histone deacetylase, to explain its role in regulating chromatin scaling to protect against inflammation. With regard to stem cell plasticity, we demonstrated that genome structure and compartmentalization could indeed be affected through pharmacological and morphological means to result in functional changes in stem cell differentiation. Within the context of cancer, we used PWS to demonstrate the near-universal link between nanoscopic changes in chromatin scaling in early tumorigenesis, which appear to be a common denominator of multiple molecular carcinogenesis pathways. Furthermore, we have shown that chromatin scaling increases during chemoevasion, that pharmacological agents target at chromatin scaling can rapidly reduce the spatial variations in chromatin scaling in cancer cells, and we have confirmed that this regulation of chromatin scaling in turn modulates transcriptional heterogeneity. In summary, we have developed a powerful tool, live cell PWS microscopy, to interrogate the relationship between chromatin structure and function and have shown that controlling the physicochemical environment within the cell's nucleus to alter chromatin scaling can predictably modulate global patterns in gene expression. This whole-transcriptome manipulation based on the control of the physiochemical nanoenvironment of chromatin has implications in essentially any disease state and may allow for the ability to control the overall behavior of biological systems.

9.2. FUTURE DIRECTIONS AND EMERGING QUESTIONS

To date, we have identified several compounds that alter global chromatin scaling to some degree. Our approach so far has as outlined in Chapter 2: within the context of the chromatin polymer model, we selected compounds for testing that could regulate chromatin polymer packing density scaling either by using ATP and molecular motors to create chromatin loops or by targeting the natural conformation of a chromatin chain within the nucleus as influenced both by chromatin self-interactions and chromatin-nucleoplasm interactions. While most of the compounds we initially screened have activity on numerous molecular pathways and have been shown to be antineoplastic in the lab or clinical setting, our main focus was on identifying the contribution of chromatin scaling to this antineoplastic activity.

However, we would ideally like to develop more efficient chromatin modulators, and there are several approaches we have begun to take to discover and optimize such compounds.

The first approach is high-throughput screening with PWS of the effects of small molecule compounds on chromatin scaling of cancer cells. The High Throughput Analysis Laboratory at Northwestern University has a repository of nearly 100,000 small molecules, and we have been mining 96-well plates from their kinase inhibitor-like library (chemically synthesized compounds with similar structure to other kinase inhibitors but without any actual known mechanism of action) and their clinical trial compound library (compounds with some known mechanism of action with variety of potential applications but are not FDA-approved) for compounds with such effects. As we are looking for compounds with maximal reduction potential in terms of chromatin scaling, only compounds whose treatment results in a >10% reduction in scaling will be selected to proceed with further testing (viability assays, synergy with chemotherapy, etc.). To date, we have screened over 144 compounds and have not found any hits. Although the end goal is to find a compound hit, it is actually reassuring that the hit rate is so low. If every compound tested were to have dramatic effects on chromatin scaling and potentially transcriptional regulation, it would be difficult to understand how our cells are able to maintain a general homeostasis.

The second approach is the use of low frequency electromagnetic radiation (LFEMR) to induce changes in chromatin scaling. Prior studies have shown LFEMR to activate Ca^{2+} voltage gated channels through modulation of the intercellular Ca^{2+} concentration(65, 186, 187). LFEMR has also been shown to affect Na+/K+-channels and mitochondrial membrane potential in a frequency dependent manner(188). In turn, mitochondrial function has a direct effect on gene transcription in general and chromatin structure in particular. Our lab has previously shown that a decrease in the mitochondrial membrane potential results in a rapid decrease in chromatin packing(38). Given our previous selection of compounds based on their ability to modulate the physico-chemical nanoenvironment through ion concentration and the subsequent effects on chromatin self-interactions, we hypothesized that LFEMR could have a similar effect. To date, we have tested a variety of frequencies ranging from 0-1000 Hz on human astrocyte (NHA) cells and seen a range of chromatin scaling responses based on the frequency tested (Figure 9.1). Our studies will continue by testing similar frequency ranges on cancer cells and quantifying changes in chromatin

scaling, synergy with chemotherapy, as well as mechanistic metrics such as transcriptional alterations, changes in intercellular and intranuclear ion distribution due to LFEMR. Additionally, we will study the dynamics of this modulation, in particular the duration of the observed effects on chromatin scaling.
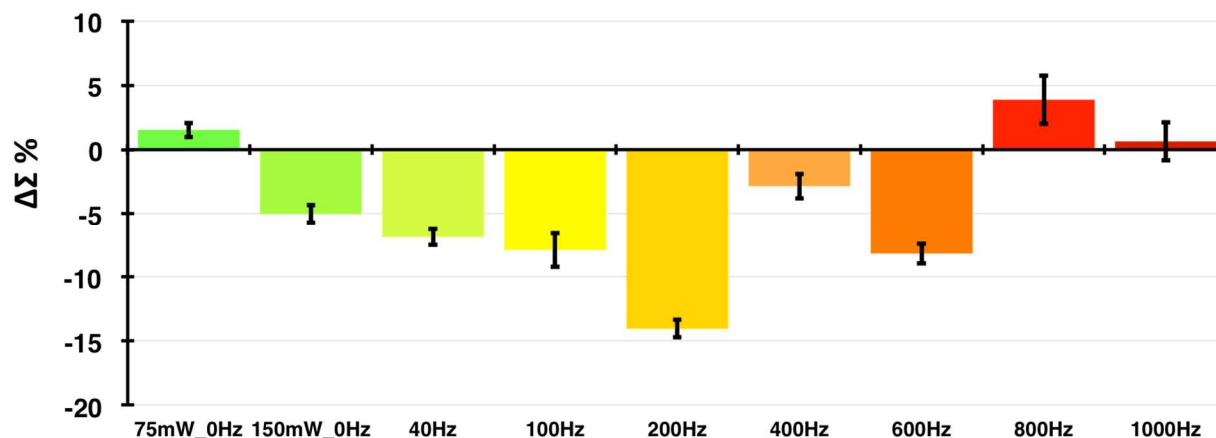
Figure 9.1. *Effects of LFEMR stimulation on chromatin heterogeneity*. NHA cells (normal human astrocytes) were exposed to laser light under two conditions; continuous, unmodulated light and modulated light. Under continuous, unmodulated light conditions, cells were exposed to 532nm laser light for 2 hours at a power of 75mW or 150nW within a 3.5mm-diameter spot area. For cells exposed to modulated light, laser light was modulated with an optical chopper to produce a 40, 100, 200, 400, 600, 800, or 1000Hz exposure while the power was kept the same as in the unmodulated exposure. Live cells were imaged with PWS microscopy before and after exposure to unmodulated or modulated light (at 0 and 120 minute time points) to quantify the percent change in chromatin packing heterogeneity (%ΔΣ). While most frequencies did not significantly or drastically change chromatin heterogeneity, cells exposed to 200Hz modulated light did experience a substantial effect in terms of reduction of chromatin scaling. These findings suggest light modulated at 200Hz significantly decreases chromatin scaling in non-cancerous, human cells *in vitro*. LFEMR experiments were performed by Andrew Stawarz, Backman Lab, Northwestern University.

The third approach is to test the effect of naturally secreted myokines from mouse muscle cells that have been electrically stimulated. The rationale for this approach comes from the empirical evidence that exercise is advantageous to health but also that cancer patients who exercise regularly tend to respond better to chemotherapy (164, 189-192). We have used a C-Pace EM system to both stimulate differentiated C2C12 mouse myoblast cells in order to generate bulk "myokine media" that is then used to treat cancer cells as a chromatin modulating agent. We have optimized the conditions for producing the myokine media with regard to voltage, duration of stimulation, and media concentration, and have seen a dramatic effect in the reduction of chromatin scaling of cancer cells with this optimized formula (Figure 9.2). Immediate plans are to fractionate this bulk myokine media with size exclusion columns and mass spectrometry to identify the individual myokine profile of this bulk media. The bulk media likely has a

combination of more and less potent myokines in terms of their ability to reduce chromatin scaling, so we

will systematically and combinatorially test the effects of these products on the cancer cells.
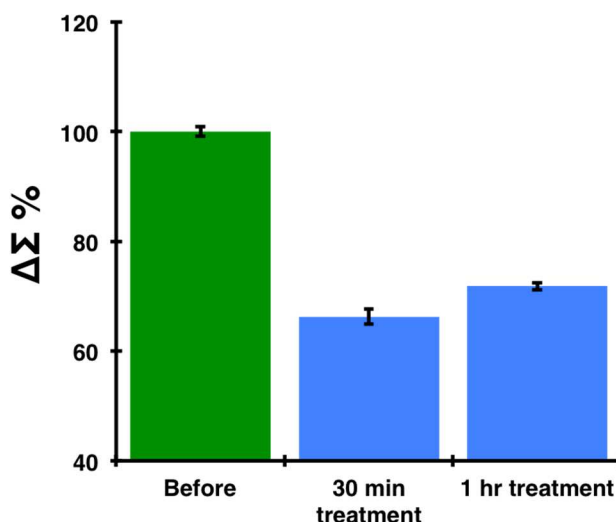
Figure 9.2. *Chromatin heterogeneity decreases with stimulated myokine media treatment*. Chromatin heterogeneity was significantly decreased at 30 minutes and 1 hour in HCT116 colon cancer cells treated with media from stimulated C2C12 mouse myokine cells. C2C12 cells were stimulated at 35V for 7 hours in 1 mL of growth media. At the end of stimulation, that media was then used to treat the HCT116 cells. Significance was determined using Student's t-test with unpaired, unequal variance on the average nuclear Σ normalized by the average Σ of the accompanying control group between the conditions. Under normal growth conditions, chromatin heterogeneity was decreased in HCT116 cells by 32% at 30 minutes post-treatment and 29% 1 hour post-treatment compared to control HCT116 cells exposed to media from un-stimulated C2C12 cells. Error bars are standard error.

Future directions will also aim to apply strategies of chromatin scaling regulation to therapeutics

for these and other diseased states. By having the ability to control the overall ability of any biological

system through the targeting of chromatin scaling, we can potentially develop novel physicochemical

strategies to help control cell fate and behavior to reverse the effects of aging and other diseases.

REFERENCES

1.   Cremer T*, et al.* (2000) Chromosome territories, interchromatin domain compartment, and nuclear matrix: an integrated view of the functional nuclear architecture. *Crit Rev Eukaryot Gene Expr* 10(2):179-212.
2.   Mirny LA (2011) The fractal globule as a model of chromatin architecture in the cell. *Chromosome Res* 19(1):37-51.
3.   Boettiger AN*, et al.* (2016) Super-resolution imaging reveals distinct chromatin folding for different epigenetic states. *Nature* 529(7586):418-422.
4.   Bedin V, Adam RL, de Sa BC, Landman G, & Metze K (2010) Fractal dimension of chromatin is an independent prognostic factor for survival in melanoma. *BMC Cancer* 10:260.
5.   Bancaud A, Lavelle C, Huet S, & Ellenberg J (2012) A fractal model for nuclear organization: current evidence and biological implications. *Nucleic Acids Res* 40(18):8783-8792.
6.   Lebedev DV*, et al.* (2005) Fractal nature of chromatin organization in interphase chicken erythrocyte nuclei: DNA structure exhibits biphasic fractal properties. *FEBS Lett* 579(6):1465-1468.
7.   Fudenberg G, Getz G, Meyerson M, & Mirny LA (2011) High order chromatin architecture shapes the landscape of chromosomal alterations in cancer. *Nat Biotechnol* 29(12):1109-1113.
8.   Dekker J, Marti-Renom MA, & Mirny LA (2013) Exploring the three-dimensional organization of genomes: interpreting chromatin interaction data. *Nat Rev Genet* 14(6):390-403.
9.   Lieberman-Aiden E*, et al.* (2009) Comprehensive mapping of long-range interactions reveals folding principles of the human genome. *Science* 326(5950):289-293.
10. Botta M, Haider S, Leung IX, Lio P, & Mozziconacci J (2010) Intra- and inter-chromosomal interactions correlate with CTCF binding genome wide. *Mol Syst Biol* 6:426.
11. Li L*, et al.* (2015) Widespread rearrangement of 3D chromatin organization underlies polycomb-mediated stress-induced silencing. *Mol Cell* 58(2):216-231.
12. Hnisz D*, et al.* (2016) Activation of proto-oncogenes by disruption of chromosome neighborhoods. *Science* 351(6280):1454-1458.
13. Ou HD*, et al.* (2017) ChromEMT: Visualizing 3D chromatin structure and compaction in interphase and mitotic cells. *Science* 357(6349).
14. Schwarzer W*, et al.* (2017) Two independent modes of chromatin organization revealed by cohesin removal. *Nature* 551(7678):51-56.
15. Almassalha LM, Bauer, G.M., Wu, W. *et al.* (2017) Macrogenomic engineering via modulation of the scaling of chromatin packing density. *Nature Biomedical Engineering* 1:902-913.
16. Almassalha LM*, et al.* (2017) The Global Relationship between Chromatin Physical Topology, Fractal Structure, and Gene Expression. *Sci Rep-Uk* 7.
17. Almassalha LM*, et al.* (2016) The Greater Genomic Landscape: The Heterogeneous Evolution of Cancer. *Cancer Res* 76(19):5605-5609.
18. Chandler JE*, et al.* (2016) Colocalization of cellular nanostructure using confocal fluorescence and partial wave spectroscopy. *J Biophotonics*.
19. Finn AV*, et al.* (2007) Vascular responses to drug eluting stents: importance of delayed healing. *Arterioscler Thromb Vasc Biol* 27(7):1500-1510.
20. Li G, Chen SJ, Oparil S, Chen YF, & Thompson JA (2000) Direct in vivo evidence demonstrating neointimal migration of adventitial fibroblasts after balloon injury of rat carotid arteries. *Circulation* 101(12):1362-1365.
21. Frosen J, Calderon-Ramirez L, Hayry P, & Myllarniemi M (2001) Quantitation of cell migration in a rat carotid artery balloon injury model. Indications for a perivascular origin of the neointimal cells. *Cardiovasc Drugs Ther* 15(5):437-444.
22. Shi Y*, et al.* (1996) Adventitial myofibroblasts contribute to neointimal formation in injured porcine coronary arteries. *Circulation* 94(7):1655-1664.
23. Chen Y*, et al.* (2013) Adventitial stem cells in vein grafts display multilineage potential that contributes to neointimal formation. *Arterioscler Thromb Vasc Biol* 33(8):1844-1851.
24. Passman JN*, et al.* (2008) A sonic hedgehog signaling domain in the arterial adventitia supports resident Sca1+ smooth muscle progenitor cells. *Proc Natl Acad Sci U S A* 105(27):9349-9354.

25. Dourron HM, *et al.* (2005) Perivascular gene transfer of NADPH oxidase inhibitor suppresses angioplasty-induced neointimal proliferation of rat carotid artery. *Am J Physiol Heart Circ Physiol* 288(2):H946-953.
26. Li XD, Chen J, Ruan CC, Zhu DL, & Gao PJ (2012) Vascular endothelial growth factor-induced osteopontin expression mediates vascular inflammation and neointima formation via Flt-1 in adventitial fibroblasts. *Arterioscler Thromb Vasc Biol* 32(9):2250-2258.
27. Liu J, Ormsby A, Oja-Tebbe N, & Pagano PJ (2004) Gene transfer of NAD(P)H oxidase inhibitor to the vascular adventitia attenuates medial smooth muscle hypertrophy. *Circ Res* 95(6):587-594.
28. Mallawaarachchi CM, Weissberg PL, & Siow RC (2005) Smad7 gene transfer attenuates adventitial cell migration and vascular remodeling after balloon injury. *Arterioscler Thromb Vasc Biol* 25(7):1383-1387.
29. Mallawaarachchi CM, Weissberg PL, & Siow RC (2006) Antagonism of platelet-derived growth factor by perivascular gene transfer attenuates adventitial cell migration after vascular injury: new tricks for old dogs? *FASEB J* 20(10):1686-1688.
30. Mazor T, Pankov A, Song JS, & Costello JF (2016) Intratumoral Heterogeneity of the Epigenome. *Cancer Cell* 29(4):440-451.
31. Hill VK, Kim JS, & Waldman T (2016) Cohesin mutations in human cancer. *Biochim Biophys Acta* 1866(1):1-11.
32. Johnstone RW (2002) Histone-deacetylase inhibitors: novel drugs for the treatment of cancer. *Nat Rev Drug Discov* 1(4):287-299.
33. Marquez-Vilendrer SB, Thompson K, Lu L, & Reisman D (2016) Mechanism of BRG1 silencing in primary cancers. *Oncotarget*.
34. Nebbioso A, Carafa V, Benedetti R, & Altucci L (2012) Trials with 'epigenetic' drugs: an update. *Mol Oncol* 6(6):657-682.
35. Nervi C, De Marinis E, & Codacci-Pisanelli G (2015) Epigenetic treatment of solid tumours: a review of clinical trials. *Clin Epigenetics* 7:127.
36. McCabe MT & Creasy CL (2014) EZH2 as a potential target in cancer therapy. *Epigenomics* 6(3):341-351.
37. McCabe MT, *et al.* (2012) EZH2 inhibition as a therapeutic strategy for lymphoma with EZH2-activating mutations. *Nature* 492(7427):108-112.
38. Almassalha LM, *et al.* (2016) Label-free imaging of the native, living cellular nanoarchitecture using partial-wave spectroscopic microscopy. *Proc Natl Acad Sci U S A* 113(42):E6372-E6381.
39. Klar TA, Jakobs S, Dyba M, Egner A, & Hell SW (2000) Fluorescence microscopy with diffraction resolution barrier broken by stimulated emission. *Proc Natl Acad Sci U S A* 97(15):8206-8210.
40. Rust MJ, Bates M, & Zhuang X (2006) Sub-diffraction-limit imaging by stochastic optical reconstruction microscopy (STORM). *Nat Methods* 3(10):793-795.
41. Betzig E, *et al.* (2006) Imaging intracellular fluorescent proteins at nanometer resolution. *Science* 313(5793):1642-1645.
42. Jing C & Cornish VW (2011) Chemical tags for labeling proteins inside living cells. *Acc Chem Res* 44(9):784-792.
43. Lelek M, *et al.* (2012) Superresolution imaging of HIV in infected cells with FlAsH-PALM. *Proc Natl Acad Sci U S A* 109(22):8564-8569.
44. Cherkezyan L, *et al.* (2014) Nanoscale changes in chromatin organization represent the initial steps of tumorigenesis: a transmission electron microscopy study. *BMC Cancer* 14:189.
45. Cherkezyan L, *et al.* (2013) Interferometric spectroscopy of scattered light can quantify the statistics of subdiffractional refractive-index fluctuations. *Phys Rev Lett* 111(3):033903.
46. Cherkezyan L, Subramanian H, & Backman V (2014) What structural length scales can be detected by the spectral variance of a microscope image? *Opt Lett* 39(15):4290-4293.
47. Kim JS, Pradhan P, Backman V, & Szleifer I (2011) The influence of chromosome density variations on the increase in nuclear disorder strength in carcinogenesis. *Phys Biol* 8(1):015004.
48. Stypula-Cyrus Y, *et al.* (2013) HDAC up-regulation in early colon field carcinogenesis is involved in cell tumorigenicity through regulation of chromatin structure. *PLoS One* 8(5):e64600.
49. Chandler JE, Cherkezyan L, Subramanian H, & Backman V (2016) Nanoscale refractive index fluctuations detected via sparse spectral microscopy. *Biomed Opt Express* 7(3):883-893.

50. Burma S, Chen BP, Murphy M, Kurimasa A, & Chen DJ (2001) ATM phosphorylates histone H2AX in response to DNA double-strand breaks. *The Journal of biological chemistry* 276(45):42462-42467.

51. Olive PL (2004) Detection of DNA damage in individual cells by analysis of histone H2AX phosphorylation. *Methods Cell Biol* 75:355-373.

52. Rogakou EP, Pilch DR, Orr AH, Ivanova VS, & Bonner WM (1998) DNA double-stranded breaks induce histone H2AX phosphorylation on serine 139. *The Journal of biological chemistry* 273(10):5858-5868.

53. Banath JP & Olive PL (2003) Expression of phosphorylated histone H2AX as a surrogate of cell killing by drugs that create DNA double-strand breaks. *Cancer Res* 63(15):4347-4350.

54. Cohen SM & Lippard SJ (2001) Cisplatin: from DNA damage to cancer chemotherapy. *Prog Nucleic Acid Res Mol Biol* 67:93-130.

55. Burgess RC, Burman B, Kruhlak MJ, & Misteli T (2014) Activation of DNA damage response signaling by condensed chromatin. *Cell Rep* 9(5):1703-1717.

56. Johnson SA, You Z, & Hunter T (2007) Monitoring ATM kinase activity in living cells. *DNA Repair (Amst)* 6(9):1277-1284.

57. Beerman TA*, et al.* (1992) Effects of analogs of the DNA minor groove binder Hoechst 33258 on topoisomerase II and I mediated activities. *Biochim Biophys Acta* 1131(1):53-61.

58. Zhang X, Chen J, Davis B, & Kiechle F (1999) Hoechst 33342 induces apoptosis in HL-60 cells and inhibits topoisomerase I in vivo. *Arch Pathol Lab Med* 123(10):921-927.

59. Kruhlak MJ*, et al.* (2006) Changes in chromatin structure and mobility in living cells at sites of DNA double-strand breaks. *J Cell Biol* 172(6):823-834.

60. Daugas E*, et al.* (2000) Mitochondrio-nuclear translocation of AIF in apoptosis and necrosis. *FASEB J* 14(5):729-739.

61. Lakhani SA*, et al.* (2006) Caspases 3 and 7: key mediators of mitochondrial events of apoptosis. *Science* 311(5762):847-851.

62. Lum JJ*, et al.* (2007) The transcription factor HIF-1alpha plays a critical role in the growth factor-dependent regulation of both aerobic and anaerobic glycolysis. *Genes Dev* 21(9):1037-1049.

63. Martinez-Pastor B, Cosentino C, & Mostoslavsky R (2013) A tale of metabolites: the cross-talk between chromatin and energy metabolism. *Cancer Discov* 3(5):497-501.

64. Liu XS, Little JB, & Yuan ZM (2015) Glycolytic metabolism influences global chromatin structure. *Oncotarget* 6(6):4214-4225.

65. Visvanathan A*, et al.* (2013) Modulation of Higher Order Chromatin Conformation in Mammalian Cell Nuclei Can Be Mediated by Polyamines and Divalent Cations. *PLoS One* 8(6):e67689.

66. Tice RR, Hook GG, Donner M, McRee DI, & Guy AW (2002) Genotoxicity of radiofrequency signals. I. Investigation of DNA damage and micronuclei induction in cultured human blood cells. *Bioelectromagnetics* 23(2):113-126.

67. Bancaud A*, et al.* (2009) Molecular crowding affects diffusion and binding of nuclear proteins in heterochromatin and reveals the fractal organization of chromatin. *EMBO J* 28(24):3785-3798.

68. Papantonis A & Cook PR (2010) Genome architecture and the role of transcription. *Curr Opin Cell Biol* 22(3):271-276.

69. Williamson I*, et al.* (2014) Spatial genome organization: contrasting views from chromosome conformation capture and fluorescence in situ hybridization. *Genes Dev* 28(24):2778-2791.

70. Katada S, Imhof A, & Sassone-Corsi P (2012) Connecting threads: epigenetics and metabolism. *Cell* 148(1-2):24-28.

71. Azuara V*, et al.* (2006) Chromatin signatures of pluripotent cell lines. *Nat Cell Biol* 8(5):532-538.

72. Hajkova P*, et al.* (2008) Chromatin dynamics during epigenetic reprogramming in the mouse germ line. *Nature* 452(7189):877-881.

73. Rao SS*, et al.* (2014) A 3D map of the human genome at kilobase resolution reveals principles of chromatin looping. *Cell* 159(7):1665-1680.

74. Bohn M & Heermann DW (2010) Diffusion-driven looping provides a consistent framework for chromatin organization. *PLoS One* 5(8):e12218.

75. Dong B*, et al.* (2016) Superresolution intrinsic fluorescence imaging of chromatin utilizing native, unmodified nucleic acids for contrast. *Proc Natl Acad Sci U S A* 113(35):9716-9721.

76. Matsuda H, Putzel GG, Backman V, & Szleifer I (2014) Macromolecular crowding as a regulator of gene transcription. *Biophys J* 106(8):1801-1810.

77. Rao SSP*, et al.* (2017) Cohesin Loss Eliminates All Loop Domains. *Cell* 171(2):305-320 e324.

78. Du P, Kibbe WA, & Lin SM (2008) lumi: a pipeline for processing Illumina microarray. *Bioinformatics* 24(13):1547-1548.

79. Jin F*, et al.* (2013) A high-resolution map of the three-dimensional chromatin interactome in human cells. *Nature* 503(7475):290-294.

80. Chagin VO*, et al.* (2016) 4D Visualization of replication foci in mammalian cells corresponding to individual replicons. *Nat Commun* 7:11231.

81. Frolov RV & Singh S (2014) Celecoxib and ion channels: a story of unexpected discoveries. *Eur J Pharmacol* 730:61-71.

82. Pardo LA, Contreras-Jurado C, Zientkowska M, Alves F, & Stuhmer W (2005) Role of voltage-gated potassium channels in cancer. *J Membr Biol* 205(3):115-124.

83. Felipe A*, et al.* (2006) Potassium channels: new targets in cancer therapy. *Cancer Detect Prev* 30(4):375-385.

84. Brunet A*, et al.* (2004) Stress-dependent regulation of FOXO transcription factors by the SIRT1 deacetylase. *Science* 303(5666):2011-2015.

85. Kao CL*, et al.* (2010) Resveratrol protects human endothelium from H(2)O(2)-induced oxidative stress and senescence via SirT1 activation. *J Atheroscler Thromb* 17(9):970-979.

86. Alcendor RR*, et al.* (2007) Sirt1 regulates aging and resistance to oxidative stress in the heart. *Circ Res* 100(10):1512-1521.

87. Schug TT*, et al.* (2010) Myeloid deletion of SIRT1 induces inflammatory signaling in response to environmental stress. *Mol Cell Biol* 30(19):4712-4721.

88. Yeung F*, et al.* (2004) Modulation of NF-kappaB-dependent transcription and cell survival by the SIRT1 deacetylase. *EMBO J* 23(12):2369-2380.

89. Yang Z, Kahn BB, Shi H, & Xue BZ (2010) Macrophage alpha1 AMP-activated protein kinase (alpha1AMPK) antagonizes fatty acid-induced inflammation through SIRT1. *The Journal of biological chemistry* 285(25):19051-19059.

90. Breitenstein A*, et al.* (2011) Sirt1 inhibition promotes in vivo arterial thrombosis and tissue factor expression in stimulated cells. *Cardiovasc Res* 89(2):464-472.

91. Gorenne I*, et al.* (2013) Vascular smooth muscle cell sirtuin 1 protects against DNA damage and inhibits atherosclerosis. *Circulation* 127(3):386-396.

92. Jiang B, Jen M, Perrin L, Wertheim JA, & Ameer GA (2015) SIRT1 Overexpression Maintains Cell Phenotype and Function of Endothelial Cells Derived from Induced Pluripotent Stem Cells. *Stem Cells Dev* 24(23):2740-2745.

93. Li L*, et al.* (2011) SIRT1 Acts as a Modulator of Neointima Formation Following Vascular Injury in Mice. *Circulation Research* 108(10):1180-U1195.

94. Zhang QJ*, et al.* (2008) Endothelium-specific overexpression of class III deacetylase SIRT1 decreases atherosclerosis in apolipoprotein E-deficient mice. *Cardiovasc Res* 80(2):191-199.

95. Kuo HY, DeLuca TA, Miller WM, & Mrksich M (2013) Profiling deacetylase activities in cell lysates with peptide arrays and SAMDI mass spectrometry. *Anal Chem* 85(22):10635-10642.

96. Gurard-Levin ZA, Kilian KA, Kim J, Bahr K, & Mrksich M (2010) Peptide arrays identify isoform-selective substrates for profiling endogenous lysine deacetylase activity. *ACS Chem Biol* 5(9):863-873.

97. Langley E*, et al.* (2002) Human SIR2 deacetylates p53 and antagonizes PML/p53-induced cellular senescence. *EMBO J* 21(10):2383-2396.

98. Warboys CM*, et al.* (2014) Disturbed flow promotes endothelial senescence via a p53-dependent pathway. *Arterioscler Thromb Vasc Biol* 34(5):985-995.

99. Takemura A*, et al.* (2011) Sirtuin 1 retards hyperphosphatemia-induced calcification of vascular smooth muscle cells. *Arterioscler Thromb Vasc Biol* 31(9):2054-2062.

100. Dimri GP*, et al.* (1995) A Biomarker That Identifies Senescent Human-Cells in Culture and in Aging Skin in-Vivo. *P Natl Acad Sci USA* 92(20):9363-9367.

101. Fenton M, Barker S, Kurz DJ, & Erusalimsky JD (2001) Cellular senescence after single and repeated balloon catheter denudations of rabbit carotid arteries. *Arterioscler Thromb Vasc Biol* 21(2):220-226.

102. Vasile E, Tomita Y, Brown LF, Kocher O, & Dvorak HF (2001) Differential expression of thymosin beta-10 by early passage and senescent vascular endothelium is modulated by VPF/VEGF: evidence for senescent endothelial cells in vivo at sites of atherosclerosis. *FASEB J* 15(2):458-466.

103. Feldman JL, Dittenhafer-Reed KE, & Denu JM (2012) Sirtuin catalysis and regulation. *The Journal of biological chemistry* 287(51):42419-42427.

104. Kim J*, et al.* (2013) Designing nanotopographical density of extracellular matrix for controlled morphology and function of human mesenchymal stem cells. *Sci Rep* 3:3552.

105. Versaevel M, Grevesse T, & Gabriele S (2012) Spatial coordination between cell and nuclear shape within micropatterned endothelial cells. *Nat Commun* 3:671.

106. Downing TL*, et al.* (2013) Biophysical regulation of epigenetic state and cell reprogramming. *Nat Mater* 12(12):1154-1162.

107. Davidson PM*, et al.* (2010) Topographically induced self-deformation of the nuclei of cells: dependence on cell type and proposed mechanisms. *J Mater Sci Mater Med* 21(3):939-946.

108. Hanson L*, et al.* (2015) Vertical nanopillars for in situ probing of nuclear mechanics in adherent cells. *Nat Nanotechnol* 10(6):554-562.

109. Liu X*, et al.* (2016) Subcellular cell geometry on micropillars regulates stem cell differentiation. *Biomaterials* 111:27-39.

110. Talwar S, Jain N, & Shivashankar GV (2014) The regulation of gene expression during onset of differentiation by nuclear mechanical heterogeneity. *Biomaterials* 35(8):2411-2419.

111. Riegler J*, et al.* (2015) Human Engineered Heart Muscles Engraft and Survive Long Term in a Rodent Myocardial Infarction Model. *Circ Res* 117(8):720-730.

112. Kraitchman DL*, et al.* (2003) In vivo magnetic resonance imaging of mesenchymal stem cells in myocardial infarction. *Circulation* 107(18):2290-2293.

113. Bauer GM*, et al.* (2017) The transformation of the nuclear nanoarchitecture in human field carcinogenesis. *Future Sci OA* 3(3):FSO206.

114. Braakhuis BJ, Tabor MP, Kummer JA, Leemans CR, & Brakenhoff RH (2003) A genetic explanation of Slaughter's concept of field cancerization: evidence and clinical implications. *Cancer Res* 63(8):1727-1730.

115. Dakubo GD, Jakupciak JP, Birch-Machin MA, & Parr RL (2007) Clinical implications and utility of field cancerization. *Cancer Cell Int* 7:2.

116. Backman V & Roy HK (2011) Light-scattering technologies for field carcinogenesis detection: a modality for endoscopic prescreening. *Gastroenterology* 140(1):35-41.

117. Paun BC*, et al.* (2010) Relation between normal rectal methylation, smoking status, and the presence or absence of colorectal adenomas. *Cancer* 116(19):4495-4501.

118. Polley AC*, et al.* (2006) Proteomic analysis reveals field-wide changes in protein expression in the morphologically normal mucosa of patients with colorectal neoplasia. *Cancer Res* 66(13):6553-6562.

119. Radosevich AJ, Yi J, Rogers JD, & Backman V (2012) Structural length-scale sensitivies of reflectance measurements in continuous random media under the Born approximation. *Opt Lett* 37(24):5220-5222.

120. Subramanian H*, et al.* (2009) Partial-wave microscopic spectroscopy detects subwavelength refractive index fluctuations: an application to cancer diagnosis. *Opt Lett* 34(4):518-520.

121. Subramanian H*, et al.* (2008) Optical methodology for detecting histologically unapparent nanoscale consequences of genetic alterations in biological cells. *Proc Natl Acad Sci U S A* 105(51):20118-20123.

122. Damania D*, et al.* (2013) Insights into the field carcinogenesis of ovarian cancer based on the nanocytology of endocervical and endometrial epithelial cells. *Int J Cancer* 133(5):1143-1152.

123. Damania D*, et al.* (2012) Nanocytology of rectal colonocytes to assess risk of colon cancer based on field cancerization. *Cancer Res* 72(11):2720-2727.

124. Konda VJ*, et al.* (2013) Nanoscale markers of esophageal field carcinogenesis: potential implications for esophageal cancer screening. *Endoscopy* 45(12):983-988.

125. Roy HK*, et al.* (2015) Nanocytological field carcinogenesis detection to mitigate overdiagnosis of prostate cancer: a proof of concept study. *PLoS One* 10(2):e0115999.

126. Roy HK*, et al.* (2013) Nano-architectural alterations in mucus layer fecal colonocytes in field carcinogenesis: potential for screening. *Cancer Prev Res (Phila)* 6(10):1111-1119.
127. Roy HK*, et al.* (2010) Optical detection of buccal epithelial nanoarchitectural alterations in patients harboring lung cancer: implications for screening. *Cancer Res* 70(20):7748-7754.
128. Li G & Reinberg D (2011) Chromatin higher-order structures and gene regulation. *Curr Opin Genet Dev* 21(2):175-186.
129. Hayashi MT & Masukata H (2011) Regulation of DNA replication by chromatin structures: accessibility and recruitment. *Chromosoma* 120(1):39-46.
130. Bista RK*, et al.* (2012) Nuclear nano-morphology markers of histologically normal cells detect the "field effect" of breast cancer. *Breast Cancer Res Treat* 135(1):115-124.
131. Hartman DJ*, et al.* (2014) Assessment of nuclear nanomorphology marker to improve the detection of malignancy from bile duct biopsy specimens. *Am J Clin Pathol* 141(6):884-891.
132. Robles FE, Zhu Y, Lee J, Sharma S, & Wax A (2010) Detection of early colorectal cancer development in the azoxymethane rat carcinogenesis model with Fourier domain low coherence interferometry. *Biomed Opt Express* 1(2):736-745.
133. Sridharan S, Macias V, Tangella K, Kajdacsy-Balla A, & Popescu G (2015) Prediction of prostate cancer recurrence using quantitative phase imaging. *Sci Rep* 5:9976.
134. Uttam S*, et al.* (2015) Early Prediction of Cancer Progression by Depth-Resolved Nanoscale Mapping of Nuclear Architecture from Unstained Tissue Specimens. *Cancer Res* 75(22):4718-4727.
135. Kagami Y & Yoshida K (2016) The functional role for condensin in the regulation of chromosomal organization during the cell cycle. *Cell Mol Life Sci*.
136. Subramanian H*, et al.* (2016) Procedures for risk-stratification of lung cancer using buccal nanocytology. *Biomed Opt Express* 7(9):3795-3810.
137. Miao Q, Derbas J, Eid A, Subramanian H, & Backman V (2016) Automated Cell Selection Using Support Vector Machine for Application to Spectral Nanocytology. *Biomed Res Int* 2016:6090912.
138. Subramanian H*, et al.* (2009) Nanoscale cellular changes in field carcinogenesis detected by partial wave spectroscopy. *Cancer Res* 69(13):5357-5363.
139. Damania D*, et al.* (2010) Role of cytoskeleton in controlling the disorder strength of cellular nanoscale architecture. *Biophys J* 99(3):989-996.
140. Michor F, Liphardt J, Ferrari M, & Widom J (2011) What does physics have to do with cancer? *Nat Rev Cancer* 11(9):657-670.
141. Wu W*, et al.* (2016) Using electron microscopy to calculate optical properties of biological samples. *Biomed Opt Express* 7(11):4749-4762.
142. Gibcus JH & Dekker J (2013) The hierarchy of the 3D genome. *Mol Cell* 49(5):773-782.
143. Minucci S & Pelicci PG (2006) Histone deacetylase inhibitors and the promise of epigenetic (and more) treatments for cancer. *Nat Rev Cancer* 6(1):38-51.
144. Welch DR (2016) Tumor Heterogeneity--A 'Contemporary Concept' Founded on Historical Insights and Predictions. *Cancer Res* 76(1):4-6.
145. Magee JA, Piskounova E, & Morrison SJ (2012) Cancer stem cells: impact, heterogeneity, and uncertainty. *Cancer Cell* 21(3):283-296.
146. Gerlinger M*, et al.* (2012) Intratumor heterogeneity and branched evolution revealed by multiregion sequencing. *N Engl J Med* 366(10):883-892.
147. Swanton C (2012) Intratumor heterogeneity: evolution through space and time. *Cancer Res* 72(19):4875-4882.
148. Burrell RA, McGranahan N, Bartek J, & Swanton C (2013) The causes and consequences of genetic heterogeneity in cancer evolution. *Nature* 501(7467):338-345.
149. Ling S*, et al.* (2015) Extremely high genetic diversity in a single tumor points to prevalence of non-Darwinian cell evolution. *Proc Natl Acad Sci U S A* 112(47):E6496-6505.
150. Easwaran H, Tsai HC, & Baylin SB (2014) Cancer epigenetics: tumor heterogeneity, plasticity of stem-like states, and drug resistance. *Mol Cell* 54(5):716-727.
151. Tomasetti C & Vogelstein B (2015) Cancer etiology. Variation in cancer risk among tissues can be explained by the number of stem cell divisions. *Science* 347(6217):78-81.
152. Sun J*, et al.* (2014) Clonal dynamics of native haematopoiesis. *Nature* 514(7522):322-327.

153. Levy SF, Ziv N, & Siegal ML (2012) Bet hedging in yeast by heterogeneous, age-correlated expression of a stress protectant. *PLoS Biol* 10(5):e1001325.
154. Breker M, Gymrek M, & Schuldiner M (2013) A novel single-cell screening platform reveals proteome plasticity during yeast stress responses. *J Cell Biol* 200(6):839-850.
155. Yadav N & Chandra D (2014) Mitochondrial and postmitochondrial survival signaling in cancer. *Mitochondrion* 16:18-25.
156. Lane RK, Hilsabeck T, & Rea SL (2015) The role of mitochondrial dysfunction in age-related diseases. *Biochim Biophys Acta* 1847(11):1387-1400.
157. Hay N (2011) Interplay between FOXO, TOR, and Akt. *Bba-Mol Cell Res* 1813(11):1965-1970.
158. Hanahan D & Weinberg RA (2011) Hallmarks of cancer: the next generation. *Cell* 144(5):646-674.
159. Morgan MA & Shilatifard A (2015) Chromatin signatures of cancer. *Genes Dev* 29(3):238-249.
160. Cancer Genome Atlas N (2012) Comprehensive molecular characterization of human colon and rectal cancer. *Nature* 487(7407):330-337.
161. Feinberg AP, Ohlsson R, & Henikoff S (2006) The epigenetic progenitor origin of human cancer. *Nat Rev Genet* 7(1):21-33.
162. Goutzanis L*, et al.* (2008) Nuclear fractal dimension as a prognostic factor in oral squamous cell carcinoma. *Oral Oncol* 44(4):345-353.
163. Holohan C, Van Schaeybroeck S, Longley DB, & Johnston PG (2013) Cancer drug resistance: an evolving paradigm. *Nat Rev Cancer* 13(10):714-726.
164. Brown K & Rufini A (2015) New concepts and challenges in the clinical translation of cancer preventive therapies: the role of pharmacodynamic biomarkers. *Ecancermedicalscience* 9:601.
165. Tan C, Saurabh S, Bruchez MP, Schwartz R, & Leduc P (2013) Molecular crowding shapes gene expression in synthetic cellular nanosystems. *Nat Nanotechnol* 8(8):602-608.
166. Morelli MJ, Allen RJ, & Wolde PR (2011) Effects of macromolecular crowding on genetic networks. *Biophys J* 101(12):2882-2891.
167. Collins FS (1999) Shattuck lecture - Medical and societal consequences of the human genome project. *New Engl J Med* 341(1):28-37.
168. Bailey JN, Pericak-Vance MA, & Haines JL (2014) The impact of the human genome project on complex disease. *Genes (Basel)* 5(3):518-535.
169. Forbes SA*, et al.* (2015) COSMIC: exploring the world's knowledge of somatic mutations in human cancer. *Nucleic Acids Res* 43(Database issue):D805-811.
170. Iwafuchi-Doi M & Zaret KS (2014) Pioneer transcription factors in cell reprogramming. *Genes Dev* 28(24):2679-2692.
171. Zhang Z & Pugh BF (2011) High-resolution genome-wide mapping of the primary structure of chromatin. *Cell* 144(2):175-186.
172. Lupianez DG*, et al.* (2015) Disruptions of topological chromatin domains cause pathogenic rewiring of gene-enhancer interactions. *Cell* 161(5):1012-1025.
173. Franke M*, et al.* (2016) Formation of new chromatin domains determines pathogenicity of genomic duplications. *Nature* 538(7624):265-269.
174. Lynch HT, Rendell M, Shaw TG, Silberstein P, & Ngo BT (2016) Commentary on Almassalha et al., "The Greater Genomic Landscape: The Heterogeneous Evolution of Cancer". *Cancer Res* 76(19):5602-5604.
175. Lee MC*, et al.* (2014) Single-cell analyses of transcriptional heterogeneity during drug tolerance transition in cancer cells by RNA sequencing. *Proc Natl Acad Sci U S A* 111(44):E4726-4735.
176. Li H*, et al.* (2012) Versatile pathway-centric approach based on high-throughput sequencing to anticancer drug discovery. *Proc Natl Acad Sci U S A* 109(12):4609-4614.
177. Pertea M, Kim D, Pertea GM, Leek JT, & Salzberg SL (2016) Transcript-level expression analysis of RNA-seq experiments with HISAT, StringTie and Ballgown. *Nat Protoc* 11(9):1650-1667.
178. Hansen MM*, et al.* (2016) Macromolecular crowding creates heterogeneous environments of gene expression in picolitre droplets. *Nat Nanotechnol* 11(2):191-197.
179. Roy HK, Hensing T, & Backman V (2011) Nanocytology for field carcinogenesis detection: novel paradigm for lung cancer risk stratification. *Future Oncol* 7(1):1-3.
180. Wali RK*, et al.* (2016) Higher-Order Chromatin Modulator Cohesin SA1 is an Early Biomarker for Colon Carcinogenesis: Race-Specific Implications. *Cancer Prev Res (Phila)*.

181. Seagle BL*, et al.* (2015) TP53 hot spot mutations in ovarian cancer: selective resistance to microtubule stabilizers in vitro and differential survival outcomes from The Cancer Genome Atlas. *Gynecol Oncol* 138(1):159-164.
182. Ahn JH, Kim TJ, Lee JH, & Choi JH (2017) Mutant p53 stimulates cell invasion through an interaction with Rad21 in human ovarian cancer cells. *Sci Rep* 7(1):9076.
183. Paek AL, Liu JC, Loewer A, Forrester WC, & Lahav G (2016) Cell-to-Cell Variation in p53 Dynamics Leads to Fractional Killing. *Cell* 165(3):631-642.
184. Shaffer SM*, et al.* (2017) Rare cell variability and drug-induced reprogramming as a mode of cancer drug resistance. *Nature* 546(7658):431-435.
185. Kang HR, Choi HG, Jeon CK, Lim SJ, & Kim SH (2016) Butyrate-mediated acquisition of chemoresistance by human colon cancer cells. *Oncol Rep* 36(2):1119-1126.
186. Pall ML (2013) Electromagnetic fields act via activation of voltage-gated calcium channels to produce beneficial or adverse effects. *J Cell Mol Med* 17(8):958-965.
187. Carson JJ, Prato FS, Drost DJ, Diesbourg LD, & Dixon SJ (1990) Time-varying magnetic fields increase cytosolic free Ca2+ in HL-60 cells. *Am J Physiol* 259(4 Pt 1):C687-692.
188. Tamrin SH, Majedi FS, Tondar M, Sanati-Nezhad A, & Hasani-Sadrabadi MM (2016) Electromagnetic Fields and Stem Cell Fate: When Physics Meets Biology. *Rev Physiol Biochem Pharmacol* 171:63-97.
189. Meyerhardt JA*, et al.* (2006) Impact of physical activity on cancer recurrence and survival in patients with stage III colon cancer: findings from CALGB 89803. *J Clin Oncol* 24(22):3535-3541.
190. Park J*, et al.* (2017) The Effects of Physical Activity and Body Fat Mass on Colorectal Polyp Recurrence in Patients with Previous Colorectal Cancer. *Cancer Prev Res (Phila)* 10(8):478-484.
191. Ruiz-Casado A*, et al.* (2017) Exercise and the Hallmarks of Cancer. *Trends Cancer* 3(6):423-441.
192. Wu W*, et al.* (2016) Pre- and post-diagnosis physical activity is associated with survival benefits of colorectal cancer patients: a systematic review and meta-analysis. *Oncotarget* 7(32):52095-52103.

Appendices

APPENDIX A. Label-free imaging of the native, living cellular nanoarchitecture using partial wave spectroscopic (PWS) microscopy

Figure A1. *UV excitation of Hoechst 33342 in Chinese hamster ovarian (CHO) cells.*

Figure A2. *Distribution statistics for Hoechst-stained cells.*
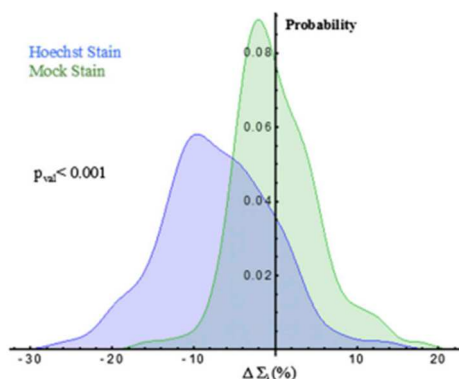
Figure A1. *UV excitation of Hoechst 33342 in Chinese hamster ovarian (CHO) cells.* Distribution of nuclear transformation (ΔPost-Pre irradiation) after UV excitation for mock-stained (green) and Hoechst-stained (blue) CHO cells. As with HeLa cells, CHO cell nuclei demonstrate a decrease in signal immediately after irradiation in the Hoechst-stained cells.
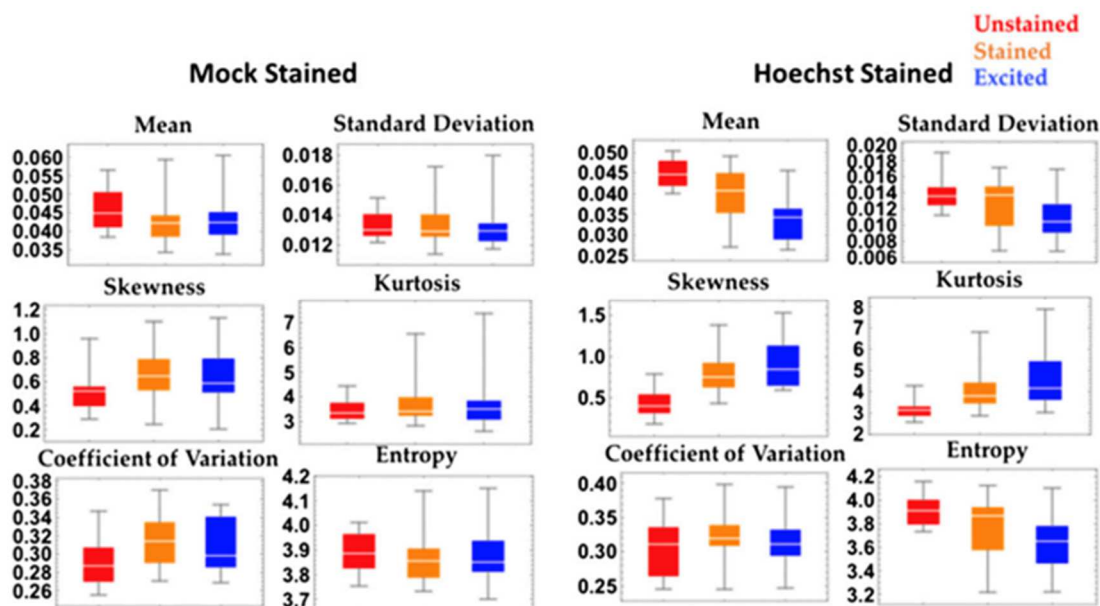

Figure A2. *Distribution statistics for Hoechst-stained cells.* The effect of Hoechst staining on the statistical properties of the nanoarchitecture as measured by P within cell nuclei between mock-stained and Hoechst-stained cells. In addition to altering the mean nuclear P, Hoechst staining and its excitation

causes changes in the distribution of possible nuclear states. In particular, Hoechst staining increases the skewness and the kurtosis while decreasing the image entropy.

APPENDIX B. The vasculoprotective effects of Sirt1

Figure B1. *Sirt1-overexpressing Aortic Adventital Fibroblast (AoAF).*

Figure B2. *Sirt1 overexpression in rat carotid arteries occurs primarily in the adventitia.*
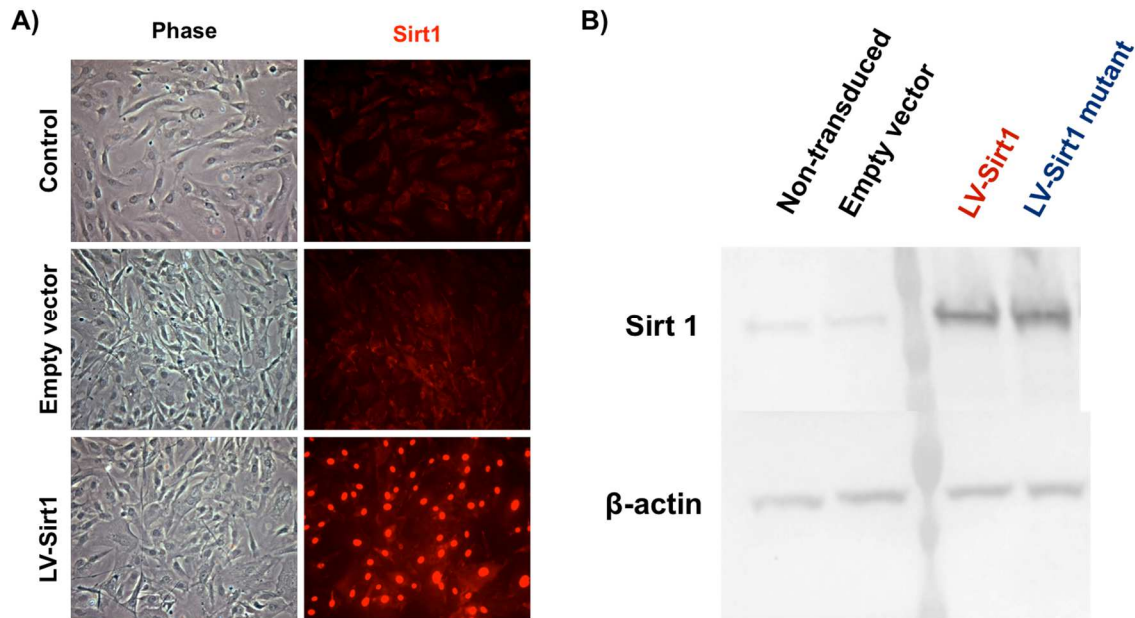
Figure B1. *Sirt1-overexpressing Aortic Adventital Fibroblast (AoAF).* Sirt1 or a Sirt1 dominant negative mutant (H363Y) was cloned into a lentiviral transfer plasmid and lentiviral vectors encoding for Sirt1 (LV-Sirt1) or Sirt1 mutant (LV- Sirt1 mutant) were produced. Primary human AoAFs were incubated either with LV- Sirt1, LV- Sirt1 mutant, or empty vector (lentiviral vector without the Sirt1 gene) and, after three days of transduction, immunostained or lysed and immunoblotted for Sirt1. The immunofluorescence stain (A) and immunoblot (B) demonstrate overexpression of Sirt1 for cells transduced with LV- Sirt1 or LV- Sirt1 dominant negative mutant.
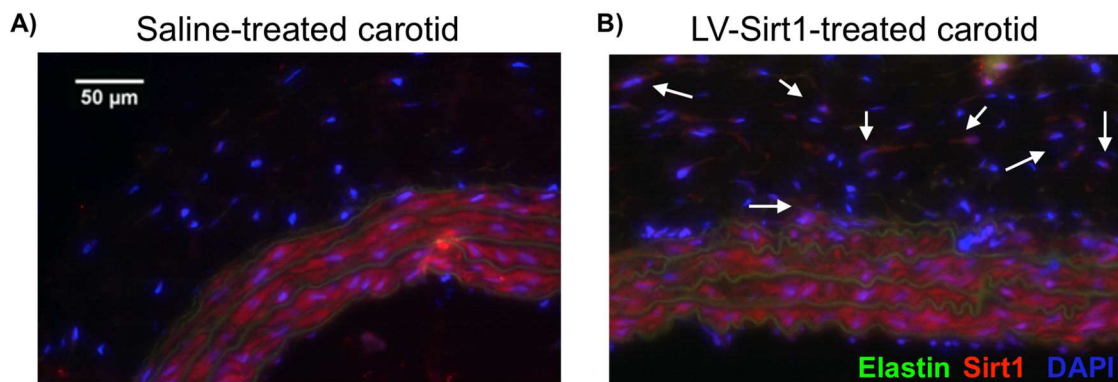
Figure B2. *Sirt1 overexpression in rat carotid arteries occurs primarily in the adventitia.* To address whether LV- Sirt1 can transduce adventitial cells *in vivo*, we perivascularly applied LV- Sirt1 around the left carotid arteries of rats. After 8 days of transduction, Sirt1-overexpessing cells were predominantly observed in the adventitia of carotid arteries treated with lentiviruses encoding for Sirt1 (LV- Sirt1). While

Sirt1 is ubiquitously expressed in all cell types, in aortic tissue samples, Sirt1 expression is the highest in the medial layer where the smooth muscle cells reside.

APPENDIX C. Chromatin scaling and macrogenomic engineering in cancer evolution

Figure C1. *Pharmacological agents can modulate chromatin packing density heterogeneity with cell line specificity.*
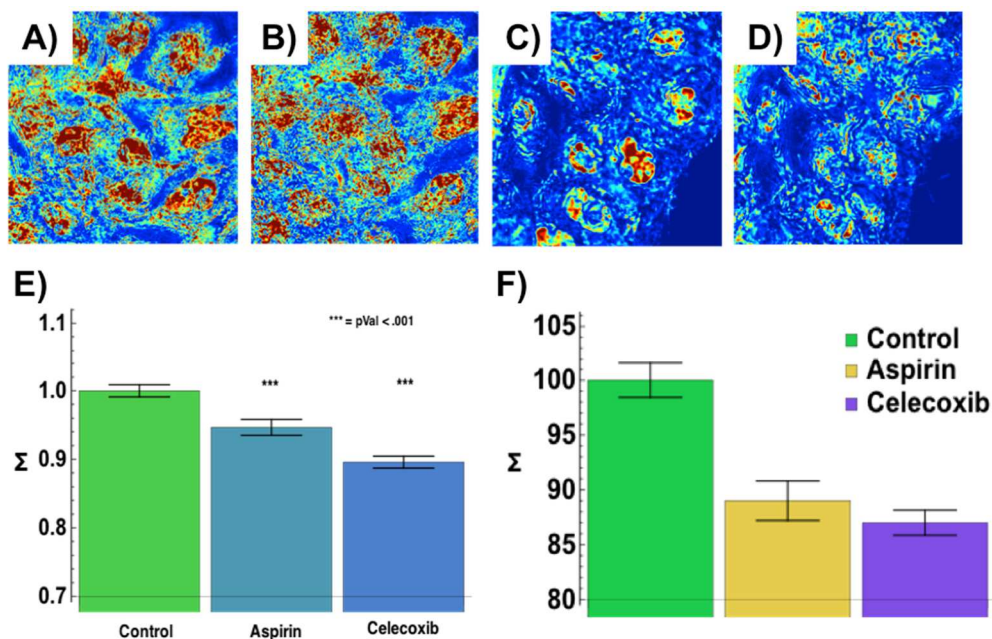
Figure C2: *HCT 116 colon cancer cells treated with chromatin scaling-modulatory agents.*

Figure C3. *Pharmacological agents can preferentially modulate chromatin packing density heterogeneity of cancer cells.*
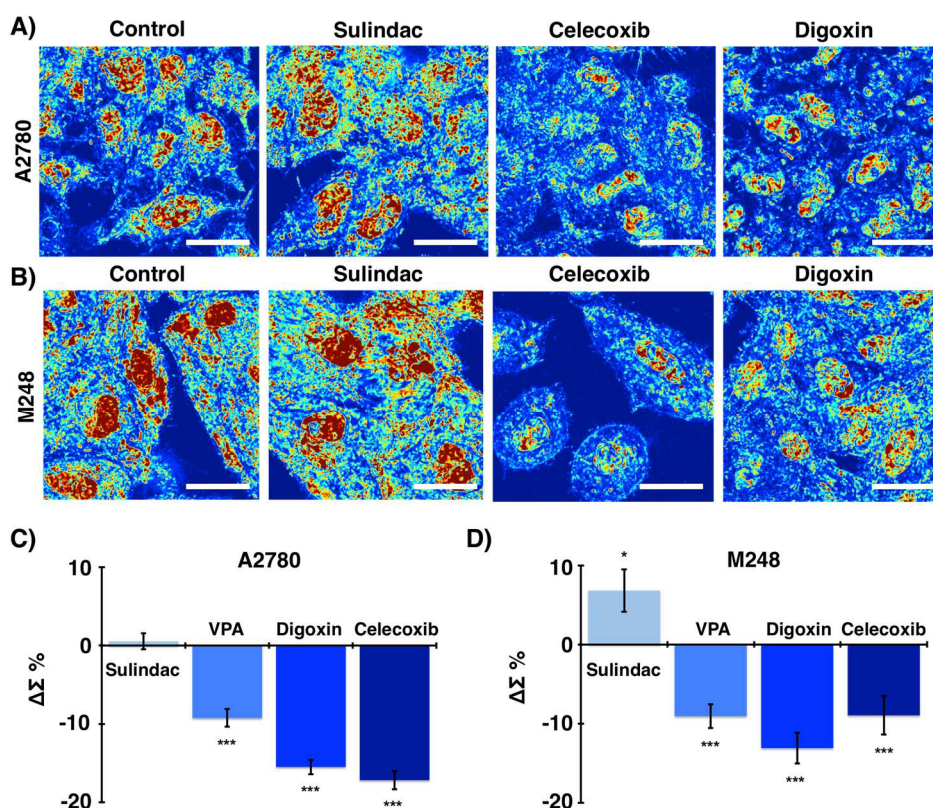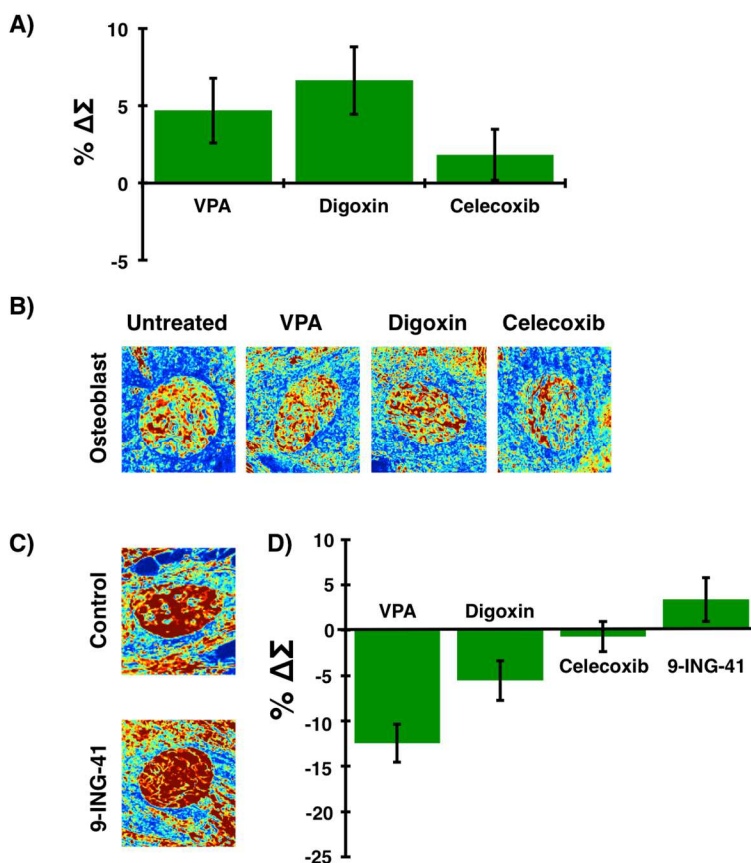

Figure C1. *Pharmacological agents can modulate chromatin packing density heterogeneity with cell line specificity.* A&B) Representative PWS microscopy images of the effects of potential CPT agents on chromatin packing density heterogeneity for WT A2780 (A) and derivative M248 (B) ovarian carcinoma cells treated with sulindac sulfide, valproic acid (VPA), celecoxib, and digoxin. C&D) Quantification of change to chromatin packing density heterogeneity in A2780 (C) and M248 (D) cells treated with potential chromatin scaling-modulatory agents. Chromatin packing density heterogeneity decreases within 30 minutes of treatment in cells treated with VPA (P=4.7x10^{-13} for A2780, 5.7x10^{-7} for M248), digoxin (P=3.1x10^{-36} for A2780, 6.2x10^{-9} for M248), and celecoxib (P=1.6x10^{-30} for A2780, 1.3x10^{-3} for M248). However, chromatin packing density heterogeneity remains unchanged in A2780 cells with sulindac treatment (P=0.96) and increases in M248 cells (P=1.6x10^{-2}) with sulindac treatment. Significance was determined using Student's t-test with unpaired, unequal variance on the average nuclear Σ normalized by the Σ of the accompanying control group between the conditions. Error bars are standard error for

N=161 sulindac, 117 VPA, 130 digoxin, and 132 celecoxib treated A2780 cells; *N*=57 sulindac, 51 VPA, 91 digoxin, and 72 celecoxib treated M248 cells (***P<0.001, *P<0.05). Scale bars, 20uM. Pseudo-color: heterogeneity of chromatin packing density (Σ).

Figure C2. *HCT 116 colon cancer cells treated with chromatin scaling-modulatory agents.* A&C) Representative images of chromatin topology of HCT-116 control cells, which do not express cyclooxygenase-2, prior to 30 minutes of treatment with (B) aspirin or (D) celecoxib. E) Chromatin packing density heterogeneity decreases within 30 minutes of treatment in cells treated with either aspirin or celecoxib (p-value <0.001). F) Chromatin packing density heterogeneity remains suppressed for prolonged periods in cells treated with celecoxib (24 hours) or aspirin (24 hours). P-value <0.001 for both groups.

Figure C3. *Pharmacological agents can preferentially modulate chromatin packing density heterogeneity of cancer cells.* A) Quantification of change to chromatin packing density heterogeneity in osteoblast cells differentiated from human mesenchymal stem cells (hMSCs) treated with VPA, digoxin, and celecoxib. While these compounds all decrease Σ in cancer cells, they do not significantly modulate Σ of osteoblasts at the time scale and concentration at which they do in cancer cells. B) Representative images of nanoscale chromatin packing density heterogeneity in osteoblasts differentiated from human mesenchymal stem cells (hMSCs) untreated and treated with VPA, digoxin, and celecoxib. C) Quantification of change in Σ in human mesenchymal stem cells (hMSCs) treated with top modulatory compounds from (A). VPA and digoxin both decrease Σ in hMSCs in addition to cancer cells, but celecoxib and 9-ING-41 do not change Σ of these stem cells at the time scale and concentration at which they do in cancer stem cells.